Universidad de Oviedo
Facultad de Química

Programa de Doctorado

Química Teórica y Modelización Computacional

Departamento de Química Física y Analítica

PRESIONES QUÍMICAS EN SÓLIDOS CRISTALINOS

HUSSIEN HELMY HASSAN OSMAN

Oviedo, España 2017

University of Oviedo
Faculty of Chemistry

Doctorate Programme

Theoretical Chemistry & Computational Modelling

Departament of Physical & Analytical Chemistry

CHEMICAL PRESSURES IN CRYSTALLINE SOLIDS

HUSSIEN HELMY HASSAN OSMAN

Oviedo, Spain 2017

University of Oviedo
Faculty of Chemistry

PhD Thesis

CHEMICAL PRESSURES IN CRYSTALLINE SOLIDS

HUSSIEN HELMY HASSAN OSMAN

PhD Supervisors

J. MANUEL RECIO MUÑIZ

MIGUEL Á. SALVADÓ SÁNCHEZ

Doctorate Programme

Theoretical Chemistry & Computational Modelling

Departament of Physical & Analytical Chemistry

Oviedo, Spain 2017

Universidad de Oviedo
Facultad de Química

Tesis Doctoral

PRESIONES QUÍMICAS EN SÓLIDOS CRISTALINOS

HUSSIEN HELMY HASSAN OSMAN

Dirigida por

J. MANUEL RECIO MUÑIZ

MIGUEL Á. SALVADÓ SÁNCHEZ

Programa de Doctorado

Química Teórica y Modelización Computacional

Departamento de Química Física y Analítica

Oviedo, España 2017

To my mum, my wife,
YASSIN & YOMNA

I believe the chemical bond is not so simple
as some people seem to think.
–Robert S. Mulliken

ACKNOWLEDGEMENTS

Foremost, I would like to express my sincere gratitude to my supervisor Prof. Jose Manuel Recio for the continuous support of my Ph.D study and research, for his patience, motivation, enthusiasm, and immense knowledge. His guidance helped me in all the time of research and writing of this thesis.

My appreciation also extends to my second supervisor Dr. Miguel Á. Salvadó, who expertly guided me through all the computational and theoretical issues of this thesis, for his unwavering support and recommendations. I would like also to thank Dr. Pilar Pertierra and Dr. Ruth Álvarez-Uría for their valuable assistance and helpful discussions over the improvement of the interpretation of the results of this thesis in several articles.

I thank my close friend Fernando Izquierdo Ruiz for his valuable work done at early stage of this thesis concerning vibrational frequencies and uranyl cluster calculations for the cesium uranyl tetrachloride under pressure study.

My sincere thanks also goes to Prof. Daniel C. Fredrickson and Dr. Joshua Engelkemier in University of Wisconsin, USA, for the helpful discussions and insightful comments regarding the DFT-CP analysis. It is my pleasure to have this collaboration that gave birth to an interesting article submitted to JACS.

I am also thankful to my mum and my wife for providing me the moral support and encouragement. Lastly, at this moment, I really thank my kids, Yassin & Yomna, for keeping silence without arguing to finish this document.

RESUMEN DEL CONTENIDO DE TESIS DOCTORAL

1.- Título de la Tesis	
Español/Otro Idioma: Presiones Químicas en Sólidos Cristalinos	Inglés: Chemical Pressures in Crystalline Solids

2.- Autor	
Nombre: HUSSIEN HELMY HASSAN OSMAN	DNI/Pasaporte/NIE:
Programa de Doctorado: Química Teórica y Modelización Computacional	
Órgano responsable: Centro Internacional de Postgrado	

RESUMEN (en español)

Esta tesis doctoral recoge el resultado de una investigación teórica y computacional dirigida a establecer una conexión entre la solución de la ecuación de Schrödinger electrónica en sistemas cristalinos y el enlace químico. Se ha utilizado el cristal de $Cs_2UO_2Cl_4$ con el doble objetivo de avanzar en el entendimiento de su comportamiento bajo presión hidrostática, resolviendo ciertas controversias en relación con la regla de Badger, y de conocer los detalles computacionales y metodológicos de los cálculos de primeros principios basados en la aproximación de la teoría del funcional de la densidad electrónica (DFT) en el estado sólido. El núcleo central de la tesis es el análisis y aplicación del formalismo de la presión química (CP) en moléculas (H_2, CO_2, S_8) y sólidos exhibiendo todo tipo dé interacciones químicas: covalentes (grafeno, diamante), iónicas (haluros e hidruros alcalinas), metálicas (elementos del grupo 15, metales alcalinos), de van der Waals (CO_2, S_8, grafito) y enlaces de hidrógeno (hielo-I). A partir de la distribución de la energía DFT en los puntos de una rejilla en la que se divide la celda unidad cristalina es posible construir mapas 1D, 2D y 3D de presiones químicas. Estos mapas sirven para identificar con claridad las regiones responsables de las atracciones y repulsiones que dan lugar a la cohesión en todos los sistemas cristalinos explorados. Enlaces, pares solitarios, dominios de interacciones dispersivas o de repulsiones estéricas pueden ser discutidos en términos de las contribuciones energéticas propias de la DFT. El formalismo DFT-CP ilustra además la validez del modelo interpretativo de las estructuras cristalinas de compuestos inorgánicos en el que se entiende que es la subred metálica (Na, Ca, BaSn) la que induce la posición final de los aniones en sus respectivos cristales (NaCl o NaF, CaO o CaF_2, $BaSnO_3$).

RESUMEN (en Inglés)

This doctoral thesis is the result of a theoretical and computational research aimed at establishing a connection between the solution of the Schrödinger electronic equation in crystalline systems and the chemical bonding concept. The crystal of $Cs_2UO_2Cl_4$ has been used with a two-fold objective: (i) to advance in the understanding of its behavior under hydrostatic pressure clarifying some controversies related to the Badger's rule, and (ii) to know the computational and methodological details of first principles calculations based on the density functional theory approximation (DFT) in the solid state. The core of the thesis is the analysis and application of the formalism of chemical pressure (CP) in molecules (H_2, CO_2, S_8) and solids exhibiting all kinds of chemical interactions: covalent (graphene, diamond), ionic (alkali halides and hydrides), metals (group 1 and group 15 elements), van der Waals (solid CO_2 and S_8, graphite) and hydrogen bonds (ice-I). From the distribution of the DFT energy at the points of a grid in which the crystal unit cell is divided, it is possible to construct 1D, 2D and 3D maps of chemical pressures. These maps serve to clearly identify the regions responsible for attractions and repulsions that give rise to cohesion in all explored crystalline systems. Bonds, lone pairs, domains of dispersive interactions or steric repulsions can be discussed in terms of DFT energy contributions. The DFT-CP formalism also illustrates the validity of the interpretive model of the crystal structure of inorganic compounds in which it is understood that the metallic sub-lattice (Na, Ca, BaSn, etc.) induces the final position of the anions in their respective crystals (NaCl or NaF, CaO or CaF_2, $BaSnO_3$, etc.).

SR. PRESIDENTE DE LA COMISIÓN ACADÉMICA DEL PROGRAMA DE DOCTORADO EN Química Teórica y Modelización Computacional

CONTENTS

Part I

Introduction

1 INTRODUCTION

This thesis is the result of four years of theoretical and computational work aimed at the development and application of chemical models that bridge the gap between the outcome of quantum mechanical electronic structure methodologies and the concept of chemical bonding in solids. The main contribution of the investigation is the formalization of a novel scheme that extends the Chemical Pressure (CP) formalism of Fredrickson *et al.* [33] towards the understanding and rationalization of the variety of chemical interactions exhibited by all classes of crystalline materials. The new perspective emerging from this thesis constitutes a unique alternative to current approaches based on the analysis of the electronic wavefunction. Within the chemical bonding-chemical pressure framework, covalent, metallic, ionic, hydrogen-bond and non-covalent interactions can be simultaneously dealt with and clearly identified following a simple computational strategy that allows quantitative analysis of any crystalline bonding network as well as its qualitative visual description through intuitive chemical pressure maps.

Chemical bonding has shown to be an elusive concept already since the advent of Quantum Mechanics in spite of being of paramount importance in all areas of Chemistry. This is mainly due to two practical reasons: it is not a perceptible property that can be experimentally observed and there is not any particular quantum-mechanical operator associated to it. From Lewis' picture in 1916 [74] to recent topological analysis of the electronic wavefunction, and through extensive developments within Pauling's view of *The Nature of Chemical Bond* [94, 95], our understanding of how and why chemical elements are linked in molecules and solids has progressively improved. The attempts to reconcile the intuitive chemical picture of Lewis electron pairs and the octet rule with the outcome of Schrödinger's electronic equation was very well illustrated by Silvi and Savin in their seminal analysis of the topology of the Electron Localization Function (ELF) [116]. More recently, in the context of a new bonding descriptor able to provide simultaneous visualization of covalent and non-covalent interactions, de Silva and Corminboeuf [19] critically reviewed the main developments concerning the quantum-mechanical analysis of chemical bonding. Methods related to the Natural Bond Orbital analysis of the one-particle density matrix [32, 105], and those based on the topology of most common scalar fields, as the electron density [2], the ELF [7], and the reduced density gradient [62] were briefly examined stating their drawbacks and main attributes. All these methods directly rely on one part of the solution of Schrödinger's equation, the wavefunction, whereas the other one, the energy, has not received explicit attention yet to the best of our knowledge. It will be of interest to find out in the following chapters how the energy eigenvalue of Schrödinger's electronic equation lead to a definition of chemical pressure that allows the characterization of the chemical bonding displaying similarities with previous scalar fields and in particular with the ELF.

A word of caution here is necessary to avoid confusion with the term chemical pressure. It is mostly used to describe how various atomic sizes affect physical properties. This concept has a long history in tackling structural distortions due to elemental substitutions in solids [13, 14, 20, 66, 81, 118]. It is noticed that the local pressures acting upon an atom are induced by the constraints of a crystal lattice where the bond distances are not the ideal ones. From the chemical point of view, the insertion of, for example, oxygen atoms in a metallic sub-lattice can be seen as a similar effect as the application of hydrostatic pressure due to the reduction of volume and/or the structural changes both produce in the solid [121]. This idea is supported by a topological analysis of the electron density dealing with the anions (O^{2-} ions) as a source of chemical pressure [123]. In principle, we can understand from these studies that there exist an equivalence between the local chemical pressure and the macroscopic thermodynamic pressure. However, as far as we know, a quantitative account of this relationship has not been reported so far.

In this thesis, we will deal with a novel and broader perspective of chemical pressure. With a rigorous growing expansion, the new formalism has recently emerged as a useful methodology [33] in Solid State Chemistry with a number of successful applications such as the anticipation of structures for intermetallic compounds [27], detection of soft modes driving second-order phase transitions [25], predicting structural instabilities [33, 34], and providing intuitive interpretations of the cohesion of crystalline solids [34]. The Chemical Pressure scheme is coupled to Density Functional-type calculations(DFT-CP) [8, 25, 34] to analyze the local pressures arising in crystal structures from the interactions of atomic size and electronic effects. Using simply the distribution of the minimized electronic energy along a grid of voxels in which the unit cell is partitioned, this methodology is able to provide the local pressure in each of these voxels just evaluating how their energy changes as the volume of the voxels departs from the equilibrium value. From these thermodynamic-like local pressures, chemical pressure maps can be built illustrating how high and low pressures are overall associated, respectively, with electron core and valence regions, thus providing a wealth of information on the existing and potential new interactions between the atomic constituents of the solid. This novel approach will be carefully examined in this document and constitutes a totally new alternative route far from previous and current extensions of chemical bonding methods based on the electronic wavefunction.

It is interesting to point out that well-established theoretical formalisms on the chemical bonding can be used to endorse our ideas. Support is also provided by other topological approaches, as the application of ELF in crystalline solids [16, 116], which shares a number of equivalent features regarding images of covalent, molecular, metallic or ionic bonding (examples will be presented in different chapters of this thesis). For our purposes, it is to be noticed that the basic quantum mechanical view of Ruedenberg and co-workers [28, 29, 106] provides an adequate scenario for interpreting in a straightforward way all the chemical pressure maps we will present in the following pages.

As a simple example, Fig. 1.1 displays the 2D chemical pressure map of a single CO_2 molecule and the corresponding 1D profile along the internuclear bonding path. Although the necessary details for a complete understanding of this figure will be given later, it is now relevant to see how the molecular space is partitioned

into chemically meaningful regions by the black isoline of zero chemical pressure. The positive chemical pressure located in the regions close to the nuclear positions (core), the *kinetic energy pressure* in Ruedenberg's words, is related to the so-called *promotion* state (a promolecule representation of the system built with atomic-like electronic densities consistent with the molecular solution), whereas the negative chemical pressure is related to the *interference* of atomic orbitals (valence region). The fact that this bonding decomposition can be associated with regions in the 3D space is one advantage of Ruedenberg's formalism concerning our chemical pressure application to chemical bonding. Ruedenberg likes to use the uncertainty principle in his reasoning. Thus, an increasing/decreasing of the electron localization leads to an increasing/decreasing of the kinetic energy helping to understand the mechanism of binding in the valence region. There, electrons are not so localized as in the cores, and the kinetic energy lowering in this internuclear region is the main contribution to the bonding according to Ruedenberg's formalism.

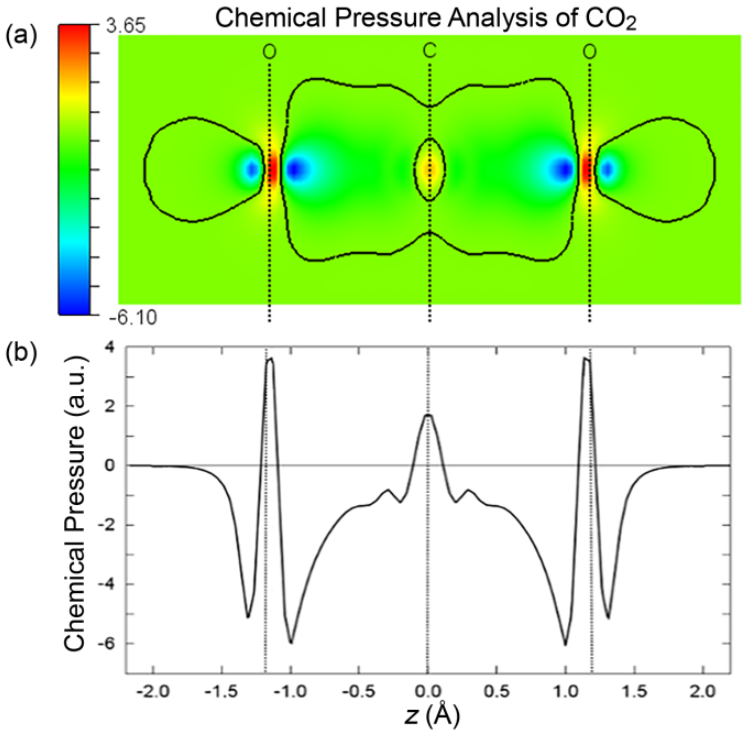

Figure 1.1: Chemical pressure (CP) analysis of a CO_2 molecule. (a) 2D cross-section of the CP map calculated for the molecule. A black contour is shown for CP=0. (b) 1D profile of CP map along the axis of the CO_2 molecule. Atomic units are used.

Interestingly enough, the core and valence regions in our 1D and 2D plots of the CO_2 molecule displayed in Fig. 1.1 are clearly differentiated, respectively, with positive and negative CP values. In addition to the core regions, positive pressures are also surrounding the CO_2 molecule in our map, whereas the negative pressure is split in zones associated with C-O bonds and O lone pairs. It should be noticed that at ambient conditions the average pressure in our maps has to be approximately zero (10^{-5} GPa) since we deal with systems in mechanical equilibrium.

Overall, in order to achieve the final thorough description of the chemical interactions within a given crystalline solid, the investigation has to be organized in two

steps. The first one concerns the solution of the Schrödinger's electronic equation of the crystal. The second one is the determination of the local chemical pressures in each of the voxels in which the crystalline unit cell is partitioned. The guiding thread of the thesis reflects these steps in the ongoing structure of this document.

Besides this introduction, Part II deals with the methodological aspects (chapter 2) and the computational details (chapter 3) of both electronic structure and chemical pressure calculations. In chapter 2, we will briefly present the basis of the density functional theory approximation starting with elementary concepts of quantum chemistry. There are a number of computational methodologies aimed at solving the Schrödinger electronic equation in crystalline solids. Most of these methods only require the positions of the atoms in the unit cell and their atomic numbers. They lead to the so-called first principles methodologies. The density functional theory (DFT) is one of the most effective formalism to perform such a total energy first principles calculations. This formalism is based on a set of equations, Kohn-Sham equations, that need to be solved in a self-consistent way. In this chapter, we will give an overview of DFT and how we can solve the Kohn-Sham equations and their extension in solids through the Bloch's theorem. The second part of chapter 2 describes the fundamentals of the DFT-Chemical Pressure analysis, including the theoretical ideas. The DFT-CP method was originally developed to deal with complex intermetallic structures whose formation appeared to be driven by conflicts between electronic and atomic size effects [8, 33]. As we have already mentioned, the DFT-CP approach has been recently used for predicting the vibrational properties of solids [25] and exploring the stability of complex intermetallics [27, 42], but never was considered for tackling chemical bonding ideas as in the present thesis.

Part II finishes with chapter 3, where we describe the different computational procedures of the theoretical calculations that can be grouped again in two main parts. First, the electronic structure calculations, including geometrical optimization, are considered with especial emphasis on convergence issues involving the energy cutoffs and k-point grids. The computational procedure of different calculations using several computational packages, such as `ABINIT` [39, 41] and `VASP` [12, 70, 71], will also be presented in this chapter. Second, the detailed strategy for constructing the raw data for the Chemical-Pressure program is also shown. The DFT-CP scheme contains two main computational programs necessary to carry out the CP analysis from the results of `ABINIT` calculations: CPmap and CPintegrate. The former creates the chemical pressure maps that are visualized with the program `VESTA 3` [82] while the latter integrate the pressures around each atom and project them onto spherical harmonics which are then visualized with the `MATLAB` code. In addition, the results of CPmap program can be presented in one-, two-, and three-dimensional profiles.

Besides, we have used other codes for various purposes. The `gibbs` code [10] was used in the computation of equation of state (EOS) fits to static first principles E(V) data and predict quantities such as the bulk modulus and its pressure derivatives. Bond critical points and electron density at critical points were obtained using the program `CRITIC2` [91]. The topological analysis of the electron density was carried out using the Bader partitioning method [2] under the Henkelman group code [119] to compute atomic volumes and charges. This chapter includes some hints about the previously mentioned codes.

Part III contains only chapter 4 devoted to the study of the effect of hydrostatic pressure, up to 50 GPa, on the structural and vibrational properties of cesium uranyl tetrachloride ($Cs_2UO_2Cl_4$). This system is complex enough to illustrate the details of how the optimized energy and wavefunction of a crystalline solid are computed and analyzed including also a critical comparison with available experimental data. In our study of $Cs_2UO_2Cl_4$, we seek to fulfill a two-fold objective. Firstly, we pretend to provide detailed information on the response of the monoclinic structure of cesium uranyl chloride complex to hydrostatic pressure conditions up to 50 GPa. We believe that these novel results can arouse enough interest since they contribute to broad the fundamental knowledge of UO_2-based compounds. Secondly, a microscopic interpretation of the evolution with pressure of the U–O stretching modes is carried out to unveil relationships between the corresponding frequencies and force constants, atomic charges and bond distances associated with the uranyl cation. Our analysis also predict that Badger's rule is invalid in its traditional form, thus supporting other previous conclusions in this direction [112, 113, 120].

In Part IV, the most important contribution of this thesis is developed in two chapters. Chapter 5 describes how the DFT Chemical Pressure (DFT-CP) method can form the basis of the visualization of the forces within chemical bonds. Actually, our main research interests are different from those leading to current studies within the CP formalism since we are focused on the nature of the chemical bond. We disclose how the CP approach turns to be an outstanding tool to identify and visualize the various types of chemical bonding networks not only for prototype covalent, molecular, metallic, and ionic solids, but also for more complex crystals displaying simultaneously localized or/and delocalized multiple covalent bonds along with van der Waals interactions, and hydrogen bonds. Rather than focusing on a quantitative description of the chemical bonding by means of indexes and descriptors of the chemical pressure scalar field and its topology, chapter 5 will almost exclusively address the visualization of bonding patterns in crystalline solids. The main and basic goal is to show that the chemical pressure formalism is an efficient tool to identify and characterize the chemical bonding in a wide variety of chemical systems, from covalent to ionic crystals, passing through metallic and molecular compounds with van der Waals and H-bond interactions. Our 1D, 2D, and 3D maps reveal the existence of the most common chemical entities involved in the cohesion of crystalline systems: core and valence regions, bonding and lone electron pairs, and ionic, atomic or molecular subsystems within a crystal, including the visualization of weak interactions domains too. Over a series of molecular and crystalline examples, specific features in the CP maps are identified as genuine for each of the different types of bonding interactions. We will begin our survey with a look at how covalent bonds are reflected in our chemical pressure maps of three different isolated molecules, H_2, CO_2 and S_8. To this basic study of systems with just one type of chemical bonding will be added two infinite systems, 2D graphene layer and C-diamond. Then, we will move to molecular crystals where van der Waals interactions occur alongside covalent bonds, as in graphite, in the low pressure phase of carbon dioxide, CO_2-I, and in solid sulfur. H-bonds will be examined in the ice-I_h phase of water. Metals will then be discussed later in the series of the 15-group elements As, Sb, and Bi, as well as *bcc*-Na, before we finish our journey along the different types of chemical bonding with the rock-salt structure of ionic NaCl.

In chapter 6, we discuss the origin of the CP features shown in chapter 5 in terms of the energetic contributions to the total CP. The chemical pressure approach allows for the partitioning of the total chemical pressure into its potential and kinetic energy contributions. In addition, the major contributions to the potential energy, Hartree, exchange-correlation, and local pseudopotential, can be mapped separately. In this way, the source of both negative and positive pressure appeared at the different chemical entities, like atomic cores, bonds, electron lone pairs, localized and non-localized weak interactions, can be then understood. In this chapter, we analyze the chemical bonding terms of the same crystalline solids that have been previously presented in chapter 5 exploring the separate maps of the kinetic and potential energy contributions. Interestingly, we will see how our analysis leads to particular signatures associated with covalent, metallic, ionic, van der Waals, and H-bond interactions.

In chapter 7, we study the Anions in Metallic Matrices (AMM) model proposed by Vegas *et al.* [123] in the light of the DFT-CP formalism. In the AMM model, the crystal structure of an inorganic compound is viewed as a metallic matrix playing the role of a host lattice controlling the actual positions of the anions. The atomic arrangement in metals leaves empty spaces where we can find inhomogeneities of the electron density [87]. The degree of electron pair localization can be easily determined and displayed graphically by methods such as the electron localization function (ELF) [7]. It was reported by Vegas *et al.* [122] that the ELF is able to identify in a metallic parent structure (Ca) the positions which are occupied by the O atoms in the corresponding inorganic compound (CaO). This is just one example among many others including other pairs such as Na/NaX (X=F, Cl, Br) and BaSn/$BaSnO_3$. In this chapter, we will show how the DFT-Chemical Pressure formalism is able to extend the capability of ELF in the same chemical structures that were presented in the work of Vegas *et al.* [122]. Interestingly, we will see that minima of CP in the metallic matrices are located at the positions that are occupied by the oxygen atoms in the related oxides. Finally, we will present another examples involving alkali and alkali halides crystals.

Overall, our main contribution in this thesis is the presentation of a new tool able to identify and visualize chemical bonding in a wide variety of chemical systems in terms of the basic energetic components involved in the cohesion of crystalline solids. Although electronic structure and chemical bonding formalism constitute the main guiding thread of the document, the thesis has been written trying to organize in an independent manner some of the chapters. Depending on the interest of the reader, each part in which this thesis is divided can be read separately.

Part II

Methodology & Computational Aspects

2 THEORETICAL BASICS

CONTENTS

The fundamental tenet of density functional theory (DFT) is that *any* property of a system of many interacting particles can be viewed as a *functional* of the ground state electron density, that is in principle to say that the electron density gathers all the information of the system. DFT is presently the most popular quantum mechanical method for modeling the electronic structure of large molecules and complex materials. It is nowadays routinely applied to analyze chemical problems concerning, among others, molecular structure and chemical reactivity in organic, organometallic, and inorganic chemistry.

Let us now briefly present the basic concepts from quantum mechanics that underlie density functional theory. In this section, our goal is to give a clear, brief, introductory presentation of the most basic equations important for DFT.

2.1 ELECTRONIC STRUCTURE CALCULATIONS

2.1.1 The Schrödinger equation

The ultimate goal of most appproaches in solid state physics and quantum chemistry is the solution of the time-independent, non-relativistic Schrödinger equation

$$\hat{H}\Psi_i(r_1, ..., r_N, R_1, ..., R_M) = E_i\Psi_i(r_1, ..., r_N, R_1, ..., R_M), \tag{2.1}$$

where $\hat{H}$ is the Hamilton operator for a molecular system consisting of M nuclei and N electrons whose positions are denoted by r_N and R_M, respectively. $\hat{H}$ adopts the following form representing the total energy

$$\begin{aligned}\hat{H} = &-\frac{1}{2}\sum_{i=1}^{N}\nabla_i^2 - \frac{1}{2}\sum_{A=1}^{M}\frac{1}{M_A}\nabla_A^2 - \sum_{i=1}^{N}\sum_{A=1}^{M}\frac{Z_A}{r_{iA}} \\ &+ \sum_{i=1}^{N}\sum_{j>i}^{N}\frac{1}{r_{ij}} + \sum_{A=1}^{M}\sum_{B>A}^{M}\frac{Z_A Z_B}{R_{AB}}.\end{aligned} \tag{2.2}$$

Mass is expressed as multiple of the mass of an electron, atomic units.

In the above equation, A and B denote M nuclei while i and j denote the N electrons of the system. M_A is the mass of nucleus A with nuclear charge Z_A. The first two terms of Eq. 2.2 define respectively the kinetic energy of the electrons and nuclei. The remaining three terms describe the attractive electrostatic interaction between the nuclei and the electrons and the repulsive potential due to the electron-electron and nucleus-nucleus interactions, respectively.

2.1.2 The Born-Oppenheimer approximation

The Born-Oppenheimer approximation allows us to decouple the electronic and ionic motions. Since the number of electrons and ions in a system is very large, an exact quantum mechanical solution of this problem is very complicated. The idea is that the mass of a nucleus is much larger than the mass of an electron, then nuclei move much slower than the electrons. As a result, it is considered that electrons move in a field of fixed nuclei. That way, the kinetic energy of these fixed nuclei is zero and the potential energy due to nucleus-nucleus repulsion is almost constant. Thus, the Hamiltonian given in Eqs. (2.1-2.2) can be further simplified to

$$\hat{H}_{elec} = -\frac{1}{2}\sum_{i=1}^{N}\nabla_i^2 - \sum_{i=1}^{N}\sum_{A=1}^{M}\frac{Z_A}{r_{iA}} + \sum_{i=1}^{N}\sum_{j>i}^{N}\frac{1}{r_{ij}} = \hat{T} + \hat{V}_{Ne} + \hat{V}_{ee}, \tag{2.3}$$

$\hat{V}_{Ne}$ in Eq. 2.3 is called the electronic Hamiltonian. $\hat{T}$ is the kinetic energy operator while $\hat{V}_{Ne}$ is also often termed the external potential, V_{ext}, in DFT.

which and $\hat{V}_{ee}$ operators denote the attractive potential exerted on the electrons due to the nuclei and the electron-electron repulsion, respectively. Consequently, the Schrödinger equation can be expressed as

$$\hat{H}_{elec}\Psi_{elec} = E_{elec}\Psi_{elec}, \tag{2.4}$$

whose solution is the electronic wavefunction Ψ_{elec} and the electronic energy E_{elec}. Then, the total energy can be defined as

$$E_{tot} = E_{elec} + E_{nuc}, \tag{2.5}$$

where E_{nuc} is the constant nuclear repulsion term, $\sum_{A=1}^{M}\sum_{B>A}^{M}\frac{Z_A Z_B}{R_{AB}}$.

2.1.3 The Hohenberg-Kohn theorems

The modern formulation of density functional theory originated in a famous paper written by Hohenberg and Kohn in 1964 [51]. These authors showed that all properties of the system can be considered to be unique *functionals* of the ground state density. Shortly following in 1965, the other classic work of this field by Kohn and Sham [68] appeared, whose formulation of density functional theory has become the basis of much of present-day methods for treating electrons in atoms, molecules, and condensed matter. DFT applies to any system of interacting electrons in an external potential $V_{ext}(r)$, in which the Hamiltonian can be expressed

$$\hat{H} = -\frac{1}{2}\sum_i \nabla_i^2 + \sum_i V_{ext}(r_i) + \frac{1}{2}\sum_{i\neq j}\frac{1}{|\, r_i - r_j \,|}. \tag{2.6}$$

2.1.3.1 *First Hohenberg-Kohn theorem*

See [67, 78] for further information

About 40 years after Thomas-Fermi approximation, the approach of Hohenberg and Kohn appeared to prove for the first time that the electron density can be used to solve the Schrödinger equation (Eq. 2.1) [51]. This first theorem states that "*the external potential $V_{ext}(\vec{r})$ is (to within a constant) a unique functional of $\rho(\vec{r})$; since, in turn $V_{ext}(\vec{r})$ fixes $\hat{H}$ we see that the full many particle ground state is a unique functional of $\rho(\vec{r})$*". The proof of this statement concludes also that the ground state density ρ_0 is uniquely specified from the external potential V_{ext}. Thus, ρ_0 contains the following information

$$\rho_0 \rightarrow N, Z_A, R_A \rightarrow \hat{H} \rightarrow \Psi_0 \rightarrow E_0. \tag{2.7}$$

The total ground state energy (E_0) can be divided into three main components which are consequently a functional of the ground state electron density (ρ_0)

$$E_0[\rho_0] = T[\rho_0] + E_{ee}[\rho_0] + E_{Ne}[\rho_0], \tag{2.8}$$

where T and E_{ee} are respectively the kinetic energy and the electron-electron interaction which are universal quantities since their form is independent of N, R_A and Z_A. These independent terms can be saved into a new term, the *Hohenberg-Kohn functional* $F_{HK}[\rho_0]$. On the other hand, now, the nuclei-electron attractive interaction is defined as $E_{Ne}[\rho_0] = \int \rho_0(\vec{r}) V_{Ne}\, d\vec{r}$. In that way, Eq. 2.8 can be written as

$$E_0[\rho_0] = F_{HK}[\rho_0] + \int \rho_0(\vec{r}) V_{Ne}\, d\vec{r}, \tag{2.9}$$

Although the explicit expressions for both functionals of F_{HK} term are unknown, the $E_{ee}[\rho]$ functional contains information about the electron-electron interaction

$$E_{ee}[\rho] = \frac{1}{2}\int\int \frac{\rho(r_1)\rho(r_2)}{r_{12}} dr_1\, dr_2 + E_{ncl}[\rho], \tag{2.10}$$

where the first term id defined as the classical Coulomb part $J[\rho]$ while $E_{ncl}[\rho]$ is the non-classical part representing the self-interaction correction and exchange correlation.

2.1.3.2 *Second Hohenberg-Kohn theorem*

We have shown that the ground state density determines all the properties. Also it contains information about the nuclear position and its charge. In this second theorem, the authors show how to be sure that a certain density (ρ) is really the ground state density we need. This theorem states that the energy E_0 obtained from the functional $F_{HK}[\rho]$ will be the lowest energy *only* if the density ρ is the ground state density ρ_0. In other words, the energy of a trial density ($\tilde{\rho}$) represents an upper limit to the E_0

$$E_0 \leqslant E[\tilde{\rho}] = T[\tilde{\rho}] + E_{ee}[\tilde{\rho}] + E_{Ne}[\tilde{\rho}], \tag{2.11}$$

Following the variational principle, the E_0 can be written as

$$E_0 = \min_{\Psi \to N} \left\langle \Psi \middle| \hat{T} + \hat{V}_{Ne} + \hat{V}_{ee} \middle| \Psi \right\rangle. \tag{2.12}$$

In other words, according to Eq. 2.12, the minimization problem is carried out through all the allowed antisymmetric N-electron wavefunctions to determine the ground state wavefunction that yields the lowest energy. This variational principle can be also applied to density functional theory through performing two different minimization steps. Then, the E_0 can be expressed as

See [67] for further information

$$E_0 = \min_{\rho \to N} \left(F[\rho] + \int \rho(\vec{r}) V_{Ne} d\vec{r} \right), \tag{2.13}$$

where the universal functional $F[\rho]$ is defined as

$$F[\rho] = \min_{\Psi \to \rho} \left\langle \Psi \middle| \hat{T} + \hat{V}_{ee} \middle| \Psi \right\rangle. \tag{2.14}$$

$F[\rho]$ differs from $F_{HK}[\rho]$ only in that it is defined for all densities come from the antisymmetric wavefunction Ψ.

Hence, for a given density, and upon minimization, the ground state density and the ground state energy are obtained from Eq. 2.13.

2.1.4 Kohn-Sham approach

In this section, we will present some basic expressions reported by Kohn and Sham [68] approaching the hitherto unknown universal functional obtained from Hohnberg-Kohn theorems (See Eqs. 2.8-2.10). As seen in the previous section, the universal functional $F[\rho]$ can be divided into three main terms as

$$F[\rho] = T[\rho] + J[\rho] + E_{ncl}[\rho]. \tag{2.15}$$

As we have discussed before, the only known term is $J[\rho]$ which represents the classical Coulomb interaction while the other two contributions, kinetic energy and the non-classical term due to self-interaction correction and electron correlation effects, still lie in the dark.

The most known reason for failing of Thomas-Fermi model and others is the simple functional expression for the kinetic energy. Then, Kohn and Sham set out to find another way to approach the accurate kinetic energy. The intelligent idea of Kohn and Sham was to calculate as much as possible of the true kinetic energy and then the remainder can be approximated.

In Hartree-Fock scheme, the wavefunction of a reference system of N non-interacting electrons moving in the effective potential V_{HF} can be considered as a single Slater determinant Φ_{SD}. The Hartree-Fock exact kinetic energy for such system is defined as

See chapter 1 of this Ref. [67]

$$T_{HF} = -\frac{1}{2}\sum_{i}^{N}\left\langle \chi_i \middle| \nabla^2 \middle| \chi_i \right\rangle. \tag{2.16}$$

Thus, a Hamiltonian of a non-interacting reference system can be constructed using an effective potential $V_S(r)$ term as follows

$$\hat{H}_S = -\frac{1}{2}\sum_{i}^{N}\nabla_i^2 + \sum_{i}^{N} V_S(r). \tag{2.17}$$

The ground state density of the real, interacting system can be exactly recovered from the KS orbitals by choosing an appropriate effective potential V_S for the following expression

$$\rho_S(r) = \sum_{i}^{N}\sum_{s}\left|\varphi_i(r,s)\right|^2 = \rho_0(r). \tag{2.18}$$

Kohn and Sham suggested to use the same expression of Hartree-Fock method to exactly determine the kinetic energy of a non-interacting reference system. In that way, the remainder of the true kinetic energy along with the non-classical contribution can be gathered in a new defined term, the so-called *exchange-correlation energy*.

Electrons of non-interacting system behave like uncharged fermions so they do not interact with each other.

2.1.4.1 *Kohn-Sham equations*

Let's try now to summarize the Khon-Sham method in some expressions. Recall the Hartree-Fock expression for the kinetic energy on a non-interacting system, then the kinetic energy of non-interacting system of the same density as the real, interacting one can be described using the Kohn-Sham orbitals φ_i instead of the HF spin orbitals χ_i as

$$T_S = -\frac{1}{2}\sum_{i}^{N}\left\langle \varphi_i \middle| \nabla^2 \middle| \varphi_i \right\rangle, \tag{2.19}$$

The true kinetic energy still has a remainder part, T_C, that can not be exactly obtained. Kohn and Sham introduced the functional of Eq. 2.15 using the exchange-correlation contribution as

$$F[\rho] = T_S[\rho] + J[\rho] + E_{XC}[\rho]. \tag{2.20}$$

In other words, the exchange-correlation energy can be defined as

$$E_{XC}[\rho] \equiv (T[\rho] - T_S[\rho]) + (E_{ee}[\rho] - J[\rho]) = T_C[\rho] + E_{ncl}[\rho]. \tag{2.21}$$

Now, the big question is how can we define the appropriate value of the V_S of the real system?. In order to answer this, the energy of the real, interacting system can be written in terms of Eqs. 2.19-2.20:

$$\begin{aligned} E[\rho] =& T_S[\rho] + J[\rho] + E_{XC}[\rho] + E_{Ne}[\rho] \\ =& -\frac{1}{2}\sum_i^N \left\langle \varphi_i \middle| \nabla^2 \middle| \varphi_i \right\rangle \\ &+ \frac{1}{2}\sum_i^N \sum_j^N \int\int \left|\varphi_i(r_1)\right|^2 \frac{1}{r_{12}} \left|\varphi_j(r_2)\right|^2 dr_1\, dr_2 \\ &+ E_{XC}[\rho] - \sum_i^N \int \sum_A^M \frac{Z_A}{r_{1A}} \left|\varphi_i(r_1)\right|^2 dr_1, \end{aligned} \tag{2.22}$$

See [92] for further details.

The minimization of this energy expression by applying the variational principle gives the final KS one-electron equation

$$\begin{aligned} &\left(-\frac{1}{2}\nabla^2 + \left[\int \frac{\rho(r_2)}{r_{12}} dr_2 + V_{XC}(r_1) - \sum_A^M \frac{Z_A}{r_{1A}} \right] \right) \varphi_i \\ &= \left(-\frac{1}{2}\nabla^2 + V_{eff}(r) \right) \varphi_i = \varepsilon_i \varphi_i. \end{aligned} \tag{2.23}$$

The Kohn-Sham orbital of one-electron non-interacting reference is determined by:

$$\hat{f}^{KS} \varphi_i = \varepsilon_i \varphi_i, \tag{2.24}$$

where the Kohn-Sham operator $\hat{f}^{KS}$ defined as

$$\hat{f}^{KS} = -\frac{1}{2}\nabla^2 + V_S(r). \tag{2.25}$$

Comparing Eq. 2.23 with Eq. 2.25, it is very clear that V_{eff} and V_S have the same expression

$$V_S(r) \equiv V_{eff}(r) = \int \frac{\rho(r_2)}{r_{12}} dr_2 + V_{XC}(r_1) - \sum_A^M \frac{Z_A}{r_{1A}}, \tag{2.26}$$

where the first and third terms stand for Hatree ($V_{Hartree}$) and external potential (V_{ext}), respectively. The potential V_{XC} is due to the exchange-correlation energy and it can be defined as

$$V_{XC} \equiv \frac{\delta E_{XC}}{\delta \rho}. \tag{2.27}$$

Up to this point we have established that the Kohn-Sham method would lead to the *exact* ground state density and energy. The *only* term approximated in this method is the exchange-correlation energy E_{XC} and the corresponding potential V_{XC}. Presently, the central challenge of the modern density functional theory is to have better approximations for these two contributions to get closer the really *exact* energy.

2.1.5 Functionals for exchange and correlation

There are several approximations to estimate the exchange and correlation energy to solve the Kohn-Sham equations. Let's briefly present the basis of some of these functionals. Further details regarding to explicit forms for approximation functionals, we refer to some special works [67, 78, 100]

2.1.5.1 *Local density approximation (LDA)*

This was the first approximation developed by Kohn and Sham [68], which gives good results in the electronic structure calculations of molecular and solid crystals. LDA assumes that the electron density in space is similar to that of a uniform electron gas. Therefore, at each point, the exchange-correlation energy $\epsilon_{XC}(\rho)$ of a homogeneous electron gas of density $\rho(r)$ can be used to approximate the $E_{XC}[\rho]$ of a system using the expression:

$$E_{XC}[\rho] = \int \epsilon_{XC}(\rho(r))\rho(r)d^3r, \tag{2.28}$$

Then Eq. 2.27 can be found as

$$V_{XC} = \frac{d}{d\rho}(\epsilon_{XC}(\rho(r))\rho(r)) = \mu_{XC}(\rho(r)), \tag{2.29}$$

where $\mu_{XC}(\rho)$ is the exchange-correlation part of the chemical potential of homogeneous electron gas.

2.1.5.2 *Generalized gradient approximation (GGAs)*

In many cases, LDA is adequate. However, when higher accuracy is needed, one need to go further beyond the LDA. GGA expands the exchange-correlation functional over the gradient of the density. The GGA often gives better results than LDA for structural properties but it overcorrects the LDA bond distances and overestimates by about 2% the experimental values. In addition, it is not sufficient for strongly correlated materials. There are many functionals that are in use today. Perdew *et al.* [97] proposed one functional, PBE, in which some features of his previous one [99] kept unchanged.

2.1.5.3 *Hubbard model: DFT+U method*

This method has been widely used to calculate the correct ground state of strongly correlated materials such as transition metal oxides and systems containing *f*-electrons

like lanthanides and actinides elements. The idea of this method has been derived from the Hubbard model [53]. The additional U term measures the strength of the on-site Coulomb interactions for the localized *d* and *f* electrons. DFT+U corrects the failure of its normal form by constructing an orbital-dependent functional in which the localized electrons (*d* or *f*) are well separated from the delocalized ones (*s* and *p*) since the latter are well described by usual DFT. One promising way to improve these is to use the so-called LDA+*U* and GGA+*U* schemes [24, 136]. In this type of calculations, the spherically averaged screened Coulomb energy (U) and the exchange energy (J) do not enter separately. It is only the difference (U − J) which is meaningful and important for the total LDA/GGA energy functional, entering in the so-called effective Hubbard term U_{eff}.

One expression for LDA+U can be written as

$$E_{LDA+U} = E_{LDA} - \frac{U}{2}N_d(N_d - 1) + \frac{1}{2}U \sum_{i,j i\neq j} n_i n_j, \tag{2.30}$$

where n_i and n_j are *d* (or *f*) occupancies. $N_d = \sum_i n_i$ is the total number of *d* (or *f*) electrons.

2.1.6 To solve Kohn-Sham equations

At this point, we come back to the Kohn-Sham equations and how to solve them to obtain the different physical properties such as energy, forces, stresses, and eigenvalues. So, once we get the effective potential V_{eff} described in Eq. 2.26 we use it to solve the KS one-electron equation 2.23 to determine the orbitals. Consequently, these orbitals are used to determine the ground state electron density and hence the total energy from the expressions 2.18 and 2.22,respectively. Since the V_{eff} depends on the density, the KS one-electron equations must be solved iteratively. This procedure is summarized in the flow chart in Fig. 2.1.

2.1.7 Energy band theory

We have now established how we can solve the Kohn-Sham one-electron equation iteratively (See Fig. 2.1). The knowledge of eigenvalues and eigenfunctions, respectively ε_i and φ_i, of the Kohn-Sham equation 2.24 is necessary to understand different properties of periodic and crystalline solids. Let's summarize how to solve this one-body problem using DFT for the periodic solid systems.

2.1.7.1 *Bloch's theorem*

In periodic structures, atomic positions are repeated in space through applying the cell translations in all directions. The solution of KS equation for such complicated systems is highly facilitated by introducing Bloch's theorem [11]. In periodic crystals, the effective potential (V_{eff}) is periodic and it depends on the crystal structure and its atomic composition, this is called the crystal potential. The latter term is accompanied by other two terms; electronic energy bands and energy gaps. The

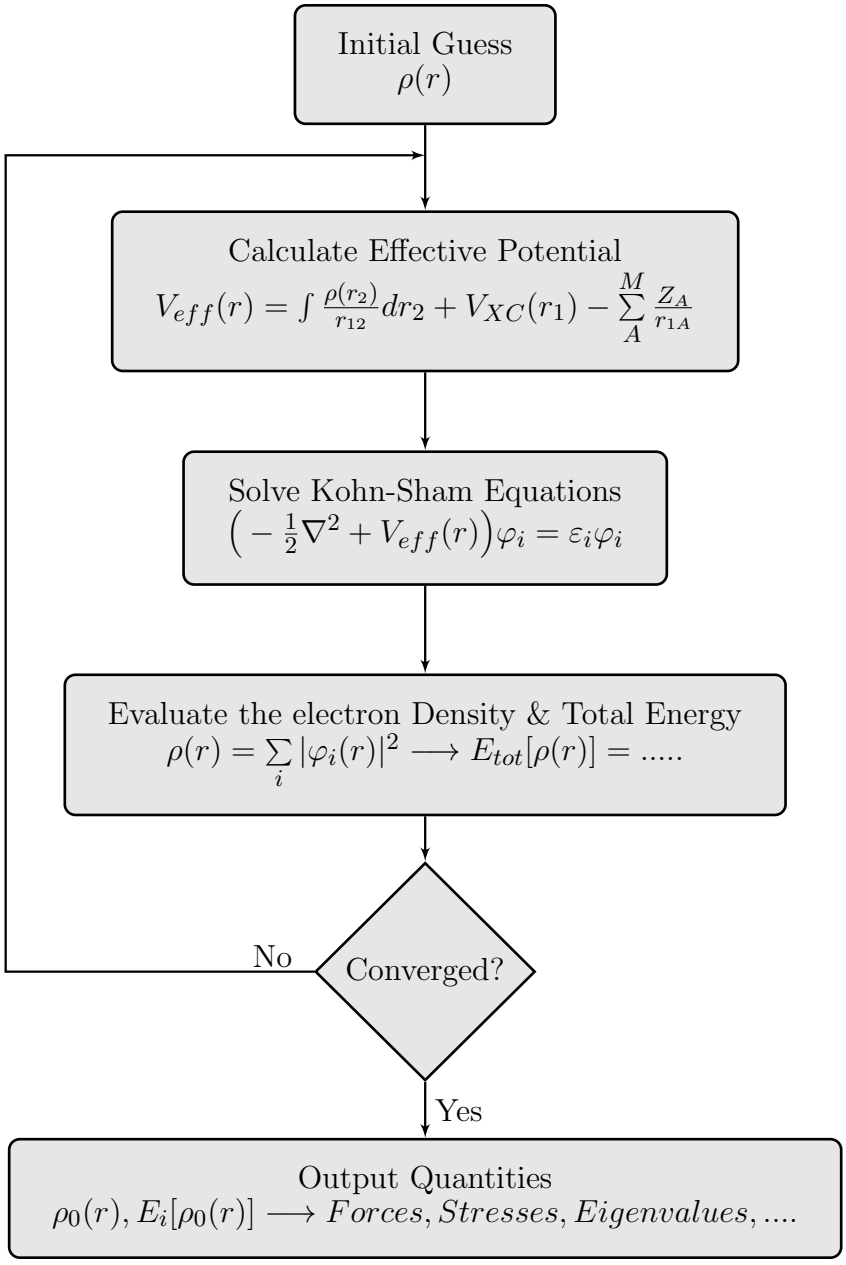

Figure 2.1: Schematic representation of the self-consistent solution of Kohn-Sham equations.

former represents the allowed energy levels while the latter represent the forbidden regions for electrons. The crystal potential can be defined using a lattice vector R:

$$V_{eff}(r + R) = V_{eff}(r). \tag{2.31}$$

Bloch's theorem states that the wave function of an electron moving in a periodic potential should have a form

$$\Psi_k(r) = e^{ik\cdot r}u_k(r), \tag{2.32}$$

where k is a vector of real numbers called the crystal wave vector, r is position, and u_k is a periodic function with the same periodicity as the crystal lattice, which is

See Ref. [78, 100] for further details of the theorem proof.

$$u_k(r+R) = u_k(r). \tag{2.33}$$

For each k-vector, there are several different Bloch waves, i.e. several energy eigenvalues ϵ_{nk}, where n is the band index. Hence, the ϵ_{nk} versus k is understood as the band structure of a solid. So far the k-vector can be anywhere from the reciprocal space. Then, $k+G$ satisfies Bloch's theorem since $e^{ik\cdot r} = e^{i(k+G)\cdot r}$, where G is a reciprocal lattice vector. Hence, all possible Bloch waves occur for k-values within the first Brillouin zone of the reciprocal lattice.

2.1.7.2 *k-points & Brillouin zone*

In principle, the values of k should be chosen to lie in the first Brillouin zone (BZ). The first BZ, or simply BZ, is a uniquely defined primitive cell in reciprocal space. In a periodic system, the solution of Bloch waves are characterized by the behavior of a single BZ. In other words, according to Bloch's theorem, the one-electron wavefunction for a periodic system can be expressed in terms of plane waves as

$$\Psi_{n,k}(r) = \sum_G C_{n,k+G}e^{i(k+G)\cdot r}, \tag{2.34}$$

where the sum runs over the reciprocal lattice vector G. The wavefunction for each value of k can be expanded over a discrete infinite plane wave basis set. This infinite plane wave basis set can be truncated to include only those plane waves of kinetic energy lower than a threshold value, the so-called *cut-off energy* (E_{cutoff}). The E_{cutoff} must be well converged, since such truncation depends on its value.

2.1.8 Pseudopotential approximation

The basic idea of a *pseudopotential* is to simplify the description of complex systems by replacing the strong Coulomb potential of the non-valence electrons of an atom and it's nucleus by an effective potential. Soft pseudopotentials are those with large cut-off radius, that are more rapid, less accurate, and less transferable. Such approximation is widely used in studying different physical and chemical properties of solids. The pseudopotential approximation was first proposed by Hellmann [47], who introduced the first use of pseudopotential in solids [48].

The development of solid-state pseudopotentials underwent a series of evolutions before 1970. The development of pseudopotentials is clearly described in the review of Heine and Cohen [15, 46]. Let's try now to briefly summarize the basis of the two most common forms of pseudopotentials: Norm-conserving pseudopotentials (NCPPs) and Projector augmented waves (PAWs).

2.1.8.1 *Norm-conserving pseudopotentials*

As mentioned by Hammann *et al.* [43], the *good* pseudopotential must fulfill the following requirements:

- Pseudo- and all-electron valence eigenvalues match for an atomic reference state.
- Pseudo- and all-electron wavefunctions match outside certain core cut-off radius r_c.
- The integrated charge for each wavefunction match inside r_c

Since the valence pseudofunction satisfy the orthonormal conditions, the Kohn-Sham equations can be defined by

$$(\hat{f}_{PS}^{KS} - \varepsilon_i)\varphi_i^{PS} = 0, \tag{2.35}$$

with $\hat{f}_{PS}^{KS}$ obtained in the same way using Eq. 2.25 and 2.26 where the V_{ext} in the latter equation is replaced by the pseudopotential.

2.1.8.2 *Projector augmented waves*

Blöchl developed the so called projector augmented waves (PAW) method [12] which combines two advantages over the conventional pseudopotentials method. It allows all-electron calculations and requires a small number of plane waves, i.e. reduced cutoff energy. Thus, it is one of the most accurate methods with the efficiency of the pseudopotential methods.

At this point, the total energy, for example, in the NCPPs approximation can be given by [135]

$$\begin{aligned} E_{tot} =& \frac{1}{2}\sum_j o_j \int |\nabla\tilde{\Psi}_j|^2 + E_{XC}[\rho^e] + \sum_\mu E_\mu^{nl} \\ &+ \int \rho^e \sum_\mu V_\mu^{loc}(r - R_\mu) + \frac{1}{2}\int \rho^e V_H + \sum_{\mu<\nu} \frac{Z_\mu Z_\nu}{R_{\mu\nu}}, \end{aligned} \tag{2.36}$$

where $\tilde{\psi}_j$ and o_j stand for the valence pseudofunction and its occupation, respectively. The first term is positive definite form of the kinetic energy density. The second term is the exchange-correlation energy for the valence electrons. The energy of the nonlocal part of the pseudopotential, the third term of Eq. 2.36, is given by

$$E_\mu^{nl} = \sum_j \sum_\ell \int \tilde{\Psi}_j^* V_{\mu\ell}^{nl}(|r - R_\mu|)\zeta_\ell \tilde{\Psi}_j, \tag{2.37}$$

where $V_{\mu\ell}^{nl}$ is the ℓth component of the nonlocal part of the pseudopotential. ζ_ℓ defines the projection operator on angular momentum ℓ. The fourth and fifth terms represent the electronic interaction with the local part of the pseudopotential

($V_\mu^{loc}(r - R_\mu)$) and with themselves that can be defined as one-half of Hartree potential ($\frac{1}{2}V_H$). The last term represents the ion-ion repulsion. Due to the long-range nature of the last three terms of Eq. 2.36, the evaluation of these terms requires some care. For further details, we refer to these books [63, 78].

2.2 DFT–CHEMICAL PRESSURE ANALYSIS

The DFT-Chemical Pressure (DFT-CP) formalism describes the local pressures in a crystal structure that arise from the atomic size and electronic effects of its constituents. The method is based on the division of the unit cell into *voxels* using the electron density and potential energy grids determined by a DFT calculation. The net pressure is evaluated as an average over the voxels of the unit cell. The evaluation of CP maps require only energy potentials and energy densities of a crystalline solid readily obtained from plane-wave DFT codes, from which the minimized electronic energy is distributed along the points of a voxel grid. Overall, the new CP formalism constitutes a unique alternative to approaches based on the analysis of the electronic wavefunction: not only does it differentiate meaningful chemical entities such as atomic cores, chemical bonds, lone pairs, ions, and atomic or molecular units within a crystal for solids, but it frames them in terms of local forces leading to the equilibrium structure. In general, the CP map involves a positive pressure near the atomic cores and a negative pressure along the bonds and in the interstitial spaces.

The computational package is available at the author's research group's homepage: `http://www.chem.wisc.edu/~danny`.

In this chapter, we are concerned to show the main features of the CP methodology as well as its theoretical background as regards the calculation of the local pressures within a solid crystal structure. Besides, we will show the basis of implemented methods used to enhance the accuracy of the results of the CP methodology. Some issues associated with the interpretation of the pressure maps will be discussed by the end of this chapter.

2.2.1 Chemical Pressure from μ_2-Hückel model

A simple theoretical approach to exploring the combined effects of electronic and atomic size is offered by the Chemical Pressure analysis proposed by Fredrickson *et al.* [33, 44]. The dense atomic packing in intermetallic structures can lead to strong correlations between interatomic distances. Such correlations make it difficult to independently optimize all the bonding distances. The atomic size affects reaching the ideal distances (Figure 2.2b) which requires shortening neighboring contacts with little electronic support, and consequently a tension arises. This fact was termed as *electronic packing frustration* (EPF). Such tension would be expected to result in *chemical pressure* (CP) along the non-ideal interatomic distances.

To illustratic the basics of this approach, the classic Hückel model will be used [54, 55]. The DFT-CP uses the ability to decompose the total energy into a sum over a spatial distribution of contributions to the energy, in this case bonds and onsite

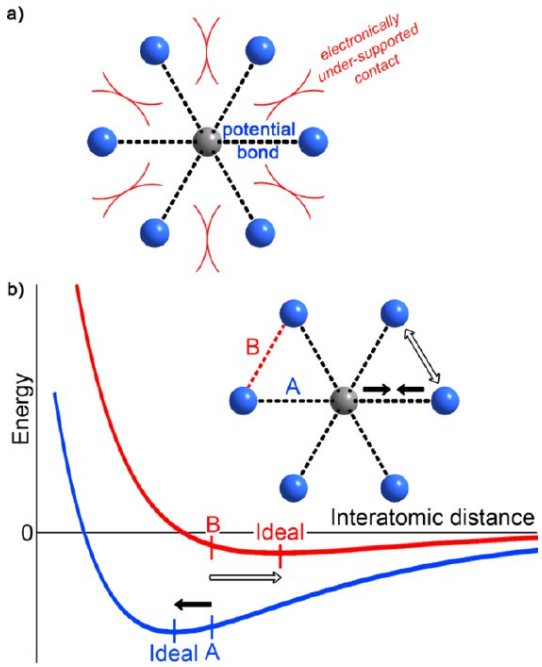

Figure 2.2: Non-ideal interatomic distances resulting from electronic packing frustration (EPF). (a) The electronic packing frustration model. (b) The correlation between the interatomic distance needed to be compressed (A) and expanded (B). The chemical pressure at a contact is obtained as the slop of the energy vs distance curve at that contact. Quoted from Ref. [26] with the kind permission of the American Chemical Society.

terms. The total energy can be expressed as a sum of on-site and bonding interaction terms [33, 73]:

$$E_{\mu_2-\text{Hückel}} = \gamma\mu_2 + E_{\text{Hückel}} = \sum_i \sum_j (\gamma H_{ij}^2 + (\sum_n o_n c_{n,i}^* c_{n,j}) H_{ij}), \tag{2.38}$$

where γ is a proportionality constant and $E_{\text{Hückel}}$ is the sum of the electrons energy from a simple Hückel calculation. $c_{n,j}$ is the coefficient of atomic orbital j in crystal orbital n, and o_n is the occupancy of that crystal orbital. Since the total energy is related to pressure by $P = -\partial E_{total}/\partial V_{cell}$, the pressure can be distributed in the following way:

$$\begin{aligned} P &= -\frac{\partial E}{\partial V} = -\sum_i \sum_j \frac{\partial}{\partial V}(\gamma H_{ij}^2 + (\sum_n o_n c_{n,i}^* c_{n,j}) H_{ij}) \\ &= \frac{1}{N_{orb}} \sum_i \sum_j p_{ij} \end{aligned} \tag{2.39}$$

where N_{orb} is the number of orbitals in the crystal, and p_{ij} is the pressure between two interacted orbitals i and j. In other words, the total pressure, within this method, can be expressed as an average of the CP contributions of bonding interactions.

2.2.2 Chemical Pressure from DFT

The simple Hückel method has several advantages, such as accuracy, and transparency between geometry and electronic structure, in investigating EPF and the creation of the CP analysis. However, it would be expected to fail in the more complex crystal structures displaying many symmetry-distinct sites. To realize the meaning of the DFT-Chemical Pressure analysis, let us extensivly show the theoretical basis of this method and how the CP results are extracted from the output of an electronic structure calculation.

We start with the total energy expression of the Kohn-Sham DFT which can be similarly decomposed, like in the Hückle model, into spatial contributions to the energy [34, 78]:

$$E_{DFT} = \iiint_{cell} \left(\frac{1}{2} \sum_j o_j |\nabla \psi_j|^2 + (v_{local} + \frac{1}{2} v_{Hartree} + \epsilon_{XC}) \rho(\vec{r}) \right) dV + E_{Ewald} + E_\alpha + E_{nonlocal}, \tag{2.40}$$

where o_j is the occupancy of the one electron eigenfunction ψ_j. The terms under the integral correspond respectively to the kinetic energy of the system, the interaction energy of the electrons with the local components of the atomic pseudopotentials, the electron-electron interaction energy, and the exchange-correlation energy. The last three terms in the integral are the main local contributions to the potential energy which is measured relative to a reference state of a homogeneous exchange-correlation free electron gas containing the ion cores. The energy of that reference state is given by the sum of the first two terms outside the integral while $E_{nonlocal}$ represents the interaction energy of the electrons with the nonlocal components of the pseudopotential. An additional term, $E_{-kT.Entropy}$ may be added to correct the total energy from the band occupancies smearing at the Fermi level. The terms outside the integral are difficult to be apportioned over specific region of space.

The DFT total energy has several components, many of which can be represented as the integral over an energy density function, ρ_{energy}. These mappable terms allow us to define kinetic ($\rho_{kinetic}$), Hartree ($\rho_{Hartree}$), local pseudopotential (ρ_{psp}) and exchange-correlation (ρ_{XC}) energy densities. In addition, the total energy contains remainder terms such as Ewald and non-local contributions involved in the valence electron-pseudopotential interaction. These are treated as a homogeneous background energy to create an energy map whose integral over the unit cell gives the correct total energy [26]:

$$E_{DFT} = \iiint_{cell} \rho_{energy}(\vec{r})\, dV + E_{remainder}, \tag{2.41}$$

Since the method divides the unit cell into a high number of finite volume elements, *voxels*, a sum over the voxel energies can be then used in place of the intgral,

$$\begin{aligned} E_{DFT} &\simeq \sum_{n}^{N_{voxel}} \rho_{energy}(\vec{r}_n) V_{voxel} + E_{remainder} \\ &= \sum_{n}^{N_{voxel}} E_n + E_{remainder}, \end{aligned} \tag{2.42}$$

where N_{voxel} is the number of voxels, in which the unit cell is partitioned, each of volume V_{voxel}, i.e. $V_{cell} = N_{voxel} \cdot V_{voxel}$. E_n is the total mapped energy associated with every voxel, and $E_{remainder}$ contains the total non-mapped energy contributions.

This spatial resolution of the total energy allows a similar decomposition of the (internal) pressure:

$$\begin{aligned} P &= -\frac{\partial E_{DFT}}{\partial V_{cell}} = -\frac{\partial}{\partial V_{cell}} \left(\sum_{n}^{N_{voxel}} E_n + E_{remainder} \right) \\ &= -\sum_{n}^{N_{voxel}} \frac{\partial E_n}{N_{voxel} \partial V_{voxel}} - \frac{\partial E_{remainder}}{\partial V_{cell}} \\ &= -\frac{1}{N_{voxel}} \sum_{n}^{N_{voxel}} \frac{\partial E_n}{\partial V_{voxel}} + P_{remainder} \\ &= \frac{1}{N_{voxel}} \sum_{n}^{N_{voxel}} P_n + P_{remainder}, \end{aligned} \tag{2.43}$$

where the macroscopic internal pressure is represented by an average (rather than sum, reflecting that pressure is an intensive property) over a pressure grid, with a homogeneous background pressure, $P_{remainder}$ (arising from the $E_{remainder}$ term of the energy), being added uniformly to all points of the pressure grid.

The key step in this calculation of partial derivatives of the voxel energies with respect to a grid's voxel volume is to give a chemical pressure of a specific voxel (P_n). In practice, these voxel pressures can be obtained by taking the difference in energies calculated for that voxel in structures that are slightly expanded (+) and contracted (-), isotropically:

$$P_n \simeq -\frac{E_n^+ - E_n^-}{V_{voxel}^+ - V_{voxel}^-}. \tag{2.44}$$

Each of the energy density terms gives a corresponding contribution to the voxel pressures, meaning that individual maps can be made for, say, the kinetic energy and local pseudopotential components to the chemical pressure. The average over these grid pressures yields the system pressure, which for a material at equilibrium with its surrounds [102] will equal the external pressure. At zero pressure, this means that regions with negative and positive chemical pressure features of a system should cancel each other to fill the mechanical equilibrium condition.

2.2.3 CP maps with grid unwarping

In our application of this analysis, we have obtained a strong CP features near the atomic core regions while the interstitial regions are much more shallow, as was discussed before by Berns *et al.* [8]. Such extreme magnitudes of CP causes a number of problems in the interpretation of the CP results. These core pressures make it difficult to detect other subtle features in the interatomic regions and the pressure directionality near the core region. A central question that was answered by Berns *et al.* [8], that if these strong CP oscilations near the atomic core regions represent the atomic interactions or are instead a result of the pseudopotential models used in the generation of the CP maps. Isolated systems, in which the interactions between atoms are absent, were studied for different atoms in large unit cells. The CP maps show a common features that the atomic positions are decorated by intense pressure near the atomic cores (See Figure 2 in Ref. [8]). An example for the effect of the unwarping method on the CP features is presented in Fig. 2.3 in which CP maps of the *bcc*-Na unit cell involving different number of valence electrons are shown.

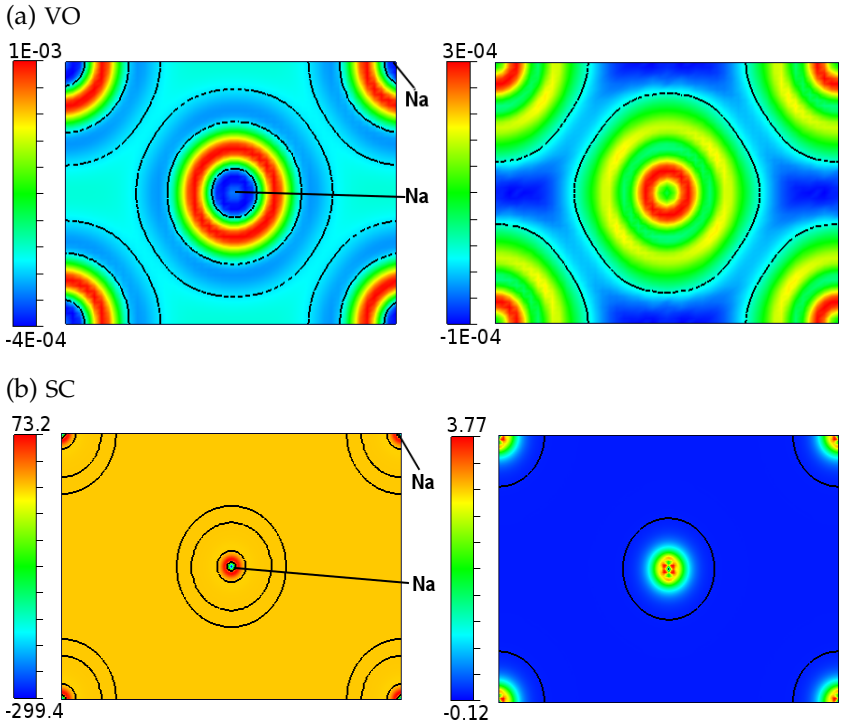

Figure 2.3: The DFT-CP maps calculated for *bcc*-Na crystal. Cross sections through the plane (101) (left) without (right) with applying the unwarping process near the atomic core regions. VO and SC refer to the valence-only and semi-core pseudopotential of Na, respectively. Black contours drawn for CP = 0 to indicate transitions between negative and positive CP values.

Moreover, The isotropic intense pressures arising near the atomic cores should be reduced in a way to allow more subtle features to be visible. This can be achieved by including an additional step in the DFT-CP method: unwarping procedure. According to Berns *et al.* [8], the unwarping procedure is based on calculating the voxel pressure in terms of its nearby atom j. To determine the closest atomic core to a certain voxel, several methods can be used, such as Hirshfeld method [50] that

will be described later in this chapter. The voxel centers in the expanded ($\vec{r}_n^{+}$) and contracted ($\vec{r}_n^{-}$) structures are then shifted in terms of their nearby atom's position in the equilibrium structure. Then the pressure of voxel can be calculated in terms of eq. 2.44 can be written as following:

$$P_n \simeq -\frac{\{\rho^{+}_{energy}(\Delta\vec{r}^{\circ}_n + \vec{r}^{+}_j) - \rho^{-}_{energy}(\Delta\vec{r}^{\circ}_n + \vec{r}^{-}_j)\}V^{\circ}_{voxel}}{V^{+}_{voxel} - V^{-}_{voxel}}, \tag{2.45}$$

where ρ^{+}_{energy} and ρ^{-}_{energy} are the energy density of the expanded and contracted structure. In the application of this method, it will be more complicated to calculate the energy density at $\Delta\vec{r}^{\circ}_n + \vec{r}^{+}_j$ and $\Delta\vec{r}^{\circ}_n + \vec{r}^{-}_j$ since will often lie in between the grid points. An estimated value can be obtained using the trilinear interpolation. The error in the total energy obtained by the integration over the voxel grid is very small and can be added homogeneously to the CP map.

We show in Figure 2.3 a and b how the CP distribution changes upon applying the unwarping procedure. Our results show that the final pressures in both cases (with and without unwarping) are same and equal to zero. The correction leads to a significant change in the CP maps. The strong core-like features around the atomic positions are replaced with flatter and less isotropic features. This allows more subtle features to come to the foreground.

On the other hand, applying the unwarping procedure to voxels in the interstitial regions will be more complicated since the energy density features might be expected to show a reasonable change with the volume of the structure. The previous mentioned vectors of eq. 2.45, $\Delta\vec{r}^{\circ}_n + \vec{r}^{+}_j$ and $\Delta\vec{r}^{\circ}_n + \vec{r}^{-}_j$, will be needed to be weighted as the atoms will shift to different positions in the expanded and contracted structures. Hirshfeld method [50] can be used to determine these weights as will be described below. Such weighing factor is not important at all for voxels near atomic core regions where the electron density changes in a very small range as the structure is expanded or contracted.

2.2.4 Hirshfeld approach in grid unwarping between atoms

In Hirshfeld method, the electron density at every voxel can be distributed among several atoms depending on their free-atom (FA) densities at certain distances from the nuclear positions. These contributions are then translated into relative weights in terms of the true electron density distribution between the atoms. Hirshfeld weight $w_{j,n}$ for the effect of an atom j on a voxel n is expressed as following:

$$w_{j,n} = \frac{\rho^{FA}_j(\vec{r}^{\circ}_n)}{\sum_x^{\text{all atoms}} \rho^{FA}_x(\vec{r}^{\circ}_n)}, \tag{2.46}$$

These weights are used by a voxel to maintain its equilibrium position as the cell expanded and contracted in the calculation of CP maps. Then the voxel posi-

tion in the extracted and contracted structures are calculated in the following way respecting the effect of the nearby atomic centers:

$$\vec{r}_n^{+} = \sum_{j}^{all\,atoms} w_{j,n} \cdot \left(\Delta\vec{r}^{\circ}_{n,j} + \vec{r}_j^{+}\right), \tag{2.47}$$

$$\vec{r}_n^{-} = \sum_{j}^{all\,atoms} w_{j,n} \cdot \left(\Delta\vec{r}^{\circ}_{n,j} + \vec{r}_j^{-}\right), \tag{2.48}$$

In the application of this procedure between the atomic centers, the voxel centres are no longer uniformly distributed, and the their volumes vary throughout the structure. Following the special treatment for the voxels located at the interstitial spaces, Eq. 2.45 slightly changes to:

$$P_n \simeq -\frac{\rho^{+}_{energy}(\vec{r}_n^{+})V_n^{+} - \rho^{-}_{energy}(\vec{r}_n^{-})V_n^{-}}{V^{+}_{voxel} - V^{-}_{voxel}}, \tag{2.49}$$

where V_n^{+} and V_n^{-} are the volume of voxel n in the expanded and contracted structures, while V^{+}_{voxel} and V^{-}_{voxel} represent the average voxel volumes in the two structures.

The unwarping procedure results in a less isotropic CP features near the atomic cores. The CP maps become more intuitive to detect the variations in CP near the nuclei and in the interstitial spaces. This also will be reflected through the integration of the atomic pressure its directionality.

2.2.5 Integration of CP around atoms

The results of the unwarping method are characterized by a region of positive pressure surrounding the nuclei embedded in a background of negative pressure (See Figure 2.3). The integration of the CP around the atom's position reveals the directionality and the overall pressure exerted on each atom. The method determines the pressures experienced by each atom along different directions. Now, we will show the integration procedure in details as proposed by Engelkemier *et al.* [26]. The first step is to project the CP distributions around an atom onto spherical harmonics:

$$a_{lm} = \frac{1}{N_{voxels,atom}} \sum_{n} w_{n,atom} P_{voxel,n} Y_{l,m}(\theta_n, \phi_n), \tag{2.50}$$

where $w_{n,atom}$ is the fraction of voxel n's pressure attributed to specific atom, $N_{voxels,atom} = \sum_n w_{n,atom}$ is the number of voxels associated to this atom, and (θ_n, ϕ_n) are the spherical angular coordinates of voxel n from the nucleus position as origin. The projection a_{lm} can be used to construct the CP anisotropy, $CP_{anisotropy}(\theta, \phi)$, of the atom as follows:

$$CP_{anisotropy}(\theta, \phi) = \sum_{l=0}^{\leqslant l_{max}} \sum_{m=-l}^{l} a_{lm} Y_{l,m}(\theta, \phi), \tag{2.51}$$

where l_{max} is the highest index for spherical harmonics included in the integration and m values are automatically generated in terms of the predefined l_{max}. For convenience, the spherical harmonics for $l = 0$ is given as $Y_{0,0} = \frac{1}{\sqrt{4\pi}}$, then the projection a_{00} is calculated using Eq. 2.50

m = -l, (-l+1), ..., (l-1), l.

$$a_{00} = \frac{1}{N_{voxels,atom}} \sum_{n} w_{n,atom} P_{voxel,n} \frac{1}{\sqrt{4\pi}} = P_{atom} \frac{1}{\sqrt{4\pi}}, \tag{2.52}$$

where P_{atom} is the nominal average pressure experienced by the atom. The anisotropy function is then calculated according to eq. 2.51 as follows

$$CP_{anisotropy}(\theta, \phi) = P_{atom} \frac{1}{\sqrt{4\pi}} \cdot \frac{1}{\sqrt{4\pi}} + ... = \frac{P_{atom}}{4\pi} + ... \tag{2.53}$$

Now, the net pressure along each direction, $P_{atom}(\theta, \phi)$, can be calculated from the previous equation by multiplying the anisotropy function by 4π, i.e.

$$P_{atom}(\theta, \phi) = 4\pi \cdot CP_{anisotropy}(\theta, \phi). \tag{2.54}$$

The numerical values of $P_{atom}(\theta, \phi)$ can be then easily represented graphically using radial plots. The integrated CP surface around each atom is plotted to a point with spherical coordinates (θ, ϕ) is proportional to the magnitude of the CP experienced by the atom along that direction. The color of the surface indicates the sign of the pressure. Black for negative and white for positive pressures. The negative pressure is located along directions through which the contraction would be favorable, while the positive pressure reflects the priority to expand.

2.2.6 Contact volumes based on Hirshfeld approach

The pressure between two atoms is given by

$$P_{jk}^{contact} = \sum_{n}^{N_{voxels}} w_{jk,n} P_n, \tag{2.55}$$

where $w_{jk,n}$ is the fraction of voxel n's pressure associated to the region of interaction between the two atoms. In homogeneous systems that include only one atom type, the following simple scheme can be used to determine the proper weight for every voxel's pressure,

$$w_{jk,n} = \left\{ \begin{array}{cc} 1, & \text{if atoms j and k are two closest to voxel n} \\ \frac{1}{m}, & \text{if m contacts are tied in above criterion} \\ 0, & \text{if j or k are not two atoms closest to voxel n} \end{array} \right\} \tag{2.56}$$

In heterogeneous systems which display different atom types, the previous weighting scheme should consider the differing effects of different atom types. To fulfil this

task, the sizes of the free-atom (FA) electron densities must be considered in determining the weights.

$$w_{jk,n} \propto \rho_j^{FA}(\vec{r}_n) \cdot \rho_k^{FA}(\vec{r}_n). \tag{2.57}$$

The weighting scheme of Eq. 2.56 could then be expressed in terms of the free-atom electron density of the two atoms as follows:

$$w_{jk,n} = \left\{ \begin{array}{ll} 1, & \text{if } \rho_j^{FA}(\vec{r}_n)\rho_k^{FA}(\vec{r}_n) \text{ is largest for j, k pair} \\ \frac{1}{m}, & \text{if m contacts are tied in above criterion} \\ 0, & \text{if } \rho_j^{FA}(\vec{r}_n)\rho_k^{FA}(\vec{r}_n) \text{ is not largest for j, k pair} \end{array} \right\} \tag{2.58}$$

The distance-based and Hirshfeld-inspired integration approaches based on the weighting scheme of eq. 2.56 and 2.58,respectively.

In addition, several structures were studied by Berns *et al.* [8] to illustrate the results of performing the two different integration methods. It was concluded that the use of this improved scheme, Hirshfeld-inspired contact volumes, incorporate the differing influence of different atom types in the construction of contact volumes and the integration of interatomic pressures.

2.2.7 Mapped and non-mapped contributions to chemical pressure (CP)

As described in the previous sections, the DFT total energy can be divided into two main parts, one is the mapped energy (E_n) which contains the energetic contributions that can be mapped over the voxel grids, such as kinetic energy (KE), exchange-correlation energy (XC), local pseudopotential energy (Local PSP), and Hartree energy. The other part is the non-mapped energy ($E_{remainder}$) which contains energetic contributions that are not easily traced to specific points in space, such as the Ewald energy and nonlocal components of the potential energy (See eq. 2.42).

The voxel energy can be expressed in terms of the contributions as follows

$$E_n = E_{kinetic,n} + E_{local,n} + E_{Hartree,n} + E_{XC,n}, \tag{2.59}$$

Each contribution to the voxel energy E_n can be computed separately in the following way [34]:

$$E_{kinetic,n} = \rho_{kinetic,n} V_n, \tag{2.60}$$

$$E_{local,n} = \nu_{local} \rho_n V_n, \tag{2.61}$$

$$E_{Hartree,n} = \frac{1}{2} \nu_{Hartree} \rho_n V_n, \tag{2.62}$$

where ρ_n and $\rho_{kinetic,n}$ are the electron density and the kinetic energy density at voxel n of volume V_n. E_{XC}, n is determined from the exchange-correlation functional as $\epsilon_{XC}(\rho_n)V_n$.

The pressure distribution of each energetic contribution to the total mapped energy over the voxel grids can be then calculated in a similar way used in eq. 2.44:

$$P_{j,n} = -\frac{E^{+}_{j,n} - E^{-}_{j,n}}{V^{+}_{voxel} - V^{-}_{voxel}}, \tag{2.63}$$

where j is one of the four mapped terms, KE, Local PSP, Hartree, and XC. The total mapped pressure at each voxel P_n is given by the following expression

$$P_n = \sum_{j=1}^{4} P_{j,n}, \tag{2.64}$$

According to eq. 2.43, the total (internal) pressure P can then be expressed as follows

$$P = \frac{1}{N_{voxels}} \sum_{n}^{N_{voxels}} \sum_{j=1}^{4} P_{j,n} + P_{remainder}. \tag{2.65}$$

In the application of this decomposition of the total mapped energy E_n, we have created separate CP map for each contribution independently. Over the course of our analysis of the contributions to chemical pressure, we have examined the source of the positive and negative CP regions within the crystalline space. Also we have investigated the behavior of CP contributions of various types of chemical bonding, including localized and delocalized covalent bonds.

3 COMPUTATIONAL PROCEDURE

CONTENTS

3.1 ELECTRONIC STRUCTURE CALCULATIONS

Electronic structure calculations were performed under the formalism of the density functional theory using plane waves basis sets and the pseudopotential scheme as implemented in standard computational packages. Several approximations for the exchange-correlation energy were tested depending on the case of study. All unit cell geometries and atomic positions were optimized. Besides, the structural relaxation was performed for the systems until the maximal forces on the atoms were less than 10^{-5} Hartree/Bohr. The total energy was converged with respect to cutoff energies and Monkhort-Pack k-point grids to at least 10^{-4} Hartree/formula unit. In this thesis, we used two computational packages to fulfill our aims. More details are given in the following sections.

3.1.1 The Vienna Ab initio Simulation Package (VASP)

To illustrate electronic structure calculations using the VASP [12, 70, 71] code, the cesium uranyl tetrachloride crystal is selected. We examined different DFT+U levels of calculation following previous reported analysis in solid UO_2 [22, 130], with explicit comparisons with available experimental and theoretical data [128, 137]. Along with this particular parameter of the uranium-based crystal, our computational study includes the projector-augmented wave (PAW) pseudopotential scheme and testing several exchange-correlation functionals. Brillouin-zone integrals were approximated using Γ-centered Monkhorst-Pack meshes [83] where the numbers of subdivisions along each reciprocal lattice vector $\vec{b_i}$ were given by $N_i = \max(1.15 \times |\vec{b_i}| + 0.5)$. The wavefunction was expanded in plane waves up to a cutoff energy of 520 eV to ensure convergence of the total energy.The final computational parameters were selected after careful comparison with the available experimental data.

Lattice parameters and atomic positions were optimized at selected pressures in the range of $0-50$ GPa. This is followed by single-point calculations using the optimized parameters at each pressure. The resulting lattice parameters, volumes, total energies, bond distances, and bond angles were extracted for all the geometries to be represented in 1D plots or to be used in further calculations. The charge density for each geometry is obtained as well to be analyzed topologically.

3.1.2 ABINIT package

We used `ABINIT` program [39–41] to prepare the raw data for the DFT-CP analysis. All the calculations were performed using the LDA exchange-correlation functional of Goedecker, Teter, and Hutter [38] and the Hartswigen-Goedecker-Hutter (HGH) pseudopotentials provided by the package [45]. The geometrical optimization was performed at zero pressure via Broyden-Fletcher-Goldfarb- Shanno minimization technique [30]. This is followed by three single-point calculations spanning a small volume range of 3% around the corresponding equilibrium crystal structure. `ABINIT` offers options for the output of electron densities, kinetic energy density, the total Khon-Sham potential, and two of its components, Hartree and exchange-correlation potentials. These outputs are given in real space by using a chosen Fast Fourier Transform (FFT) grid in which the unit cell is partitioned into voxels.

In order to get the required data mentioned above for CP analysis, one needs to add the following input variables to the normal single-point input of `ABINIT`:

```
ngfft xx xx xx       # The size of the fast Fourier transform in three dimensions.
                     # Otherwise ABINIT will sometimes choose different grids for each scale.
ndtset 3             # Number of data sets to be treated.
scalecart1 3*1.005   # Expanded until cell volume.
scalecart2 3*1.000   # Equilibrium unit cell volume.
scalecart3 3*0.995   # Contracted unit cell volume.
prtpot 1             # Print the Kohn-Sham potential output file.
prtvha 1             # Print the Hartree potential output file.
prtvhxc 1            # Print the sum of the Hartree and XC potential output file.
usekden 1            # Compute the kinetic energy density during the self-consistently loop.
prtkden 1            # Print the kinetic energy density in real space output file.
prtwf 0              # Do not print the wavefunction output.
                     # These are large and not used in the calculation.
```

Once we obtain these output files, with the suffix **`_POT`**, **`_VHA`**, **`_VHXC`**, and **`_KDEN`**, we can run the CP program to generate the CP maps. This is the general procedure we used to prepare the input data for the CP analysis of all the systems studied in this thesis. The same computational strategy can be followed for any other crystalline system.

3.2 CHEMICAL PRESURE CALCULATIONS

At this point, we have provided how to obtain the main data for the CP program [8] to create the CP maps. Several versions of the DFT-CP program have been published. All the results presented in this thesis were obtained using the last version, `Version` 3.0 [25]. In this section, we show how to run the CP programe and how to control different input parameters to obtain the desired CP results.

The interactive mode of the CP program is used to select the mapped energy components. Then, the first step is to run the CP program and identify the required inputs, i.e. the outputs of `ABINIT`. There are two ways to create the CP maps:

- USING THE DEFAULTS
  By default, The CP program uses the core unwarping method to create the total CP map in which all the energetic components, kinetic (KE), local pseudopotential (Local PSP), Hartree , and exchange-correlation energy (XC), are mapped. Besides, the non-mapped components, Ewald and non-local contributions of the pseudopotential energy term, are treated as a homogeneous background energy, as previously discussed in section 2.2.2. The preferred partitioning scheme is the Hirshfeld scheme described in section 2.2.4, which is used by default along with the highest spherical harmonics onto which the CP will be projected (l=6). In this case, the CP program will ask for the free-atom electron density profiles (ρ_j^{FA}) that must be named with a special format. If we use hydrogen as an example, the name of the file would be `H_rho_r.txt`. This can be found at the `ABINIT` website. The above mentioned procedure can be achieved by responding to the following queries:

See http://www.abinit.org/downloads/all_core_electron

```
What is the prefix of your Abinit _o_ files ?
What is the name of your Abinit outfile?
Choose a name for your CP output files:
Would you like to use the defaults?  [yes/no]
```

  Then the user will be asked for the atomic density profiles:

```
Reading files.  Please wait a moment to enter profile names...
Enter the name of the Hirshfeld profile for atom #1 (X, Y equivalent sites):
```

  where X and Y will be changed to the atomic symbols and the number of equivalent sites in the unit cell, respectively.

- OTHER OPTIONS
  Instead of having only one CP map for all the mapped and non-mapped energetic contributions, CP program can also produce one CP map for each energetic term of the total mapped energy defined in Eq. 2.59 by using the non-defaults of CP program. In this way, a new list of queries (see below) will appear. The user is required to respond one by one.

  Thus, it is possible to select energetic contributions which are mapped, to turn off the core unwarping step, to select another way to handle the non-mapped energy, or even to change the partitioning scheme. It is worth to mention that one may choose to printout other additional maps in the `.xsf` format which can be visualized by `VESTA` program [82].

Whatever the options the user chooses to run the CP program, the CP calculations will output several files with different types of information. Below, the contents of the output files are briefly described.

- **`-cplog`** is the log file that contains the numerical values of CP for all the energetic contributions and the integrated CP around each atomic center.

```
Map kinetic energy?  [1=Yes] [2=Thomas-Fermi]
Map local energy?  [1=Yes]
Map Hartree energy?  [1=Yes]
Map exchange-correlation energy?  [1=Yes]
Use core unwarping (recommended)?  [1=Yes]
Restore symmetry (recommended)?  [1=Yes]
Add unmapped pressure homogeneously?  [1=Yes]
Substract it homogeneously instead?  [2=Yes]
Ignore it instead (not recommended)?  [3=Yes]
Partition scheme?  [1=Hirshfeld] [2=Distance]
Percent tolerance?  [1=Default]
Max l for spherical harmonics?  [6=Default]
Use datasets other than 1 through 3?  [1=Yes]
Output potential maps as XSF files?  [1=Yes]
Output total energy maps?  [1=Yes]
Output map of new voxel volumes?  [1=Yes]
Output voxel weight maps?  [1=Yes]
```

- **-CP.xsf** is the resulting CP map that can be visualized with VESTA program.
- **-geo** contains the Cartesian coordinates of atoms within a unit cell, in Angstrom.
- **-cell** contains the lattice parameters of the unit cell, in Angstrom.
- **-coeff** contains the numerical values of the integrated CP for all possible spherical harmonics depending on the maximum value that has been defined.

Now, the CP calculations are completed and it is time to analyze the results.

3.3 ANALYZING CHEMICAL PRESSURE RESULTS

The output of DFT-CP program, **-CP.xsf**, can be analyzed and represented in many different ways. One-, two- and three-dimensional plots can be used. In this thesis, we use the three types to represent and discuss our results. The 1D profiles show clearly how the CP varies, say between two atoms or along certain direction. The 2D CP maps, sometimes called cross-sections, can include atoms and bonds with color indicating the value of the pressure at each point in space over a certain pressure range. For wide CP ranges, it is important to rescale the CP range to a narrower one to allow the more subtle features of these maps to be visible. The CP distributions within a unit cell can also be visualized with isosurfaces in 3D plots. In the latter, we use white and black colors for positive and negative CP, respectively.

A copy of figuretool.m template has been sent to us by Prof. Daniel C. Fredrickson.

Moreover, the rest of the outputs mentioned above can be used to analyze the anisotropy within a solid. The integrated CP around the atomic centers are visualized by MATLAB program using *figuretool.m* template. To run this template in MATLAB, the prefix of the CP outputs should be defined in the "CPfile" parameter of the *figuretool.m* file. In addition, by reading the **-CP.xsf** with VESTA, the portion of the unit cell that you would like to visualize must be selected, and exported as an **.xyz** file. The latter is then introduced in the "template" parameter of the *figuretool.m*. The anisotropy is represented using the same colors of the isosurfaces in the 3D plots.

3.4 OTHER PACKAGES

Other programs were used for different purposes. Below, we give short notes about the usage of these additional packages in our work.

3.4.1 GIBBS program

The equation of state (EOS) is a thermodynamic equation describing properties of solids with respect to changes in the macroscopic variables (p, V, T). GIBBS [10] can analyze the output of electronic structure calculations using a set of energy-volume (E–V) data using a selected form of EOS. The equilibrium volume, bulk modulus (B_0) and its pressure derivative (B_0'), both evaluated at zero pressure, were obtained by fitting the 4^{th} order static Birch-Murnaghan EOS [9] to the calculated (E–V) data set. We applied this method to the (E–V) data obtained from the electronic structure calculations of $Cs_2UO_2Cl_4$ crystal under hydrostatic pressure.

The 4^{th} order Birch-Murnaghan EOS takes the form

$$E = E_0 + \frac{3}{8}V_0B_0f^2\{(9H - 63B_0' + 143)f^2 + 12(B_0' - 4)f + 12\}, \tag{3.1}$$

$$p = \frac{1}{2}B_0(2f+1)^{5/2}\{(9H - 63B_0' + 143)f^2 + 9(B_0' - 4)f + 6\}, \tag{3.2}$$

$$\begin{aligned} B =& \frac{1}{6}B_0(2f+1)^{5/2}\{(99H - 693B_0' + 1573)f^3 \\ &+ (27H - 108B_0' + 105)f^2 + 6(3B_0' - 5)f + 6\}, \end{aligned} \tag{3.3}$$

where $H = B_0B_0'' + {B_0'}^2$ and f is the finite Eulerian strain in terms of a reference volume V_r, in our case the zero pressure volume.

$$f = \frac{1}{2}\left[\left(\frac{V_r}{V}\right)^{2/3} - 1\right]. \tag{3.4}$$

3.4.2 Bader charge analysis code

An intuitive way developed by Bader [2] to divide the molecules into atoms which is based on the zero flux surface of the gradient of the electron density. As within the molecular systems, atoms can be separated in crystalline solids, and the electron population enclosed in these basins are calculated to evaluate the charge for each atom.

We used the Henkelman group code [119] which is based on the Bader partitioning method [2] for doing a topological analysis of the electron density for all the optimized structures of $Cs_2UO_2Cl_4$ crystal at each pressure in the range of $0 - 50$ GPa to compute atomic volumes and charges. The program can read in the charge densities output of `VASP` code (`CHGCAR`). This charge densities are included in two separate outputs of `VASP`: the core charge and the valence charge which are written

to **AECCAR0** and **AECCAR2**, respectively. Then, the total charge can be obtained by summing these two charge densities files using the **chgsum.pl** script using the command:

```
chgsum.pl AECCAR0 AECCAR2
```

The total charge is written to **CHGCAR_sum** which in used directly in the Bader charge analysis through the command

```
bader CHGCAR -ref CHGCAR_sum
```

Several output files are generated by the program. The atomic volume and the charge are written to **ACF.dat**. These data was used in 1D representations or even in for a further calculations. This analysis was carried out for all the optimized structures of $Cs_2UO_2Cl_4$ crystal at each pressure. For further details about the output files of the Henkelman group code, we refer to the author's website [49].

3.4.3 CRITIC2 code

CRITIC2 [91] is a program for the topological analysis of real space scalar fields of solids. It can be used in searching for critical points and basin integration using the Bader's theory. In this thesis, we used CRITIC2 to study the bond critical points and electron density at the critical points for the output of VASP calculations of $Cs_2UO_2Cl_4$ crystal at each pressure. More information can be found on the program web page [17].

Part III

Electronic Structure Calculations

4 CHEMICAL BONDING IN $Cs_2UO_2Cl_4$ COMPLEX UNDER PRESSURE

CONTENTS

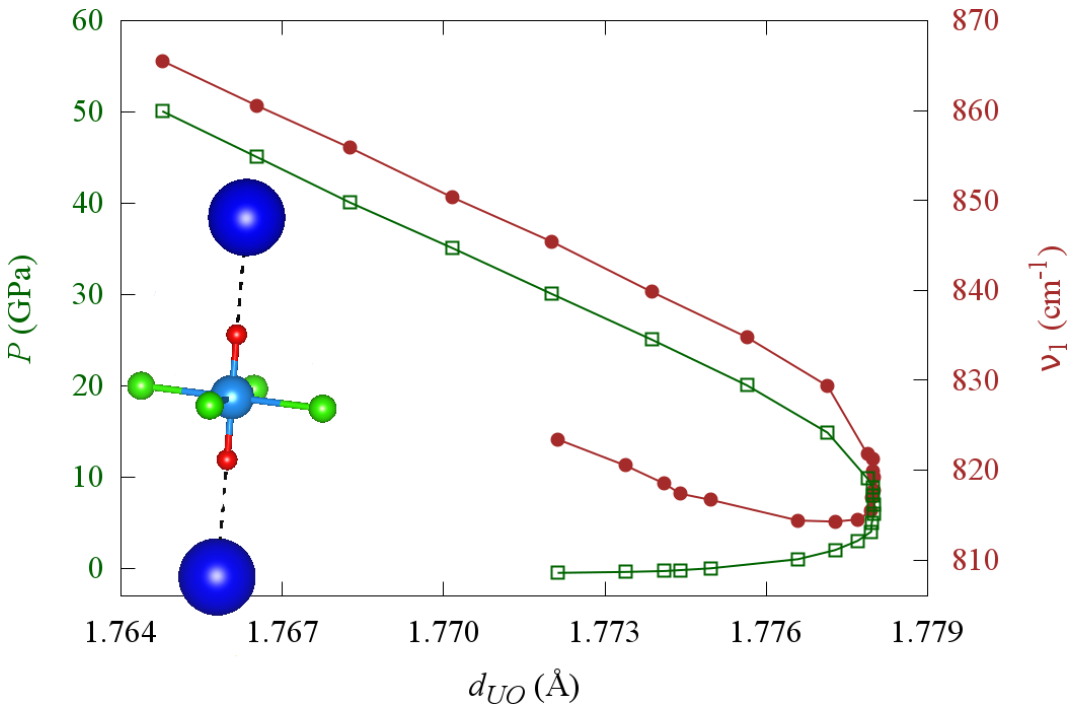

Anomalous behavior of the U–O bond under low pressure range up to 10 GPa. Increasing symmetric stretching frequencies for same bond length at pressure range 10 – 15 GPa. Model of $Cs_2UO_2Cl_4$ (U = cyan, O = red, Cl = green, Cs = blue).

An extensive investigation of pressure effects on the structural properties of crystalline cesium uranyl chloride was performed by means of first-principles calculations within the density functional theory framework. Total energies, equilibrium geometries and vibrational frequencies were computed at selected pressures up to 50 GPa. Zero pressure results present good agreement with available experimental and theoretical data. Our calculated equation of state parameters reveal that $Cs_2UO_2Cl_4$ is a high compressible material, similar to other ionic compounds with cesium cations, and displays a structural anisotropic behavior guided by the uranyl moiety. An unexpected variation of the U–O bond length, d_{UO}, is detected as pressure is applied. It leads to a d_{UO}-stretching frequency relationship that can not be described by the traditional Badger's rule. Interestingly enough, it can be explained in terms of a change in the main factor controlling d_{UO}. At low pressure, the charge transferred to the uranyl cation induces an increasing of the bond length and a red shift of the stretching frequencies, whereas it is the mechanical effect of the applied pressure above 10 GPa the dominant factor that leads to a shortening of d_{UO} and a blue shift of the stretching frequencies.

4.1 INTRODUCTION

Uranium-based compounds are important in the treatment of nuclear waste or as effective fuel materials especially for the light water reactors. Uranyl complexes attracts experimental and theoretical attention due to the decisive role they play in the migration mechanisms of this radioactive element through the groundwater and soil [18]. In the last years, uranyl chloro complexes have been particularly studied using quantum-mechanical simulations and diverse spectroscopic techniques [18, 58, 80, 112, 113, 120, 137, 138]. The nature of the chemical bonding in $Cs_2UO_2Cl_4$ was deeply studied by Zhurov *et al.* [137, 138] using experimental X-ray diffraction electron densities. Vallet *et al.* [120] carried out a rigorous analysis of quantum mechanical calculations of uranyl complexes in gas phase and in a water solvent with different Lewis base ligands, providing interesting correlations between stretching frequencies, uranyl charges, and U–O bond lengths.

X-ray diffraction and infrared and Raman spectroscopies have also been used to investigate how stretching frequencies correlate with U–O bond lengths in a variety of uranyl chloro complexes with emphasis in the evaluation of stretching force constant (k_1) and interaction force constant (k_{12}) involved in the UO_2 moiety [3, 112, 113, 120]. In the experimental work of Schnaars and Wilson [112, 113], it was observed that Badger's rule [3] fails in actinyl complexes since a shorter distance is not always accompanied by a higher stretching force constant. Failure of Badger's rule was firstly detected by Vallet *et al.* in uranyl complexes with hydroxide ligands [120]. It is to be concluded that "a great deal of caution must be afforded ... when making inferences in regard to bond distances and bond strengths" from vibrational frequencies of uranyl-based compounds [112, 113].

Pressure is an interesting thermodynamic variable if we look for structure-property correlations (see for example Ref. [102]). By applying pressure, we can significantly modify the interatomic distances and the local environment of the uranyl moiety in $Cs_2UO_2Cl_4$, in a similar way as in previous studies with different ligands and coun-

teractions [58, 80, 112, 113, 115, 120]. In spite of the strong nature of the U–O multiple bond, small but meaningful variations of its bond length could be observed under the pressure conditions attained in diamond anvil cell experiments. Quantum-mechanical simulations constitute an attractive alternative to recreate these conditions and provide valuable information on how structural changes affect force constants, charge transfer, and stretching frequencies of the uranyl moiety. However, in the case of solid $Cs_2UO_2Cl_4$, we are not aware of any previous theoretical or experimental investigation on its behavior under hydrostatic pressure.

To fulfill our purpose, first-principles electronic structure calculations were performed to optimize all the structural degrees of freedom of the monoclinic unit cell of $Cs_2UO_2Cl_4$ at selected pressures in the $0 - 50$ GPa range. We have a long-term experience in quantum-mechanical simulations of the behavior of materials under high-pressure conditions, from the determination of isothermal equations of state in simple binary compounds [75, 103] to the detailed description of phase transition mechanisms [107] and the structural prediction of novel materials [77]. In addition, two main factors were analyzed to rationalize the values of the symmetric stretching frequency of the uranyl moiety: charge and U–O bond length. In our previous work on the vibrational modes in uranyl aquo complexes, we have seen that all the frequencies, except the stretching modes associated with the U–O bond, have values below $400\ cm^{-1}$ [58]. It has been repeatedly reported that depending on the medium and equatorial ligand type, the frequencies of the stretching modes can oscillate between $800 - 900 cm^{-1}$ [58, 112, 113, 115, 120]. As our interest is in the U–O chemical bond, we will focus on the variation of the stretching frequencies with respect to pressure, and how force constants, Bader charges, and bond lengths correlate with the observed trend.

4.2 CRYSTAL STRUCTURE

The experimental crystal structure for $Cs_2UO_2Cl_4$ complex has been previously reported [128, 137, 138]. $Cs_2UO_2Cl_4$ has a monoclinic structure, space group $C2/m$, with $Z = 2$. There are four independent atoms, one of each type, with seven free coordinates and four parameters defining the volume and shape of the crystal for a total of eleven degrees of freedom. The structure can be described as formed by $[UO_2Cl_4]^{2-}$ complex anions and Cs^+ cations. The complex anion consists of six ligands bound to the metal center in a pseudo-octahedral geometry. The axial positions are occupied by the two oxo ligands, while the four chloride ligands reside in the equatorial plane (See Fig. 4.1 and 4.2). The complex anion has a D_{4h} symmetry in aqueous solution. In a crystal, the uranium atom resides on a special position with C_{2h} site symmetry, C_2 axis goes along *b* direction and σ_h plane is parallel to the *ac* plane, resulting in a strictly linear conformation of the uranyl moiety and the four chlorine atoms located in the same plane. Deviations from the higher symmetry are small. The experimental angle between chlorine plane and uranyl is $89.4°$ and between Cl–U bonds is $87.2°$. All the U–O bonds are parallel to each other, perpendicular to *b*-axis and point approximately in the [201] direction forming an angle of $49.5°$ with the *a*-axis that is very close to a half the β monoclinic angle.

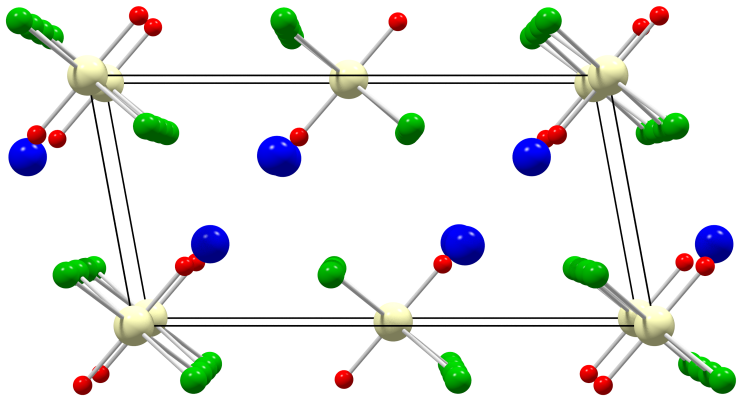

Figure 4.1: *b*-axis projection of the unit cell of $Cs_2UO_2Cl_4$ (U = yellow, O = red, Cl = green, Cs = blue).

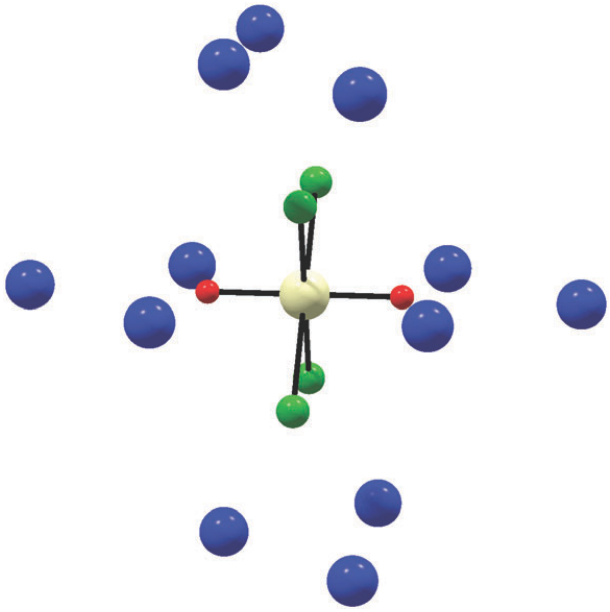

Figure 4.2: Complex anion environment in $Cs_2UO_2Cl_4$.

The crystal packing can be described as a very distorted hexagonal close-packed structure where one third of sites are occupied by the complex anion and two thirds are occupied by cesium cations. In Figure 4.1, it is seen the stacking of successive layers of anions and cations parallel to the [1 1 0] plane. Also, hexagonal layers of mixed anions and cations are formed parallel to the [$\bar{2}$01] plane. These layers contain also the uranyl bond. Each anion is surrounded by six cations in the plane and six additional ones in contiguous layers leading to a total twelve coordination. The computational details concerning the electronic structure calculations in this system were described in section 3.1.1.

4.3 RESULTS AND DISCUSSION

4.3.1 Crystal structure and equation of state

The equilibrium volume, lattice parameters (*a*, *b*, *c*, and β) and selected bond lengths and angles obtained with several approximations at zero pressure are summarized in Table 4.1. In this table, the results under LDA+*U* and GGA+*U* were obtained choosing a value of U_{eff} = 3.49 eV, which is lower than values used in previous works on UO_2 [64, 101, 114]. When compared with the experimental values [138] of *a*, *b*, *c*, and the monoclinic angle β, (11.788, 7.641, 5.769 Å, and 100.44°, respectively), our GGA (PBEsol)+*U* [98] results show a very good agreement. It is also the best level of calculation if we look at the U–O bond length (d_{UO} = 1.775 Å calculated and 1.774 Å experimental value from Zhurov *et al.* [138]), which is a key parameter in our discussion of the next section. Other interatomic distances and angles agrees very well with the corresponding experimental data, thus keeping the whole point group symmetry around the uranyl moiety. Although other levels of calculation also show a consistent description of the $Cs_2UO_2Cl_4$ structure, our results will refer only to this PBEsol+*U* level of calculation.

The overall effect of pressure on the volume and unit cell parameters can be seen in Figure 4.3. The unit cell volume of $Cs_2UO_2Cl_4$ exhibits a high compressible trend with a reduction of about 50% in the $0 - 50$ GPa range. EOS parameters, B_0 = 16.5 GPa and B_0' = 4.9, characterize a molecular-ionic class of compound with a high incompressible UO_2 dication in a quite open structure with empty space (low electron density) among cations and anions. It is noticeable that our calculated B_0 value lies in the range of other binary cesium halides. For example, the zero pressure bulk modulus in CsCl is 16.7 GPa [132].

Lattice parameters *a* and *c* decrease by about 15% in the $0 - 50$ GPa pressure range, while *b* changes to a greater extent, by about 25% of reduction, the zero pressure value. Thus, the easy axis to compress in $Cs_2UO_2Cl_4$ is the *b*-axis, which is perpendicular to the uranyl bond. Also, we obtained an increase in the value of the monoclinic angle (β) of 8%, that can be ultimately related with the orientation of the uranyl moiety in the unit cell. Overall, the calculated response of $Cs_2UO_2Cl_4$ under hydrostatic pressure shows that the structural anisotropy of this material is quite significant.

4.3.2 Internal complex geometry under pressure

Pressure affects the local geometry by changing interatomic distances and bond angles. The main bond lengths, d_{UO}, d_{UCl}, and d_{CsO} are examined in Fig. 4.4. As expected, globally the distances decrease as hydrostatic pressure is applied. In the whole $0 - 50$ GPa pressure range, the U–O, U–Cl, and Cs–O distances reduced by 0.010, 0.188 and 0.953 Å, respectively. The variations of d_{UO} induced by different environments in previous works are of the same order: 0.010 Å[112], 0.012 Å[113], 0.013 Å[115], and 0.020 Å[58]. However, rather surprisingly, d_{UO} increases by 0.006 Å in the low pressure regime (up to approximately 10 GPa).

An examination of the electron density at the bond critical points (bcp's) shows values of 0.063 for U–Cl, 0.316 for U–O, and 0.0078 e/bohr^3 for O–Cs at zero pres-

Table 4.1: Comparison between zero pressure calculated and experimental data (Ref. [138]) of lattice parameters (Å), volume (Å^3), shortest bond U–O (d_{UO}), U–Cl (d_{UCl}), and Cs–O (d_{CsO}) distances (Å) and Cl-U-O (ω_1) and Cl-U-Cl (ω_2) bond angles (°).

	a	b	c	β	V	d_{UO}	d_{UCl}	d_{CsO}	ω_1	ω_2
LDA	11.56	7.33	5.70	102.0	472.4	1.803	2.618	3.02	90.6	92.4
LDA+U	11.52	7.47	5.66	101.5	476.8	1.770	2.653	3.09	90.6	93.0
PBE	12.26	7.84	5.98	100.9	565.0	1.815	2.678	3.35	90.8	93.1
PBE+U	12.36	7.89	5.95	96.8	576.5	1.780	2.717	3.74	90.9	92.9
PBEsol	11.88	7.57	5.83	101.5	513.7	1.808	2.641	3.18	90.7	92.9
PBEsol+U	11.88	7.68	5.79	100.0	520.8	1.775	2.678	3.32	90.7	93.3
Exp.	11.79	7.64	5.77	100.4	511.01	1.774	2.671	3.32	90.3	92.9

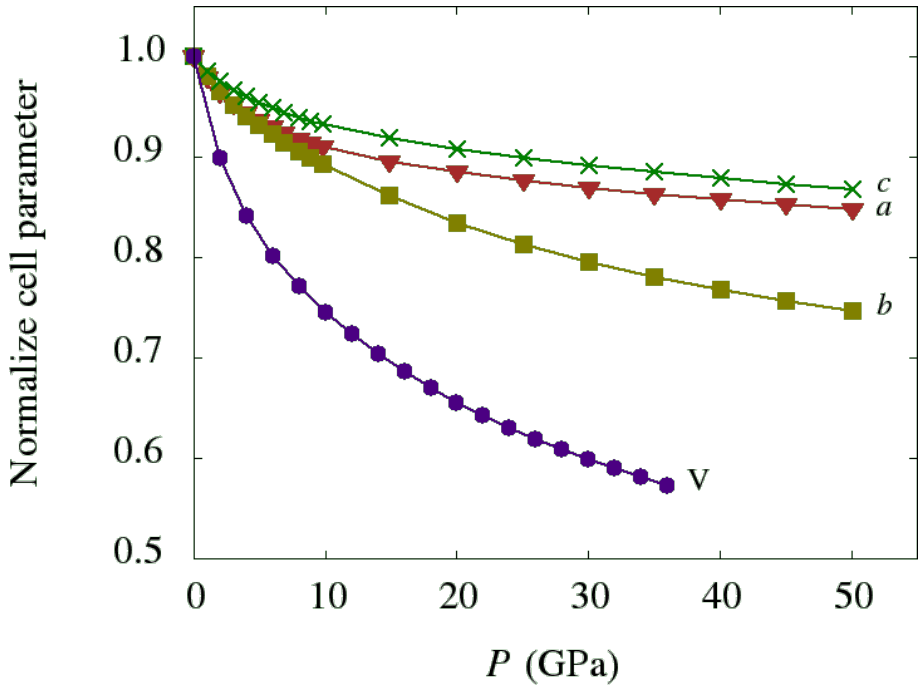

Figure 4.3: Normalized cell parameters and unit cell volume of $Cs_2UO_2Cl_4$ with respect to hydrostatic pressure according to our calculations.

sure. These results are in accordance with experimental data [138] and cluster calculations [120]. When pressure increases, both U–Cl and O–Cs electron densities at the bcp increase monotonously. However, in the case of U–O, the electron density at its bcp decreases to a minimum value of 0.312 e/bohr^3 at 10 GPa and then shows the increasing trend as pressure increases up to 50 GPa (See Fig. 4.5). Moreover, these results are consistent with the behavior displayed by our bond length data in Fig. 4.4. These facts are fully consistent with a weakening of the U–O bond manifested by frequency parameters in the low pressure regime, as we will see below.

To explain this fact, we have to go further into the behavior of other distances and the effect of electrostatic interactions. We have observed that 77% of the total shortening of Cs–O bond length occurs in the $0-10$ GPa region, where d_{CsO} decreases by 0.481 Å. Similar behavior is obtained for the U–Cl distance, about half the change takes place up to 10 GPa with a reduction of 0.082 Å. As discussed by Vallet *et al.* [120], a drop in the ligand-U distance correlates with a lengthening of the U–O distance due to the electrostatic repulsions between the yl-oxygens and the negatively charged chloride ligands. Moreover, as we will discuss in detail later, it should be also emphasized that as pressure is applied the charge transferred to the uranyl moiety increases. This effect tends to enlarge the U–O and can be only compensated at high enough pressures by the effect of other atoms approaching the oxygen atom.

The rest of the internal coordinates were optimized for each point of the grid. In order to test this hypothesis we have made electronic structure calculations in a model system comprising an *in vacuo* UO_2Cl_4 cluster with two Cs atoms located in the line O–U–O above and below the chlorines plane. The cluster calculations were performed using the `Gaussian09` code [35] with two functionals, B3LYP (hybrid) [6,

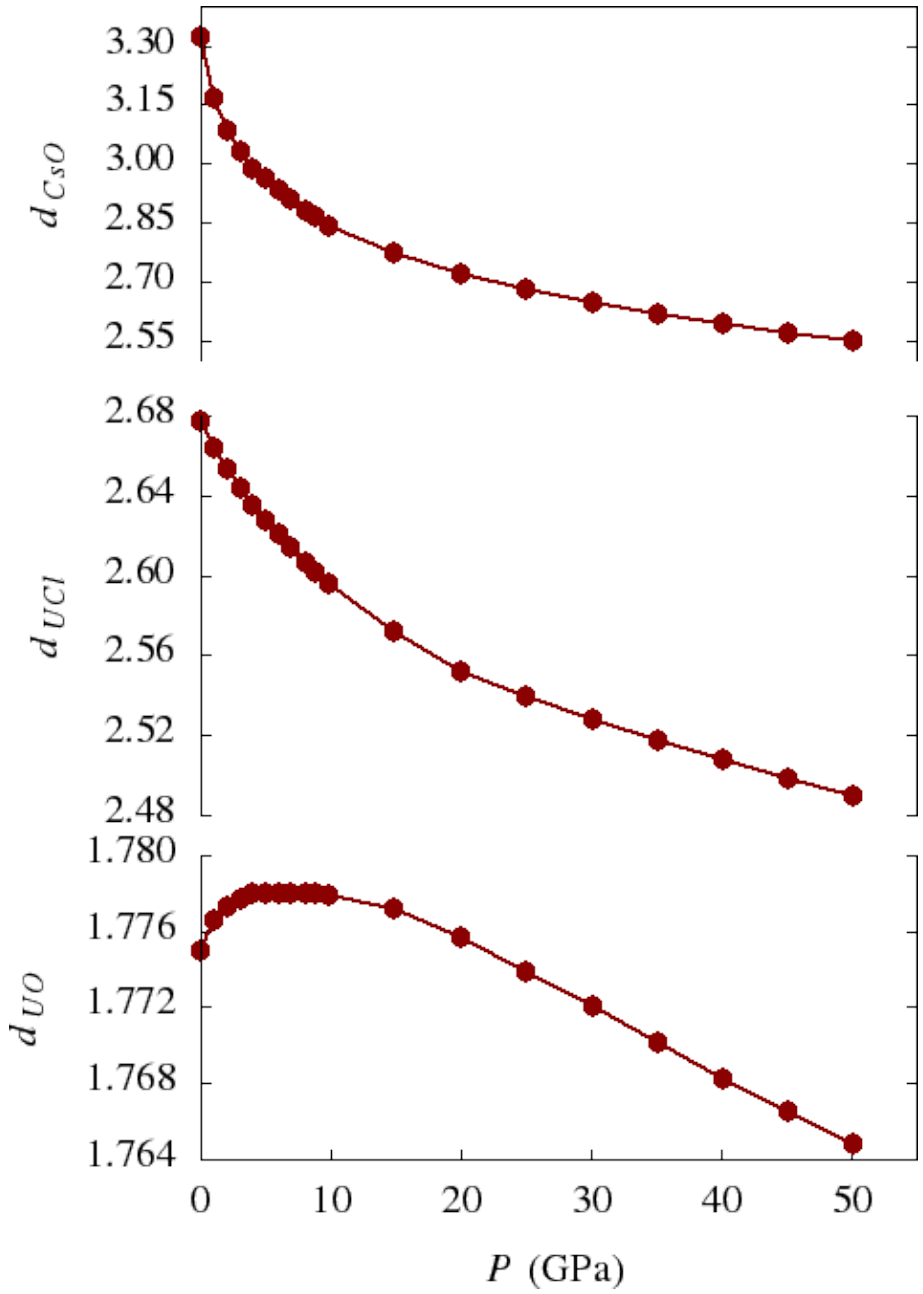

Figure 4.4: Relevant bond lengths (Å) in $Cs_2UO_2Cl_4$ with respect to hydrostatic pressure.

72] and PBE (GGA) [97], Dunning augmented double-z basis were used for Cs, O and Cl atoms. For U atoms a 60 electron pseudopotential was used in combination with a double-z basis.For a fixed U–Cs distance, decreasing U–Cl distance in the range from 2.4 to 2.8 Å in steps of 0.01 Å leads to longer U–O bond as expected as shown in Fig. 4.6. For a fixed U–Cl distance, decreasing U–Cs distance in the range from 4.0 to 5.5 Å in steps of 0.02 Å also lead first to a longer U–O bond (electrostatic attractive effect) but at certain distance the behavior is reversed (Pauli repulsion). The obtained curve in Fig. 4.7 shows the same qualitative behavior as the one seen in Fig. 4.4 for d_{UO} with respect to pressure in the crystal. This supports

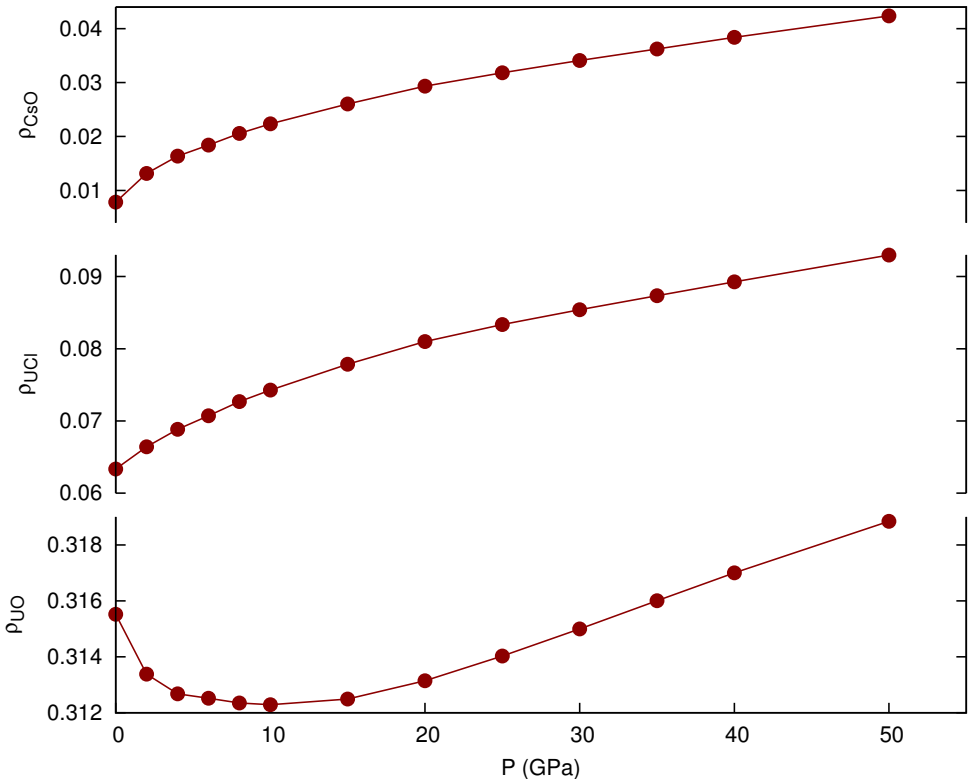

Figure 4.5: Electron density e/bohr^3 at the critical bond points at several pressures.

our hypothesis of competing factors determining the final U–O bond distance in the crystal.

The angle between the U–Cl and U–O bonds (ω_2 or ω_3) is negligibly affected by pressure, thus remaining close to 90° in the $0-50$ GPa range. On the other hand, the two supplementary Cl–U–Cl angles in the equatorial plane (ω_1 and ω_4) change by about 21° over the whole pressure range as shown in Fig. 4.8. It is energetically preferable to change the equatorial angle maintaining the uranyl bond perpendicular to it. When the pressure increases and the cell is compressed, the repulsion forces between chloride atoms can be minimized increasing one Cl–U–Cl angle and decreasing the other one making the *b*-axis the preferred compression direction. It is remarkable that close to 10 GPa all $\omega_i - p$ curves cross with a value of 90°.

4.3.3 Badger's rule and vibrational frequency under pressure

The local distortions induced by pressure lead to changes in the U–O bond strength that can be quantified evaluating parameters associated to the symmetric and antisymmetric stretching modes of the uranyl moiety. Frequencies were calculated using the finite displacement method with a step of 0.008 Å and four displacements at all the optimized equilibrium geometries. Typical values of ν_1 and ν_3 in the UO_2Cl_4 complex anion lie within the $831-842$ cm^{-1} and $900-922$ cm^{-1} ranges, respectively [112, 113]. Our calculated crystalline vibrational frequencies of the symmetric and antisymmetric modes at zero pressure are 818 cm^{-1} (832 cm^{-1}) and 979

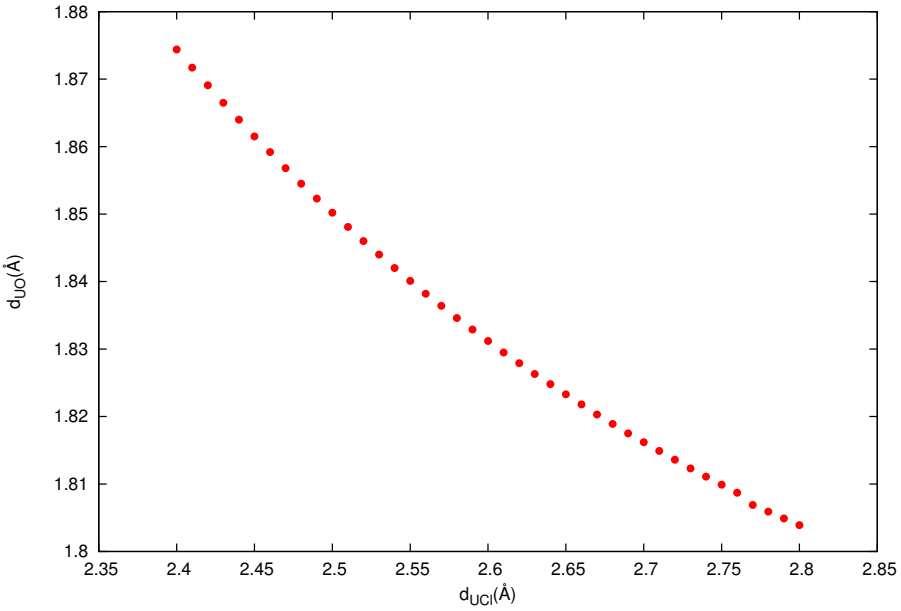

Figure 4.6: U–O vs U–Cl distances obtained in the cluster calculations (U–Cs fixed at 5.1 Å).

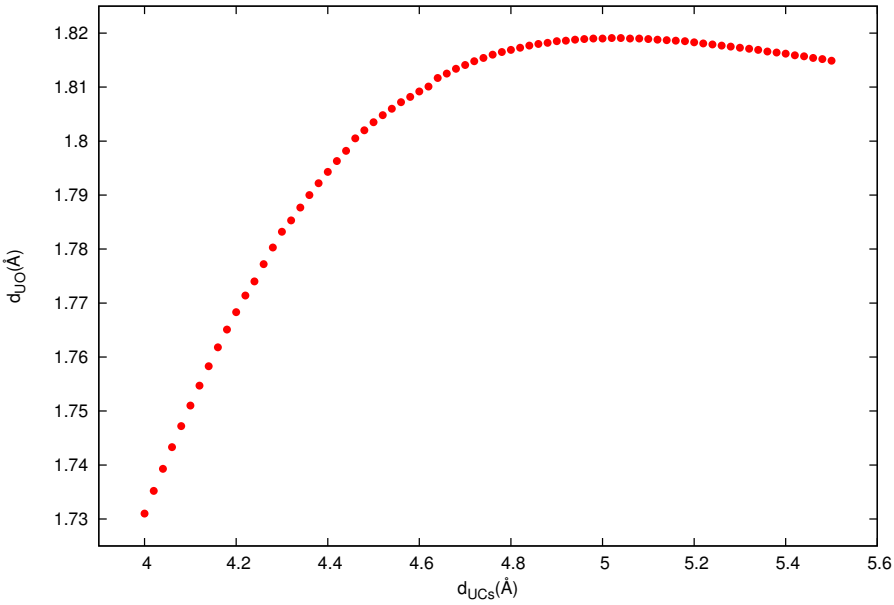

Figure 4.7: U–O vs U–Cs distances obtained in the cluster calculations (U–Cl fixed at 2.68 Å).

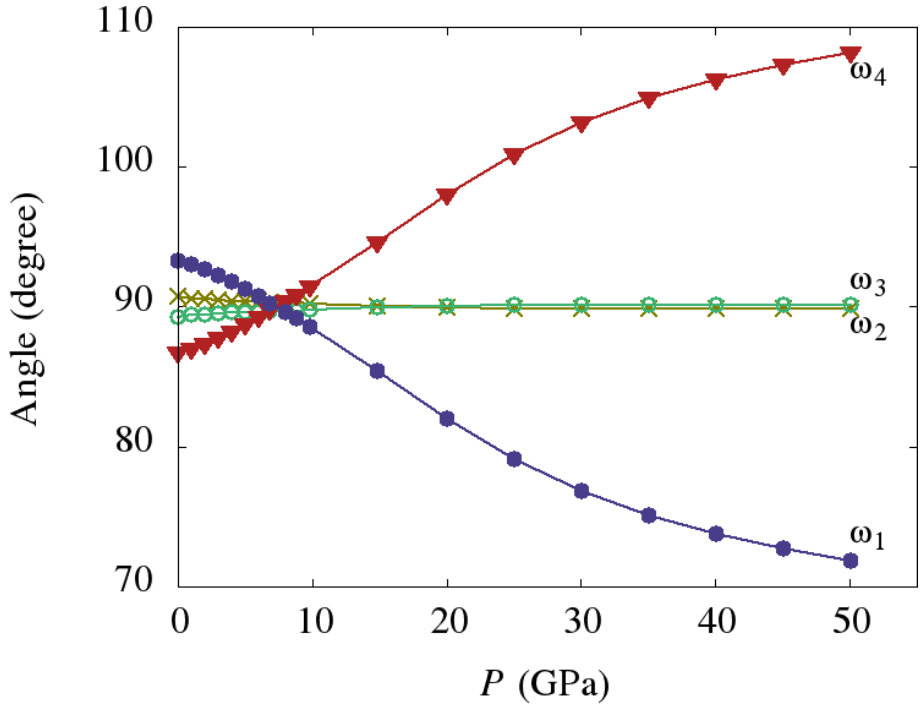

Figure 4.8: Main bond angles of the UO_2Cl_4 complex anion in the $Cs_2UO_2Cl_4$ crystal with respect to hydrostatic pressure. See text for definition of ω_i symbols.

cm^{-1} (922 cm^{-1}). Deviations with respect to experimental values [112] (in brackets) are lower than 2% and 7%, respectively.

Overall, the pressure evolution of these frequencies shows a typical slightly sub-linear trend being the splitting between ν_1 and ν_3 almost constant along the pressure range of our study. When we plot the stretching frequencies against d_{UO} (See Fig. 4.9), we have found two branches-like behavior for both frequencies. In each branch the expected relationship between shorter bond and increased frequency is found. We have noticed that the jump from one branch to the other occurs at the d_{UO} value obtained around 8 GPa. This result is a manifestation of the d_{UO}-p behavior previously discussed (See Fig. 4.4-bottom).

We have calculated the stretching force constant, k_1, and the interaction force constant, k_{12}, from the computed frequencies [112] (See Fig. 4.10). k_1 is a measure of the strength of the U–O bond, whereas k_{12} describes the interaction between the two yl-oxygen atoms. The actual expressions relating k_1 and k_{12} with ν_1 and ν_3 can be found elsewhere (See for example eq. (3) and (4) of Ref. [4] or the supplementary material of Ref. [112]). Here, it is important to point out that besides the mass dependences, k_1 and k_{12} roughly depend respectively on the sum and difference of these frequencies. Our calculated values fall in the range of $7.06 - 7.95$ for k_1 and -0.804–-0.900 for k_{12} over the selected pressure range. The values of Schnaars and Wilson in a variety of UO_2-based compounds [112, 113] span across 6.58 to 6.82 and -0.18 to -0.27 for k_1 and k_{12}, respectively.

In plutonyl complex anions, the interaction force constant shows values as low as -0.53 [112]. With respect to our calculated values, the difference in k_{12} is easily explained in terms of the higher computed value of ν_3 and the sensitivity of the model to the input frequencies. Besides, it is to be pointed out that our negative

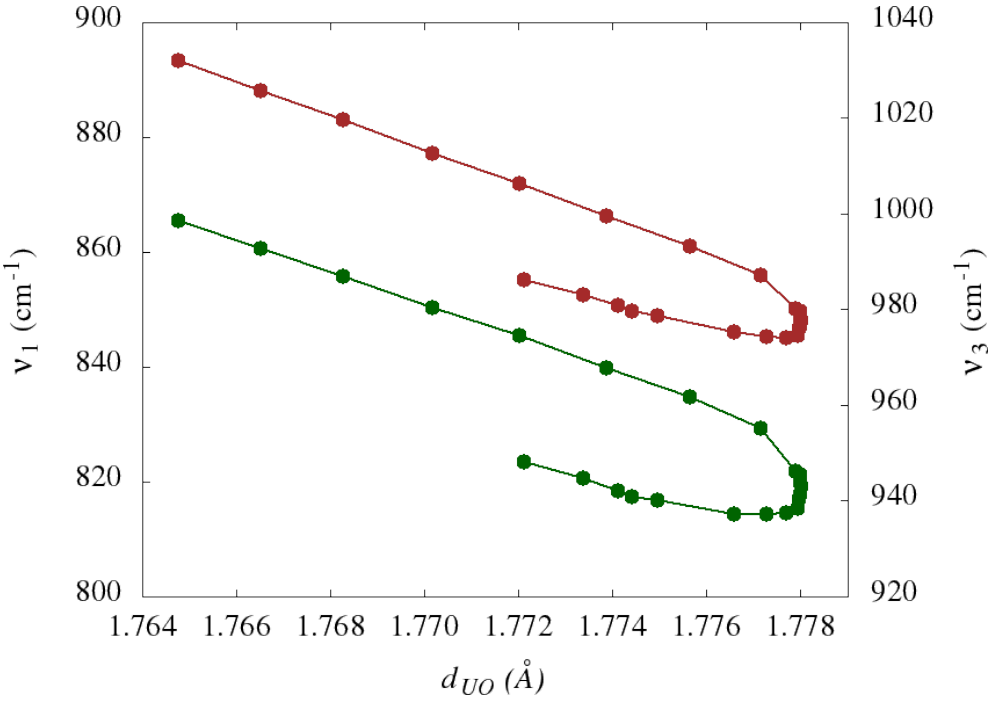

Figure 4.9: Frequencies of the symmetric (lower curve, left axis) and antisymmetric (upper curve, right axis) stretching modes of uranyl with respect to d_{UO}.

k_{12} values are consistent with the inverse trans influence experienced by dioxo actinyl compounds that generates negative (ν_1-ν_3) differences. Although k_{12} has a relatively small change in the computed pressure range, it exhibits a maximum in a zone close to the jump in the frequencies branches discussed above.

A formal relationship between d_{UO} and k_1 can be described with the Badger's rule [3], expressed here as

$$k_1^{-1/3} = A^{-1/3}(d_{UO} - B), \tag{4.1}$$

where A and B are the fitting parameters. This rule implicitly contains the more general rule that a shorter bond has a larger stretching force constant. Derived relationships were used by Bartlett and Cooney to predict U–O bond lengths from stretching frequencies with varying success [4]. We have observed that our data can not be described by a unique Badger's relationship (see top and bottom straight lines in Fig. 4.10-right). Interestingly enough, we see, however, that these two Badger linear trends describe accurately the correlation between d_{UO} and k_1. From our fittings, we obtained 0.65 and 1.00 mdyn Å^2, to be compared with the universal Badger parameter (A = 1.86 mdyn Å^2) [85, 129]. Thus, our data does corroborate previous results on studies of dioxo actinyl compounds regarding Badger's rule failure [112, 113, 120].

Nevertheless, it is possible to explain this anomalous behavior of Badger's rule by means of a deeper analysis of the two main factors affecting frequencies and distances as pressure is applied. The first factor is the pure mechanical effect that produces an overall shortening of interatomic distances in the crystal. The second one acts in the opposite direction as far as the d_{UO} distance is concerned. It is

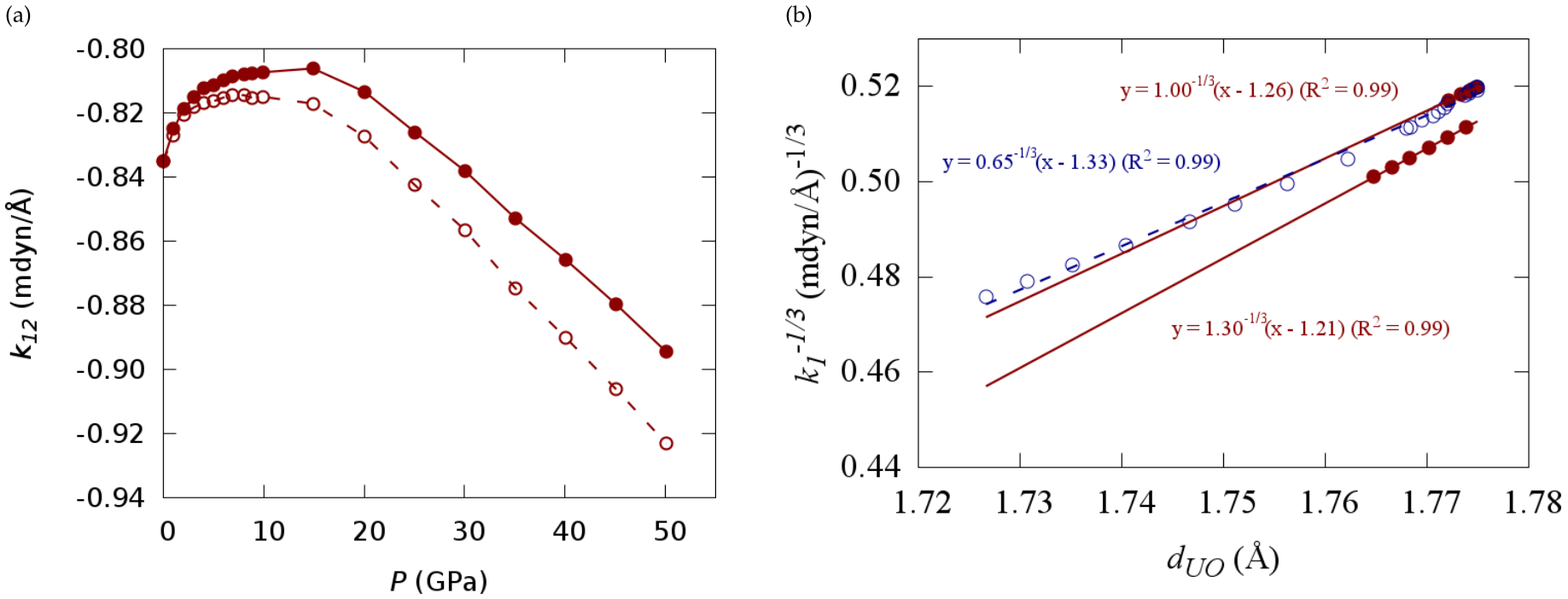

Figure 4.10: Interaction O_{yl}-O_{yl} constant with respect to (a) hydrostatic pressure and (b) force constant-bond length linear correlations in the U-O chemical bond. Results from the pure mechanical model are displayed in dashed lines and empty circles.

Table 4.2: Atomic charges (q, e) and atomic volumes (Ω, Å^3) for $Cs_2UO_2Cl_4$ crystal.

	U	O	Cl	Cs	UO_2	
q	2.756	-0.878	-0.685	0.871	1.000	Present
	2.751	-0.923	-0.605	0.774	0.905	Exp. [138]
Ω	17.04	19.13	32.64	37.26	55.30	Present
	16.17	18.99	31.39	37.73	54.15	Exp. [138]

the charge transferred to the UO_2 moiety. The idea is to separate both factors and evaluate the fulfillment of Badger's rule without considering charge transfer effects. Before this analysis is introduced, we recall to previous results on the charge transfer in uranyl hydrated species [115] along with our own results at this regard.

4.3.4 Charge transfer to uranyl ion under pressure

As formerly illustrated by Siboulet *et al.* [115], the charge transferred to the uranyl dication is a good parameter to explain changes in the U–O bond length and stretching frequencies involved in the uranyl moiety. At zero pressure, our topological analysis of the electron density leads to a total charge of the $Cs_2UO_2Cl_4$ unit cell of 0.0001 e, and a unit cell volume calculated from separate atomic volumes of 520.75 Å^3. These values are consistent with the neutral character of the cell and with the optimized cell volume. Our calculated charges and volumes are close to those obtained from the topological analysis carried out by Zhurov *et al.* using experimental charge densities of the same crystal at 20 K (See Table 4.2). This experimental study gives a total charge of uranyl of $+0.905$ e, while we obtain a value of 1.00 e. For this moiety we previously obtained a value of 0.996 e for the same complex in water solution [58].

4.3.5 Charge and frequency versus pressure

The effect of pressure on the charge transferred to uranyl, calculated as the difference between the uranyl formal charge (+2) and the calculated one, is presented in Fig. 4.11. The uranyl charge decreases as the pressure increases. The charge transferred to uranyl increases by 25% of its zero pressure value when pressure increases up to 50 GPa.

Let us propose now an analysis of Badger's rule using k_1-d_{UO} data coming from results involving only the pure mechanical effects on frequencies and distances. A simple yet reasonable procedure consists of removing the reduction in frequencies and the increasing in distances induced by the charge transferred to the uranyl moiety. At a given pressure, $\nu_1(p)$ and $d_{UO}(p)$ can be described with these expressions:

$$\begin{aligned} \nu_s(p) &= \nu_1(0) + \Delta\nu_1(p); \quad \Delta\nu_1(p) = \Delta\nu_1^M(p) + \Delta\nu_1^{CT}(p), \\ d_{UO}(p) &= d_{UO}(0) + \Delta d_{UO}(p); \quad \Delta d_{UO}(p) = \Delta d_{UO}^M(p) + \Delta d_{UO}^{CT}(p), \end{aligned} \tag{4.2}$$

where the superscripts M and CT stand respectively for the contributions due to pure mechanical and charge transfer effects. We can use the proposed slopes

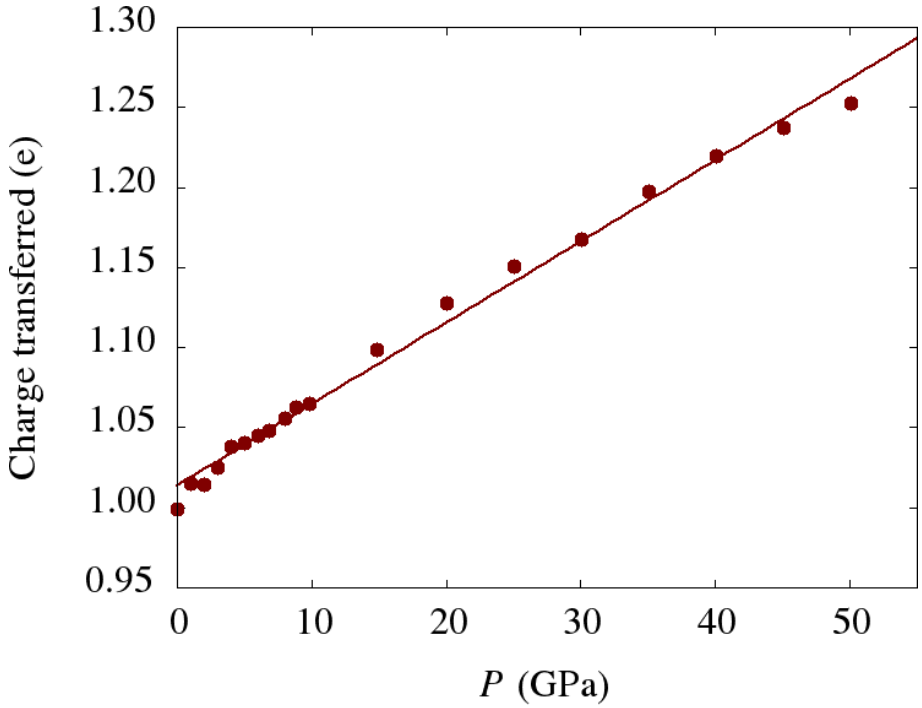

Figure 4.11: Bader charge transferred versus pressure. R^2 = 0.996 and the slope corresponds to 0.005 GPa per electron transferred.

reported by Siboulet *et al.* [115] for the charge transfer effect in the frequency, -300 cm^{-1}, and the distance, +0.16 Å, both per electron transferred to the uranyl moiety. Taking the charge transferred at zero pressure as the reference value, we can obtain the contributions to the frequencies and distances at different pressures using the above slopes and the calculated relationship between pressure and charge transferred displayed in Fig. 4.11. With this information we can evaluate new frequencies and distances only affected by the pure mechanical effect using the following expressions:

$$\nu_1^M(p) = \nu_1(0) + \Delta\nu_1^M(p); \quad d_{UO}^M(p) = d_{UO}(0) + \Delta d_{UO}^M(p) \tag{4.3}$$

Similar equations can be written for ν_3 providing the basic data, along with d_{UO}^M values, for a new analysis of Badger's rule. Results are included in Fig. 4.10, and illustrate how the fulfillment of this rule is achieved. Successfully, a single straight line can now describes the correlation between the force constant and the bond length (See Fig. 4.10-right). From this fittings, we have obtained for the Badger parameter A = 1.30 mdyn $Å^2$.

We have also considered the behavior of uranyl charge and the symmetric stretching Raman frequency versus the U–O distance as shown in Fig. 4.12. The frequency-distance relationship shows three different regimes: (i) the symmetric stretches ν_s decreases around 4 cm^{-1} at low pressures up to 5 GPa, (ii) from 5 to 10 GPa the blue shift is around 8 cm^{-1}, and (iii) an increase around 40 cm^{-1} is observed in the high pressure range from 10 to 50 GPa. At both low and high pressure ranges, the shorter the bond length the larger the Raman frequency. However, at 8 GPa (d_{UO} = 1.778 Å), the blue shift, of about 8 cm^{-1} in ν_s, appears without bond length

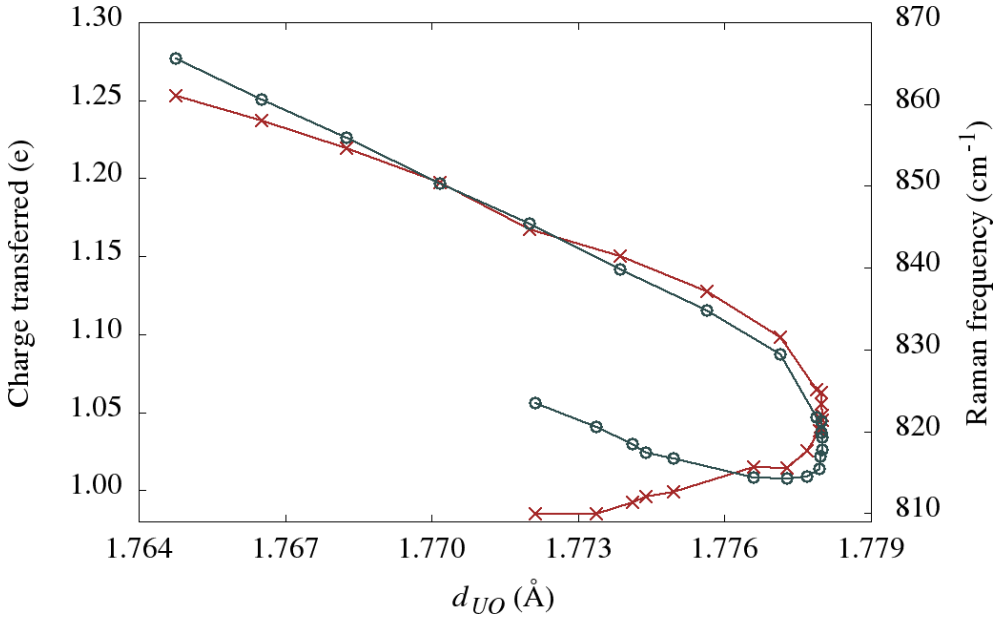

Figure 4.12: Bader charge transferred (cross, left axis) and Raman frequency (circle, right axis) versus uranyl bond length.

variation. A linear correlation between the U–O distance and the Raman-active vibrational frequency with a slope of 20 cm^{-1}/pm was proposed by Siboulet *et al.* [115] when different aquo uranyl complexes were considered. A similar behavior can be derived from our calculations in crystalline $Cs_2UO_2Cl_4$ but in two different pressure regions.

In the low pressure regime the decrease in the Raman frequency (and the accompanied increase in bond length) is associated with a decrease in the uranyl charge, that is the same behavior found by Siboulet *et al.* Our $\Delta\nu_s/\Delta d_{UO}$ ratio is only around 10 cm^{-1}. The lower slope can be attributed to a greater Δd_{UO} value than expected from the charge transferred to the uranyl dication. This effect is caused by an enhancement of attractive electrostatic interactions of the Cs cations that display a very rapid reduction of their distances to the yl-oxygen atoms in the low pressure regime, as we have seen in Fig. 4.4. However, at pressures higher than 10 GPa the charge transfer is not a good parameter to correlate with distances and symmetric stretching frequencies: an increase in the Raman frequency (and the accompanying bond length decrease) occurs in spite of the increase of the charge transferred to UO_2. This is due to a pure mechanical effect of hydrostatic pressure that reduces the d_{UO} distance, strengthening the U–O bond, and leads to a blue shift in the stretching frequencies. What is more, d_{CsO} distances enter in the repulsive regime and this interaction starts pushing rather than pulling the U–O bond.

Part IV

DFT Chemical Pressure Analysis

5 CHEMICAL BONDING IN THE LIGHT OF CHEMICAL PRESSURE CONCEPT

CONTENTS

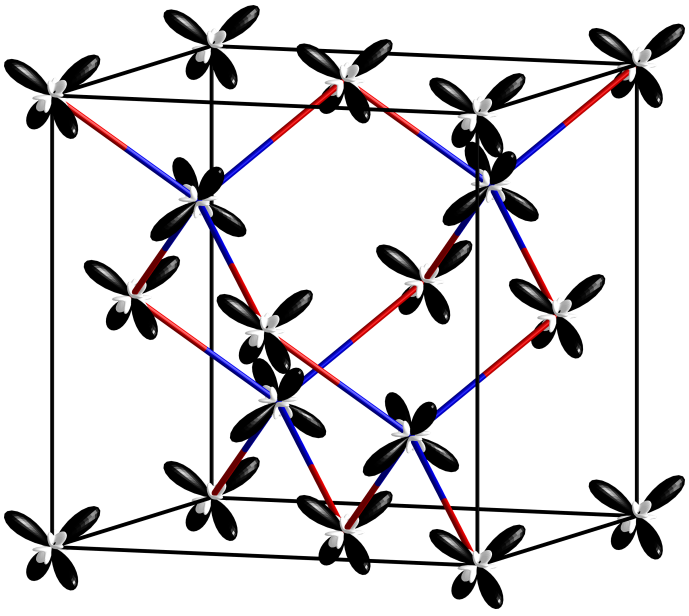

The DFT-CP associated with carbon atoms in diamond. White and black lobes represent positive and negative pressures, respectively. The anisotropy of the chemical pressure is apparent with positive pressure pointing along C–C contacts implying difficulty to compression in that direction. As expected, negative lobes point to interstitial voids within the diamond framework showing the easiest direction for volume reduction.

Traditionally, the concept of chemical pressure (CP) has been invoked to understand the new behavior of materials emerging when chemical elements are replaced by others of different size, though quantitative accounts of this effect are rarely reported. Recently, a quantum mechanical definition has been proposed to construct real space CP maps of molecules and crystals from the output of DFT calculations [33]. The characterization of bonding interactions in molecules and materials is one of the major applications of quantum mechanical calculations. Numerous schemes have been devised to identify and visualize chemical bonds, including the electron localization function, quantum theory of atoms in molecules, and natural bond orbital analysis, whereas the energetics of bond formation are generally analyzed in qualitative terms through various forms of energy partitioning schemes. In this chapter, we illustrate how this approach reveals the chemical bonds through the forces of attraction and repulsion acting between the atoms.

5.1 INTRODUCTION

Chemical bonding has long been an elusive concept from the point of view of Quantum Mechanics [86]. This is mainly due to two practical reasons: (1) it is not a perceptible property that can be experimentally observed directly (but is instead inferred from interatomic distances, bond enthalpies, and perhaps electron density maps), and (2) there is not any particular quantum- mechanical operator associated to it.

To fill this gap between chemical experience and theory, a number of approaches have been developed to analyze bonding in the results of quantum mechanical calculations. These have generally focused either on (1) identifying signatures of bonding in the wavefunctions [31, 56, 57, 79, 127, 133, 134, 139, 140], density matrices [21, 32, 36, 104, 105], electronic density [2, 62], or some derivative function [7, 69, 108–110, 116, 125], or (2) decomposing the energy of an interaction in physically meaningful terms [23, 52, 126]. In this chapter, we show that these two approaches can be merged in the recently developed chemical pressure (CP) method, yielding schemes in which bonds are evident in the balance of attractive and repulsive forces acting within a structure [33].

The foundations for an energy-map based approach to visualizing bonding has been emerging in the context of solid state chemistry, with the development of the chemical pressure (CP) formalism [33]. Through the spatial decomposition of macroscopic pressure into local, interatomic components, this CP approach leads to visual schemes that anticipate structural transformations in intermetallic compounds [65], highlight of potential soft phonon modes that drive second-order phase transitions [25], predicting structural instabilities [33, 34], and provide intuitive interpretations of the cohesion of crystalline solids [34]. Using simply the distribution of the minimized electronic energy along a grid of voxels in which the unit cell is partitioned, this methodology is able to provide the local pressure in each of these voxels just evaluating how their energy changes as the volume of the unit cell departs from the equilibrium value. From these thermodynamic-like local pressures, chemical pressure maps can be built illustrating how high and low pressures are overall associated, respectively, with electron core and valence regions, thus providing a wealth

of information on the existing and potential interactions between the atomic constituents of the solid.

The energies obtained from quantum mechanical calculations have also inspired the development of analytical tools. The total energies calculated for a compound can be partitioned in a variety of ways [23, 52, 126]. One of the most fruitful of these approaches was pioneered by Ruedenberg in the 1960s analyzing the physical origin of the chemical bond, examining how the separate kinetic and potential energy contributions lead to the cohesion between atoms in a covalent system [28, 29, 106]. In these studies, a compelling story emerged based on the classic conflict between the potential energy's drive to localize electrons around the atomic nuclei, and the kinetic energy costs of localization: the ability of electrons to delocalize over a pair of atoms in a bond lowers the kinetic energy penalty to concentrating the electrons near the nuclei. These conclusions have since been reaffirmed by other authors and increasingly accurate calculations [1, 37, 111].

So far, the CP approach has mainly been applied to explaining structural phenomena, but the maps generated are also rich in information regarding chemical bonding. In this chapter, we will see how the chemical pressure method can provide an new alternative route to visualizing chemical bonding quite distinct from previous and current extensions of chemical bonding methods based on the electronic wavefunction.

5.2 STRUCTURAL AND COMPUTATIONAL DETAILS

5.2.1 Crystal structure

Unless specified, atomic units are always used.

The electronic structure calculations were carried out following the method described in section 3.2 of chapter 3. Covalent bond has been studied in isolated molecules, H_2, CO_2 and S_8 and also two- and three-dimensional carbon units of respectively graphene and diamond. Besides, we explored the CP distributions in systems displaying covalent and weak intermolecular interaction such as van der Waals and hydrogen bonding. The former is usually found in graphite and molecular crystals of S_8 and CO_2 while the latter is exiting between water molecules (Ice-I_h). Metallic bonding has been studied in crystals of Na (*bcc*) and along group 15 elements; As, Sb, and Bi. Finally, we show the CP in the ionic crystals like NaCl. Further details, including the space groups as well as optimized cell parameters are given below in Table 5.1.

5.2.2 Computational details

Further details regarding to DFT calculations, including the cut-off energies and Monkhort-Pack k-point grids [83], are provided in Table 5.2. The semi-core (SC) potential for sodium was used in case of metallic sodium and ionic sodium chloride because the valence-only (VO) pseudopotential did not provide a simultaneously coherent picture for both crystals. The active valence space contains 9, 7, 4, 6, 6 and 1 electrons for Na, Cl, C, S, O and H, respectively, and 5 electrons for the group 15 elements As, Sb, and Bi.

Graphene calculations were performed using a graphite unit cell with a long c-axis to avoid interlayer interactions.

Table 5.1: Unit cell parameters of conventional cells, distance in Å and angle in degree (°), for DFT-optimized structures at zero pressure used in ABINIT and DFT-CP calculation. Space group (SG) are given.

	SG (no.)	a	b	c	α	β	γ
All isolated molecules	P1	10	10	10	90	90	90
C-graphene	P6_3/mmc (194)	2.4431	2.4431	21.4488	90	90	120
C-diamond	Fd − 3m (227)	3.5317	3.5317	3.5317	90	90	90
S_8	Fddd (70)	13.2462	12.7555	7.8808	75.7906	68.9872	35.2222
CO_2-I	Pa − 3 (205)	5.2863	5.2863	5.2863	90	90	90
Graphite	P6_3/mmc (194)	2.4431	2.4431	2.4431	90	90	120
Ice-I_h	P6_3cm (185)	7.1858	7.1858	6.7609	90	90	120
Na-bcc	Im − 3m (229)	4.5865	4.5865	4.5865	90	90	90
As	R − 3m (166)	3.9128	3.9128	9.5929	90	90	120
Sb	R − 3m (166)	4.4917	4.4917	11.0263	90	90	120
Bi	R − 3m (166)	4.7351	4.7351	11.6643	90	90	120
NaCl-B1	Fm − 3m (225)	5.4645	5.4645	5.4645	90	90	90

Table 5.2: Main computational parameters used in ABINIT and CP computational packages.

	E_{cutoff}	k-point grid	FFT-grid
H_2	100	1×1×1	180×180×180
CO_2	170	1×1×1	225×225×225
S_8	80	1×1×1	240×240×240
C-graphene	80	11×11×2	40×40×360
C-diamond	100	8×8×8	45×45×45
S_8	60	4×4×4	192×192×192
CO_2-I	220	6×6×6	150×150×150
C-graphite	80	11×11×4	40×40×108
H_2O-I_h	140	4×4×4	150×150× 144
Na	300	6×6×6	36×36×36
As	30	6×6×2	45×45×120
Sb	30	5×5×2	45×45×108
Bi	30	5×5×2	45×45×108
NaCl	70	6×6×6	54×54×54

5.3 RESULTS

In formalism described in chapter 2, we saw how the DFT internal pressure is amenable to being resolved onto maps. As this internal pressure contains all contributions establishing the equilibrium geometry of the structure, the bonding forces leading to the cohesion of solids and molecules should in some way be visible in these maps. Looking at the expression of the chemical pressure in Eq. 2.44, we can foresee some general answers as to how these forces should manifest in the CP maps. In regions of space where CP is negative, a reduction of the system's volume would lower the local energy. This scenario suggests that the ion cores are packed too sparsely around the electrons. This is in contrast to areas of positive CP, where increasing the system's volume is needed for a lowering in local energy. Electrons are not so comfortable in these regions, as the ion cores seem to be packed around them too densely. The electron density in regions wishing a reduction of volume is responsible for the attraction between chemical nuclei while that in the positive pressure zones acts to drive the nuclei apart. Thus, overall, we can expect low chemical pressures associated with bonds and attractive interactions, whereas positive chemical pressures would be related to core electrons and repulsive interactions.

5.3.1 H_2 molecule

To begin seeing how bonding forces are revealed by CP maps, we start with H_2, the simplest neutral molecule. This system is particularly interesting as it has no core electrons, and the electronic factors determining the interatomic distance will emerge entirely from the valence electrons. A look at the 2D slice through the CP map in Fig. 5.1 reveals that these forces are not uniformly distributed: a continuous closed region of negative pressure contains the two H nuclei, with the values being especially low (blue) close to the two nuclei along the bonding path. The positive

pressures, however, are located further outwards from the nuclei, beyond the black contour corresponding to CP=0. Overall, then, the forces leading to the cohesion between the H atoms are concentrated between that nuclei (reminiscent of the cartoon of electrons acting as glue holding the atoms together), with the drawbacks of bond formation being felt further out from the bonding region.

Several connections can be perceived between this CP map and the physics of chemical bond formation described by Ruedenberg [106]. In terms of the attractive region, note that the strongest attraction is not directly at the midpoint of the interatomic contact, but is instead concentrated near the two nuclei on opposite sides of the midpoint. This is a manifestation of the relationship between kinetic and potential energy encoded in the virial theorem: the spreading of the wavefunction across the two nuclei lowers the kinetic energy cost of tightening the wavefunction around the nuclei. A deeper potential energy is thus attained for those electrons close to either of the nuclei in the space between atoms.

A promotion state is a promolecule representation of the system built with atomic-like electronic densities consistent with the molecular solution.

The positive chemical pressure located away from the bonding region close to the nuclear positions (core), the *kinetic energy pressure* in Ruedenberg's words, can be understood in as *promotion* effect. In these outer regions, the potential is more like that of the free atoms; the deviations from the free-atom wavefunctions then, locally, are perceived as a destabilizing perturbation.

While these two opposing effects cancel each other out at the equilibrium geometry, they are distributed in very different ways. The attractive CP region is small but contains relatively large magnitudes, with the range of negative CP values being between -0.85 and 0.00 a.u. (1 a.u. = 29422 GPa). The repulsive region, on the other hand, consists essentially of the rest of space, with very small values being spread over this expansive volume, between 0.00 and 0.02 a.u.

Another way of visualizing these features, which will become useful for the more complicated structures below, is through isosurfaces, as shown in Fig. 5.1-b. Here, isosurfaces of one selected positive and one selected negative CP value, +0.006 a.u. (white) and -0.01 a.u. (black), respectively. In this image the cylindrical symmetry of the molecule is apparent, with the negative CP isosurface

enclosing a volume containing the two nuclei as expected from the 2D plot. The positive isosurface, on the other hand, highlights the concentration of positive CP at the two ends of the molecule (resembling the anti-bonding molecular orbital) and in a ring dividing the molecule into two equal parts containing one H atom each.

The way in which these positive and negative CP features control the H–H bond distance can be visualized by following the evolution of the CP isosurfaces over a range of H–H distances. This process is carried out in Fig. 5.2, with isosurfaces at $\pm$ 0.009 a.u. for distances between 0.65 and 0.85 Å.

At 0.85 Å, plot is dominated by the negative CP features, with only the slightest of dots of positive CP on the opposite sides of the molecule. The overall negative CP experienced by the molecule (average = - 0.7389 a.u.) reflects that the distance is longer than the ideal. As the distance is decreased, the negative CP surface remains largely unchanged, with the major difference being the growth of the positive CP lobes on the back sides of the bond. By 0.70 Å, well past the equilibrium distance of 0.77 Å, a ring of positive pressure begins to become apparent around the waist of the molecule. Finally, at 0.65 Å, the positive CPs growth to the point that the

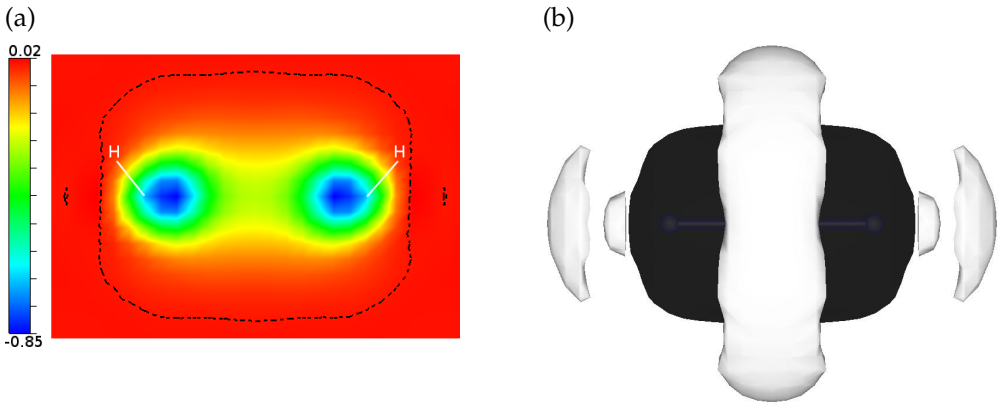

Figure 5.1: Chemical pressure plots of a single H_2 molecule. (a) 2D map of a plane containing the two H nuclei. (b) 3D isosurfaces with CP = +0.006 (white) and CP = -0.01 (black).

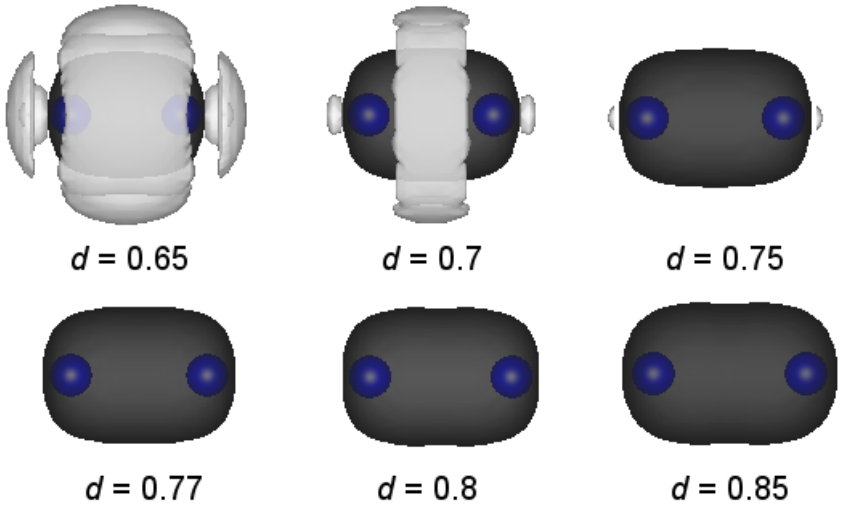

Figure 5.2: Chemical pressure distributions within a single H_2 molecule at several H–H distances. 3D isosurfaces with CP = +0.008 (white) and CP = -0.008 (black). The H–H distances denoted below each map are in Å.

negative CP region begins to shrink, qualitatively agreeing with the overall positive pressure now calculated for the molecule.

5.3.2 More complicated molecules: CO_2 and S_8

As we move beyond H_2 , one major difference is going to be the introduction of core electrons for heavier atoms. To some extent, the effects of the core electrons will be folded into the pseudopotentials we use for the atoms. Such features are illustrated by case of the CO_2 molecule (See Fig. 5.3). As can seen most easily in the CP profile across the molecule in the right panel, the deep wells of negative CP occur along the C–O contacts serving as the attractive component of the C–O interactions. Similar

to the case of H_2, the deepest minima do not lie at the center of the bonding region, but instead occur closer to the nuclei on the two sides of the bond. This time the minimum closer to the oxygen atom is significantly deeper, perhaps reflecting the oxygen atom's higher electro-negativity and the polarity of the bond.

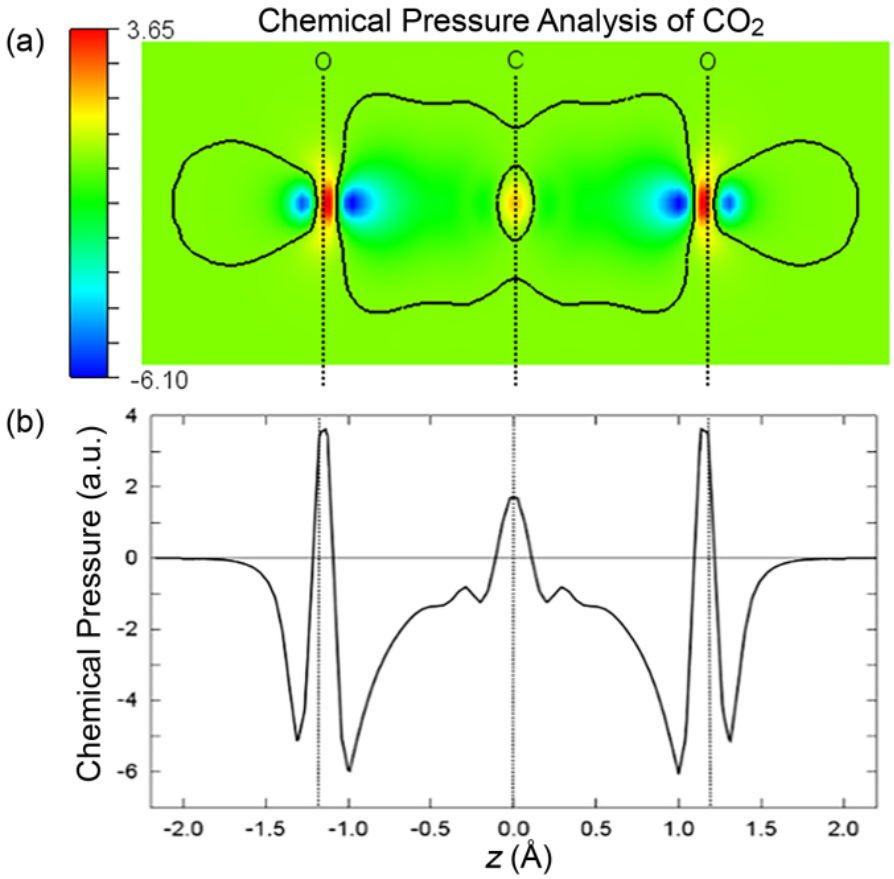

Figure 5.3: (a) 2D chemical pressure map of CO_2 molecule. (b) 1D profile of chemical pressure along the bonding line of a CO_2 molecule.

Several other new features are also apparent here. While in H_2 the positive CPs were spread out through the external area of the molecule, now they are concentrated into peaks centered on the C and O nuclei. The pseudopotential cores and perhaps the inner regions of the C 2*s* and O 2*s* orbitals now represent the major restoring force acting against the bonding regions' call for the contraction of the molecule. In addition, smaller positive CPs also occur the outskirts of the molecules, decaying toward zero at far distances.

This behavior is always seen for isolated molecules.

Another new entity appearing in CO_2 is well of negative CP projecting from the O atoms outwards along the axis of the molecule. In shape and orientation, these negative CP lobes resemble the sp- hybridized lone-pairs that are commonly drawn for the CO_2 molecule. Given our common association of lone- pairs with repulsion, as in the valence shell electron-pair repulsion (VSEPR) model, assignment of negative CP to a lone-pair is at first surprising. However, what this picture suggests that the lone-pair region in fact helps drive the contraction of the molecule. One explanation for this could be in how the electrons of the C-O bonds are distributed. They are focused in the C–O bonding region, opening access to the core on the opposite side

of the O atoms. The enhancement of this effect upon the contraction of the molecule would then lead to the negative CPs in the O lone-pair region. This view gives an alternative interpretation of the usefulness of the VSEPR model: electron pairs tend to maximize their distance from each other to support access to cationic core from different angles, rather than due to direct Coulombic repulsion between them.

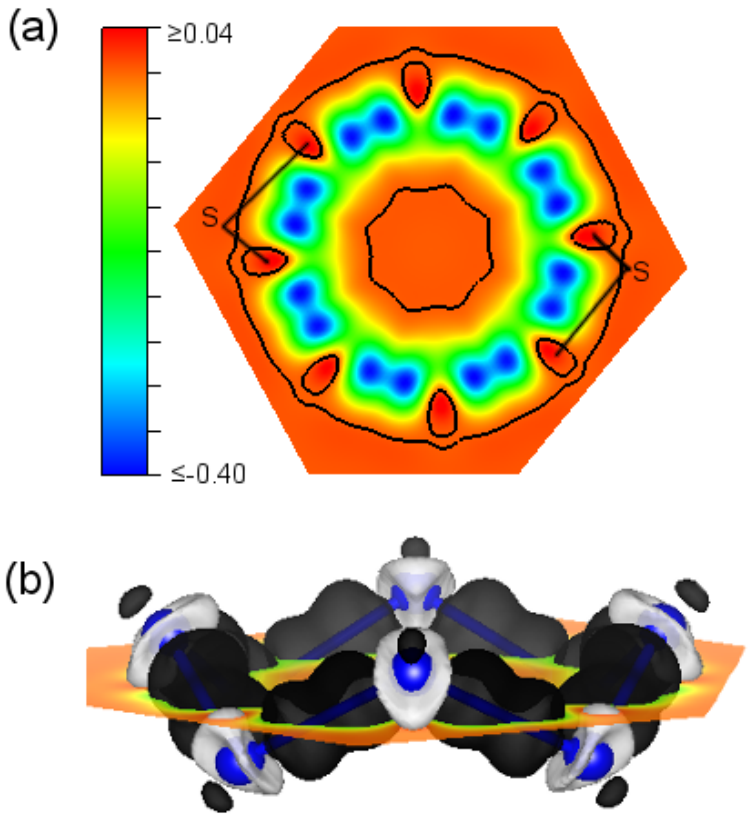

Figure 5.4: Chemical pressure plots of a S_8 molecule. (a) 2D cross- section along the plane intersecting the eight S-S bonds. Black curves: CP=0 contour. (b) 3D isosurfaces with CP=+0.02 (white) and CP= -0.17 (black).

The generality of these features for covalent systems can be seen in our last molecular example, the S_8 crown molecule (which we will soon examine in the context of crystalline sulfur). Taking a horizontal cross section through the molecule's boat-like geometry yields the 2D CP map of Fig. 5.4-a. Each S–S contact appears with blue dumbbell of negative CP similar to that observed for H_2, but with the minima now closer to the bond centers. In the 3D plot, these negative pressure features now manifest as black peanut-like shapes representing the S–S bonds, as well as a black lobe pointing outwards from each S atoms coinciding in space with the expected positions of sp^2- hybridized lone-pairs. The strongest positive pressures are associated with electron densities around the nuclear positions. Along with the core regions, a positive chemical pressure zone appears inside the boat S_8 configuration revealing the existence of steric repulsions. As with H_2 and CO_2, the CP distributions allow not only a visualization of the chemical bonds, but put them in the context of a balance of forces within the molecule.

The intense positive pressure is always indicated by red in the 2D plot and white surfaces in the 3D plot

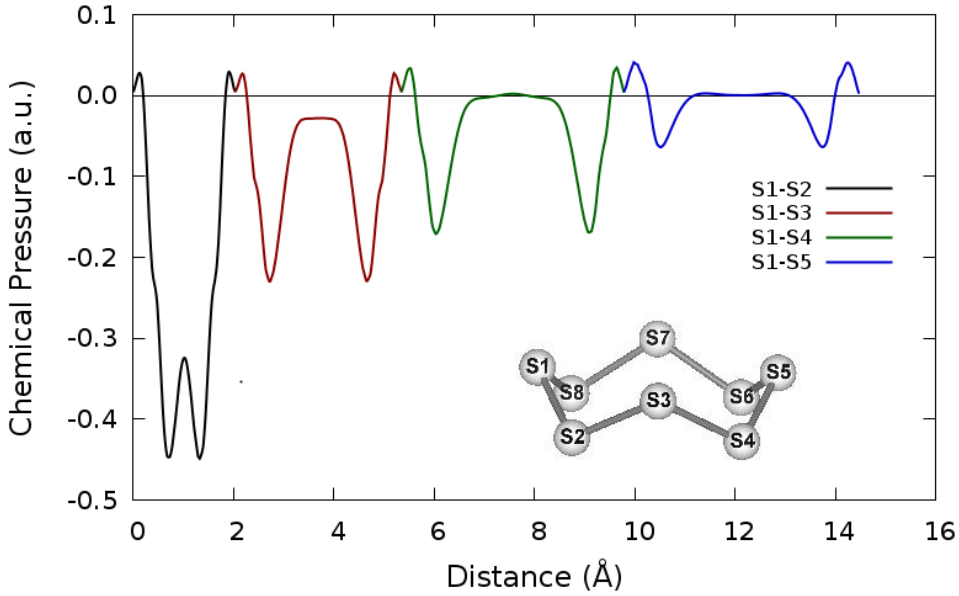

Figure 5.5: 1D CP profiles along the four different S–S paths in the S_8 boat configuration.

5.3.3 Systems built from covalent bonds: Graphene and Diamond

The themes we saw above continue uninterrupted when we build up from simple molecules to infinite lattices connected through covalent bonds. One simple example is graphene, in which a single honeycomb net of carbon atoms is held together through σ bonds and a delocalized π system. The 2D and 3D CP maps in Fig. 5.6 show the now familiar negative CPs along the bonded contacts, with the CP features necking at the bond centers. Around each C center, this creates a trefoil pattern of negative CP mirroring their sp^2-hybridization.

The most of the positive CP is localized around C nuclear positions, largely filling in whatever space is leftover by the C–C σ bonds. These positive CP features create a cloud of positive pressure above and below the carbon layer. Indeed for a CP value of +0.01 a.u., a continuous non-planar surface tracing out the atomic positions is obtained. Just at the centers of the hexagonal rings, a white hills of positive CP emerge also reflecting steric repulsion at the ring centers similar to that we detected before for the S_8 molecule.

Curiously, no appreciable negative CP is detected here for the π interactions along the graphene layer. Just above and below the C atoms, pits in the positive CP isosurface can be detected. These depressions may reflect the stabilization of the π electrons as π overlap allows them to grip more tightly to the C cores. The overlap of these regions with the positive CP components of the σ interactions would then prevent strong negative CP features from appearing at these points.

The CP map of the C-diamond, the quintessential covalent solid, can be understood in a similar fashion (Fig. 5.7). Negative CP features are again focused in the bonding regions along the C–C contacts, with positive CP poking out from the cores into the spaces between the bonds. As is shown with a [110] cross-section, the negative CPs between the C atoms show peaks close to the cores as in graphene. These

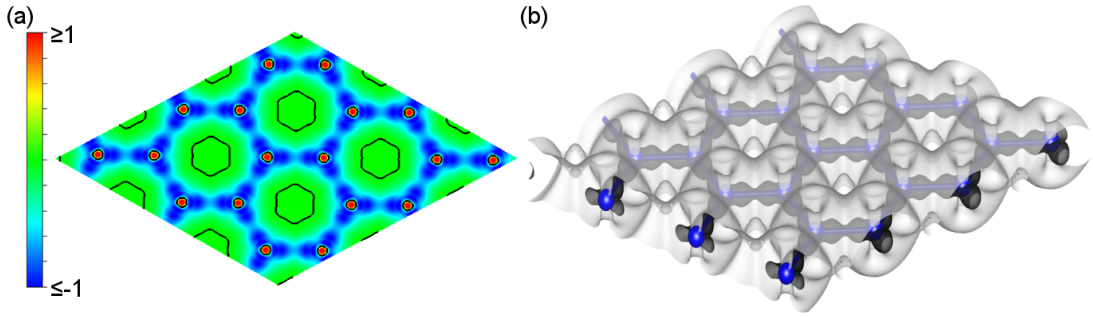

Figure 5.6: Chemical pressure plots of graphene. (a) 2D map of the [0 0 1] plane containing the C atoms. (b) 3D isosurfaces with CP = +0.01 (white) and CP = -0.6 (black) with black curves: CP=0 contour.

are somewhat dwarfed, however, by a new feature: a CP minimum directly at the bond center, which is less understandable from the Ruedenberg model of bonding.

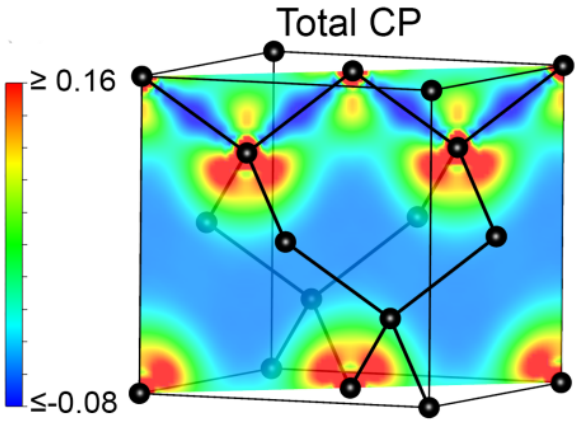

Figure 5.7: Cross-sections chemical pressure distributions of the diamond polymorph of C through [1 1 0] plane.

The origin of this CP pattern can be discerned by separately plotting the energetic contributions of the mapped energy as will be discussed in the next chapter.

5.3.4 Systems displaying both intra- and inter-molecular interactions: Graphite, CO_2 and S_8

In the examples we have thus far considered, the atoms of the structures have been linked together through covalent bonds. For molecules or the graphene sheets we discussed, these would rarely occur in isolation, but would instead interact with other molecules in their surroundings through non-covalent forces, such as van der Waals forces. Moving to molecular crystal structures offers an opportunity to explore the how such intermolecular interactions are manifested in the CP function (recognizing the well-known limitations of using DFT to treat van der Waals interactions).

Each carbon atom has an electronic configuration of $1s^2\ 2s^2\ 2p^2$. In graphite, the $2s$, $2p_x$ and $2p_y$ electrons form three sp^2 hybridized orbitals directed 120° apart on a

layer plane. The $2p_z$ electron, on the other hand, delocalizes in a π-orbital symmetry. Such type of electron delocalization could be identified by negative pressure (black waves) between the graphite layers (Fig. 5.8a), whic we assumed that is associated to the weak van der Waals forces between the layers.

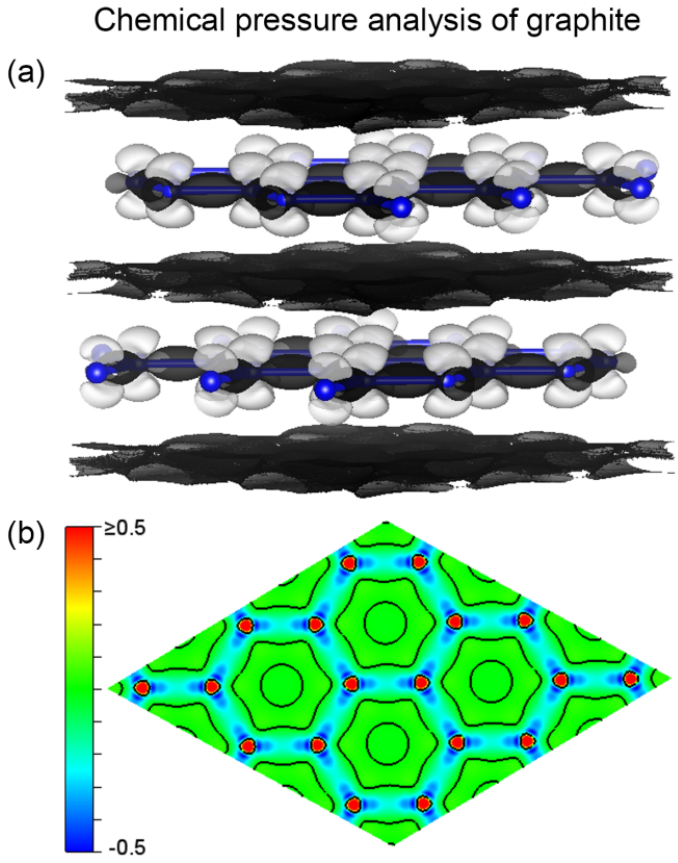

Figure 5.8: Chemical pressure plots of graphite. (a) 3D isosurfaces with CP=+0.07 (white) and CP=-0.02 (black). (b) 2D map of the [0 0 1] plane containing C atoms.

Let's start with the graphite structure, built from ABA stacking of graphene layers held together with weak van der Waals intralayer interactions. The CP map of graphite is shown both as a cross-section through a single layer and with isosurfaces for 3D structure in Fig. 5.8. Within the individual layers, the CP distribution is very similar to that of the isolated layer, emphasizing the secondary nature of the interlayer interactions. Each C atom has three wells of negative CP, one directed toward each of its C neighbors in the sheet (See Fig. 5.9). The remaining space around the C core is taken up by positive CP, corresponding to regions of space where the deviations from the wavefunction away from the atomic orbitals of a free atom are not compensated by bond formation.

The major differences between the CP features of graphene and graphite are instead appearing at the surfaces of the layers. In graphene, the spaces above and below the graphene layer exhibit positive CPs, again arising from the perturbations to the C atoms to allow C–C bond formation. In graphite, this situation changes, with negative CPs now occurring between the sheets. The presence of negative pressure in this interlayer region is reassuring, as it suggests an attractive force is

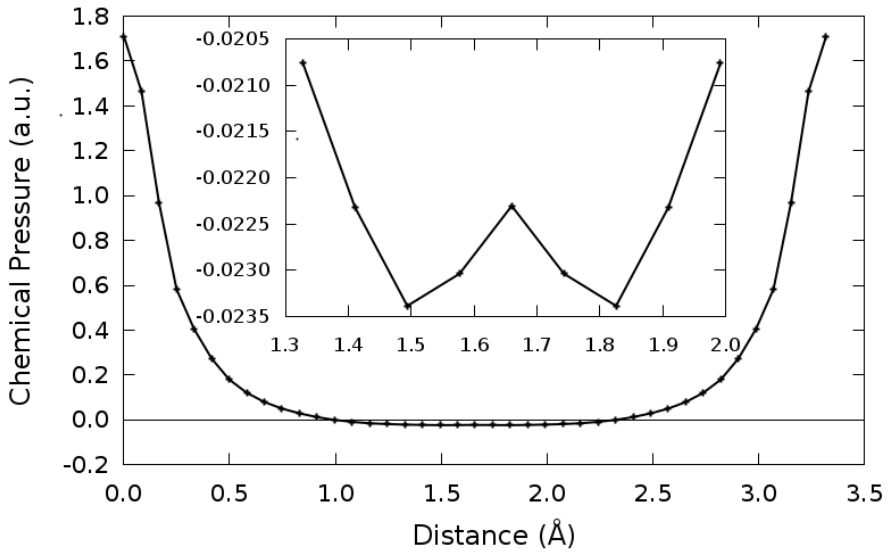

Figure 5.9: 1D profile of chemical pressure distributions along the C–C covalent bond.

holding the layers together. Perhaps more interesting, though, is the way in which it is distributed. As in the covalent bonds seen earlier, the negative CP is concentrated not at the mid-points between the interacting atoms, but instead closer to the atomic centers; in this case, the isosurfaces show black surfaces that stick close to the upper and lower sides of each layer. This suggests a small degree of covalency to the interaction, the source of the band dispersion along the interlayer direction.

The molecular crystals of S_8 (homonuclear) and CO_2 (heteronuclear) have been chosen to be compared with their isolated forms. In both cases, the CP maps (see Figs. 5.10 and 5.12) are able to identify the S_8 rings and CO_2 linear molecules within their respective unit cells. In the case of the 2D dimensional plots, the zero pressure isoline constitutes a clear boundary that encloses the nuclear positions. They are identified by positive (red) chemical pressure. In the case of S_8, the CP is represented in the same equatorial plane intersecting S–S bonds as in our previous example of the isolated molecule. Therefore, we really observe projections of the CP from these nuclear positions and the S–S bonds. The latter are identified by dark blue small lobes between the S nuclei (see Fig. 5.10b).

One important difference with respect to the molecule is that no positive pressure is found inside and outside the rings, being the CP values in these regions around -0.02 a.u. We noticed that, as in graphite, S_8 rings are located in a similar stacking with S atoms on top and below the centers of the S_8 boat configuration as shown in Fig. 5.11. As a result, weak interactions between the S_8 units could be identified by the negative CP in this region.

As regards CO_2, we observed regions of negative pressure associated again with the C–O bonds and the O lone pairs. Outside the CO_2 units, the background of CP, as in the S_8 molecular crystal, is negative and also close to -0.025 a.u.. Similarly, this is probably an indication of the weak but attractive interactions between the molecular-like units of these crystals. The 3D plots allow visualizing the planes chosen for the 2D representations and clearly show the bonding within the S rings and in the CO_2 molecules.

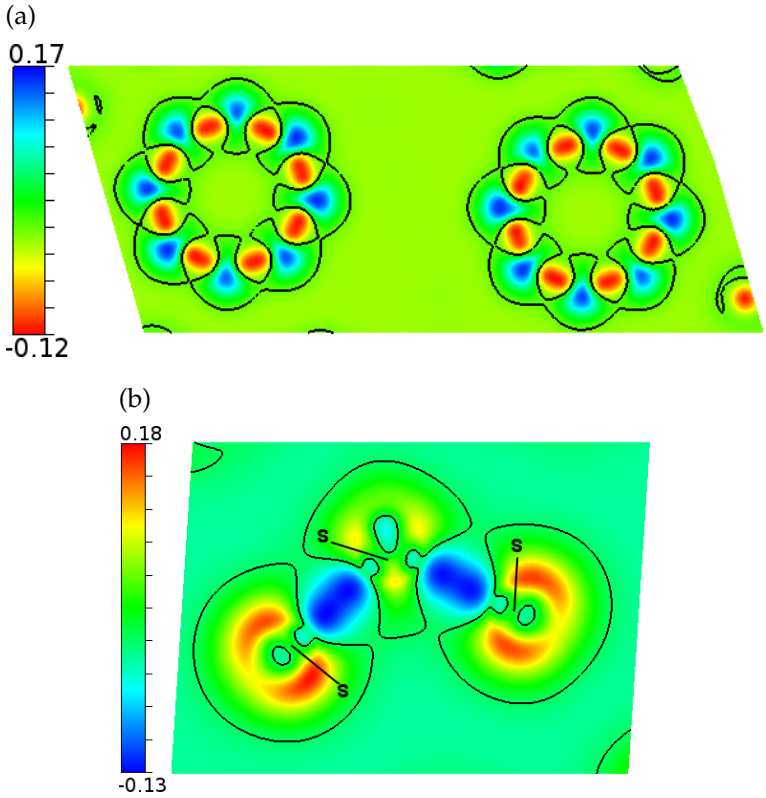

Figure 5.10: Chemical pressure maps of the S_8 molecular crystal structure through a plane (a) intersecting S–S bonds and parallel to the planes containing the two sets of four S atoms of the S_8 boat configuration (b) containing three consecutive S atoms.

The comparison with ELF results (See Fig. 5.12b) shows that the analogies are more than aparent. The ELF topology of CO_2 polyomorphs has been discussed in details by Contreras-García *et al.* [16]. ELF is also able to identify CO_2 units with basins associated with C and O cores, the double C–O bonds, and the O lone pairs. We would like to highlight that the importance of this similitude is in the origin of the scalar field used in the representations. Whereas the ELF is a function based on the electron density, the chemical pressure is based on the energy.

5.3.5 Chemical pressure of the hydrogen bond: ice-I_h

We now turn to another type of intermetallic interaction, the hydrogen bond. These interactions have often considered as being primarily electrostatic in nature, with the partial positive charge of a H atom in an X- H bond (X = O, N, F, or other electronegative atom) being attracted to the lone-pair of a nearby atom. This picture, however, has been enriched by theoretical calculations such experimental data as NMR couplings constants, which show that hydrogen bonds have a substantial quantum mechanical component, most easily understood in terms of the partial donation of the lone-pair into the X-H σ^* orbital. This element of covalency in the hydrogen bond is readily seen in the CP maps, as we will now demonstrate using the low pressure I_h phase of ice.

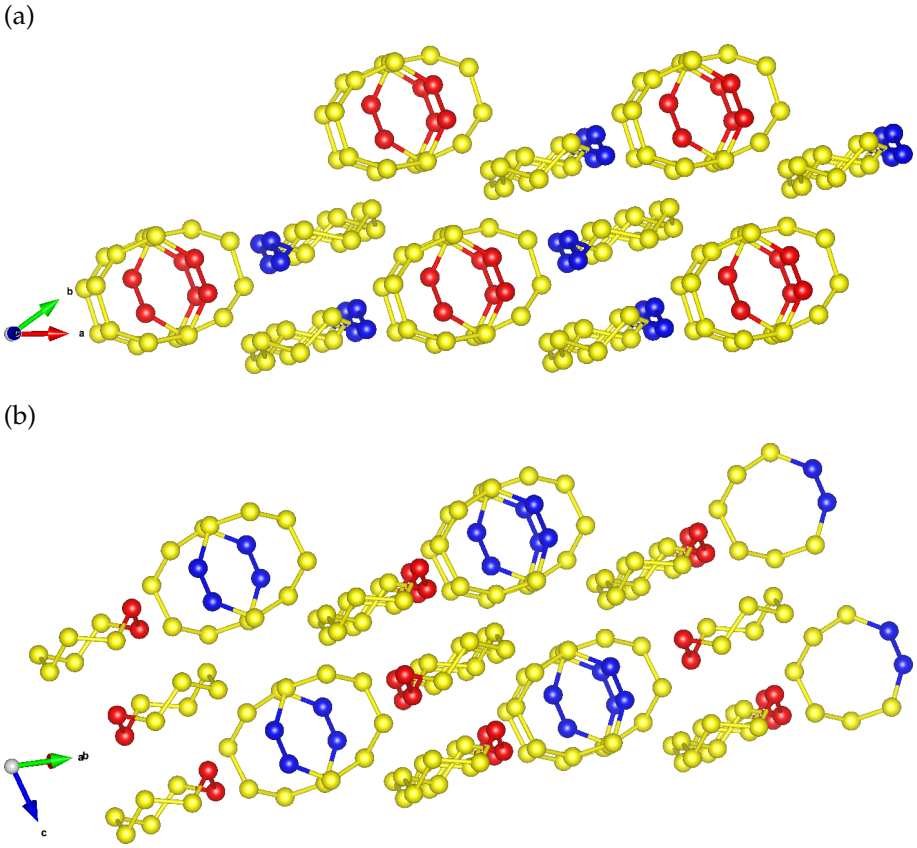

Figure 5.11: Stacking between the S_8 units in molecular crystal structure (a) projection along *c*-axis. (b) through *bc* plane.

In this structure, the oxygen atoms exhibit the typical four-fold coordination by H atoms forming a distorted tetrahedral in which two hydrogen atoms are covalently bonded while other two come from neighboring water molecules. This is displayed in the 3D plot of Fig. 5.13. If we look at the white lobe corresponding to one of the central oxygens of the selected blue plane, we observe two black lobes emerging from it toward the closer H atoms, while a black disk marks appears at the more distance H atoms. The former represent covalent bonds similar to those we have seen for other molecules.

A 2D cross-section of the CP map allows us to look more deeply into the CPs of the O-H and O$\cdots$H interactions (See Fig. 5.13a-top). The red color is associated with the high pressure regions surrounding the oxygen position, while the O-H$\cdots$O lines are mostly faint blue indicating negative CP. More importantly, the intensity of the blue color in the O-H$\cdots$O regions becomes darker when we move from the H-bond to the covalent H–O bond. We noticed that the negative pressure associated with the H-bond does not touch the oxygen position as the covalent bond does. The position of the H nucleus is inside the dark blue lobe of the covalent bond.

The relative scales of these interactions are more clearly illustrated in a 1D profile of the CP function along a O-H$\cdots$O path (Fig. 5.13b). Here, the covalent bond appears as a deep double well of negative pressure, with the H atom situated toward the outside of one of these wells. The hydrogen bond region is much more shallow, and almost resembles and extension of the negative CP of the covalent bond into

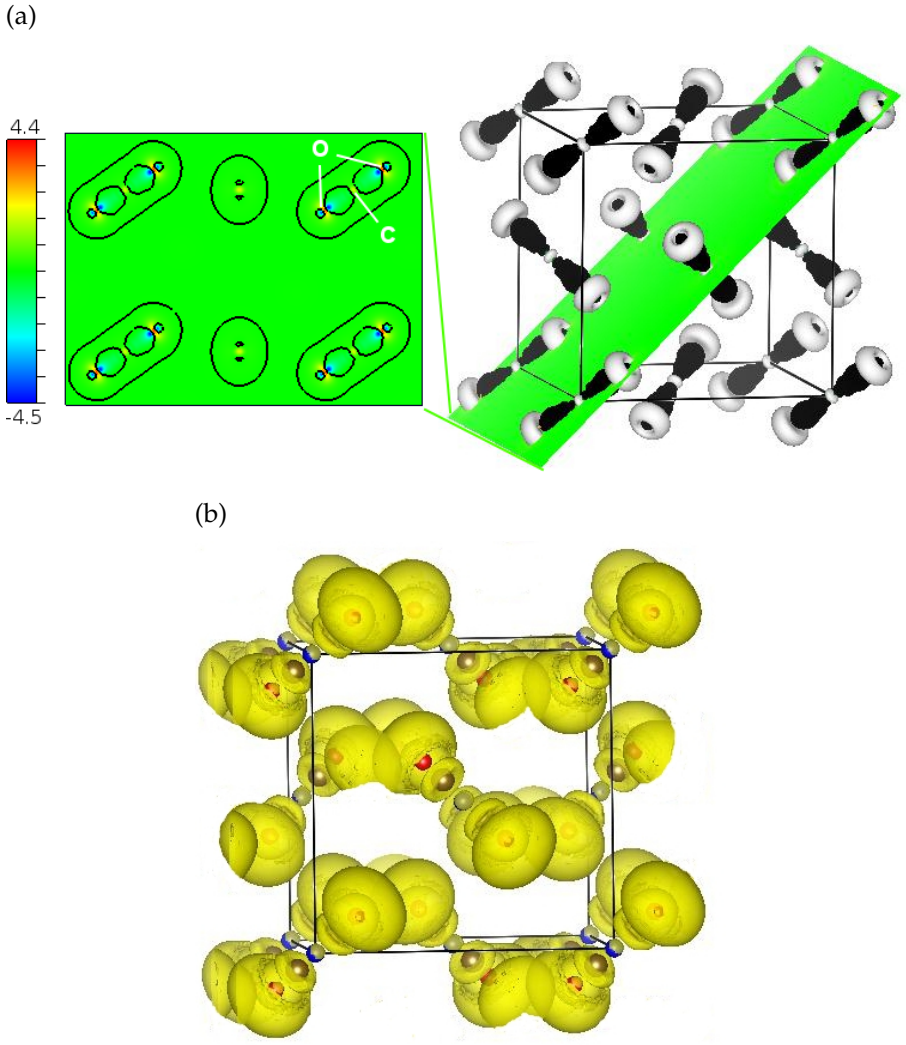

Figure 5.12: Chemical pressure maps and ELF of the CO_2-I molecular structure of carbon dioxide. (a) 2D $[1\,\bar{1}\,0]$ plane containing nuclei of C and O atoms of CO_2 units (left) 3D isosurfaces with CP = +0.5 (white) and CP = -0.3 (black) (right). (b) 3D isosurfaces with ELF = 0.8.

the intermolecular region. In the oxygen side of the hydrogen bond there is a shoulder of positive pressure. The source of these CP features can be detected through examining separately each energetic contribution to the chemical pressure as will be discussed in the next chapter.

5.3.6 Metallic bonding: Na, As, Sb and Bi

It is well-known that the valence electron density of a metal can be thought of as derived from a homogeneous electron gas within the free electron model. With this in mind, we should not expect negative chemical pressure in specific localized regions of the metal but in a *plateau* dominating the interstices around the atomic positions of positive chemical pressure. As illustrated in Fig. 5.14 (left), there is a circular isoline of a zero value enclosing the Na nuclear positions. The spherical

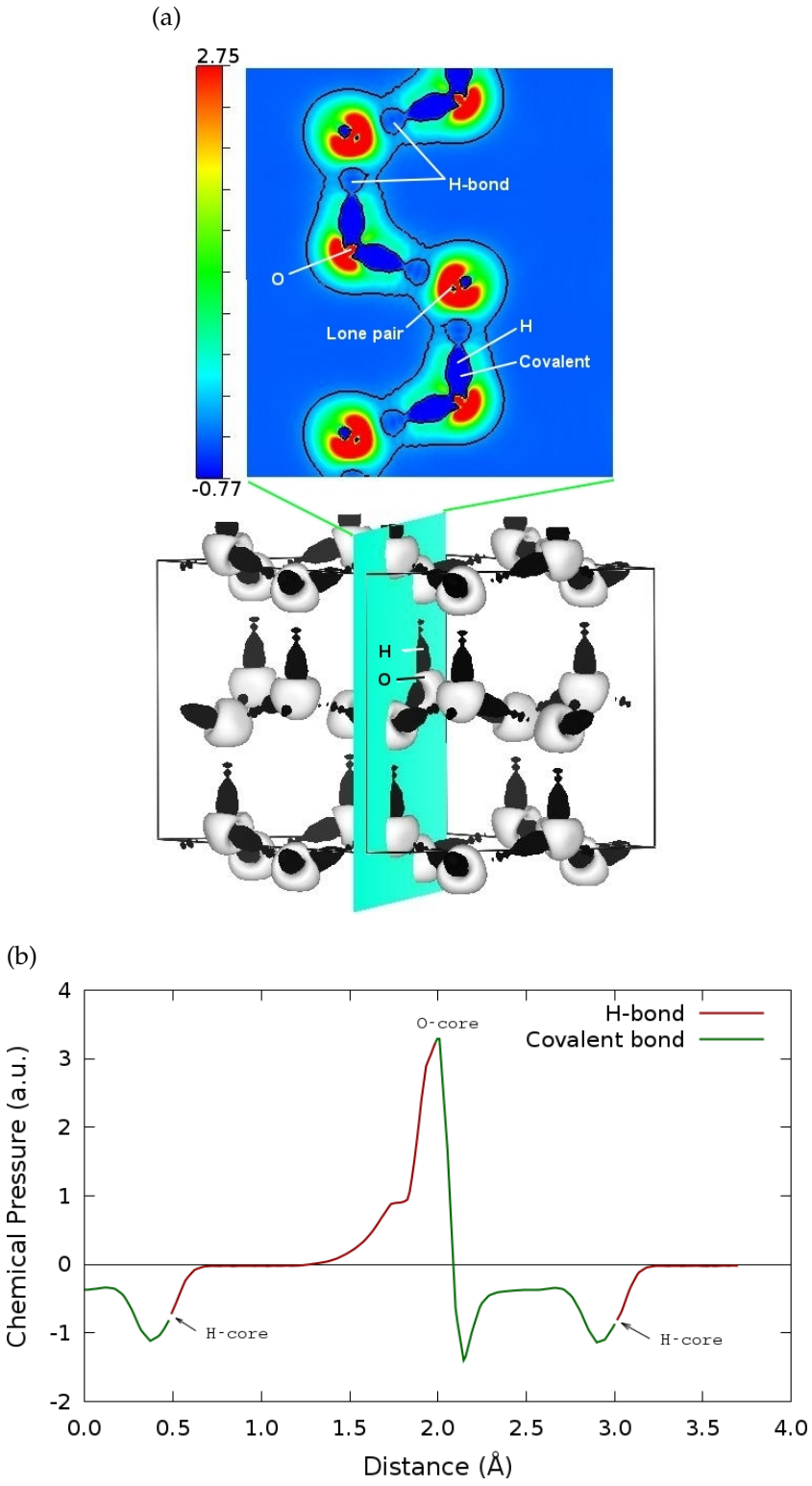

Figure 5.13: Chemical pressure plots of water in the Ice-I_h phase. (a) 3D isosurfaces with CP = +0.1 (white) and CP = -0.016 (black) and 2D $[1\,\bar{1}\,0]$ plane containing nuclei of water molecules with H– O covalent bonds and H$\cdots$O hydrogen bonds. (b) 1D profile of CP versus distance along covalent and hydrogen bonds.

symmetry of the chemical entities associated with the Na atoms can be detected in both 2D and 3D CP maps and correspond to Na cores. For a low positive value of CP +0.02 a.u., the isosurface encloses an sphere centered at the nuclear position of Na as illustrated in Fig. 5.14 (right). The *plateau* region of negative chemical pressure can also be clearly visualized.

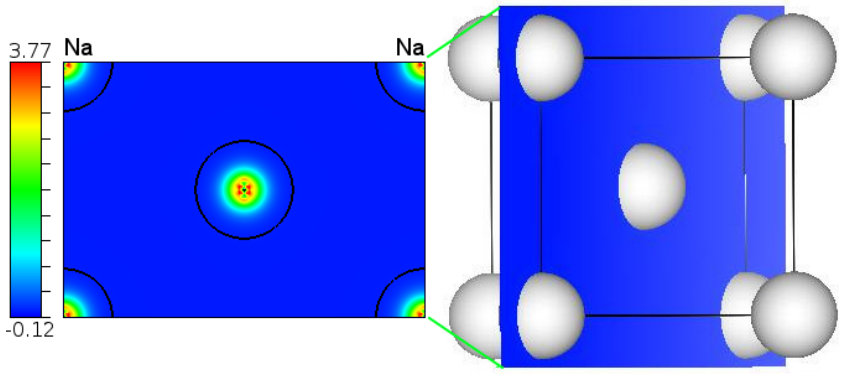

Figure 5.14: Chemical pressure plots of metallic Na in the *bcc* structure. (Right) 3D isosurfaces in the conventional cell with CP = 0.02 (white). (Left) 2D $[\bar{1}\,0\,\bar{1}]$ plane at z = 0 in the conventional cell.

The expected increasing metallic character as we go down along the group 15 is explored by analyzing the CP plots of As, Sb, and Bi (See Fig. 5.15). For the overal comparison, it is convenient to use a single CP scale for the three crystals. Thus, the intensity and variation of the blue color in the intestitial space provide a first visual indication of the trend in the metallic character along this series. As expected, the observed sequence of increasing metallicity is As, Sb, and Bi. Besides, Fig. 5.16 shows the trend of CP along the nearest neighbor (nn) and next nearest neighbor paths.

These trends can be used as a basis for a CP-based definition of metallicity. To give a quantitative account, we have tested the validity of two different indexes of metallicity. The first index was proposed by Silvi and Gatti [117] and measures the delocalization within a metallic structure as the ELF difference between the max-

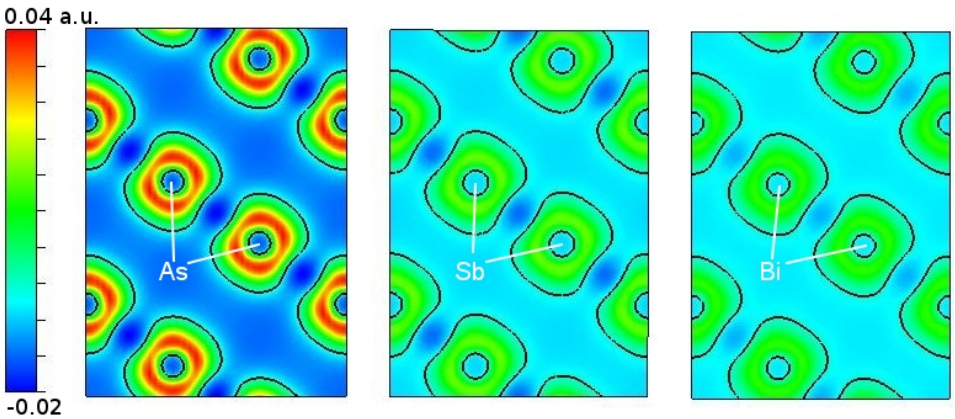

Figure 5.15: DFT-CP cross sections through the [1 1 0] plane in As, Sb, and Bi (from left to right).

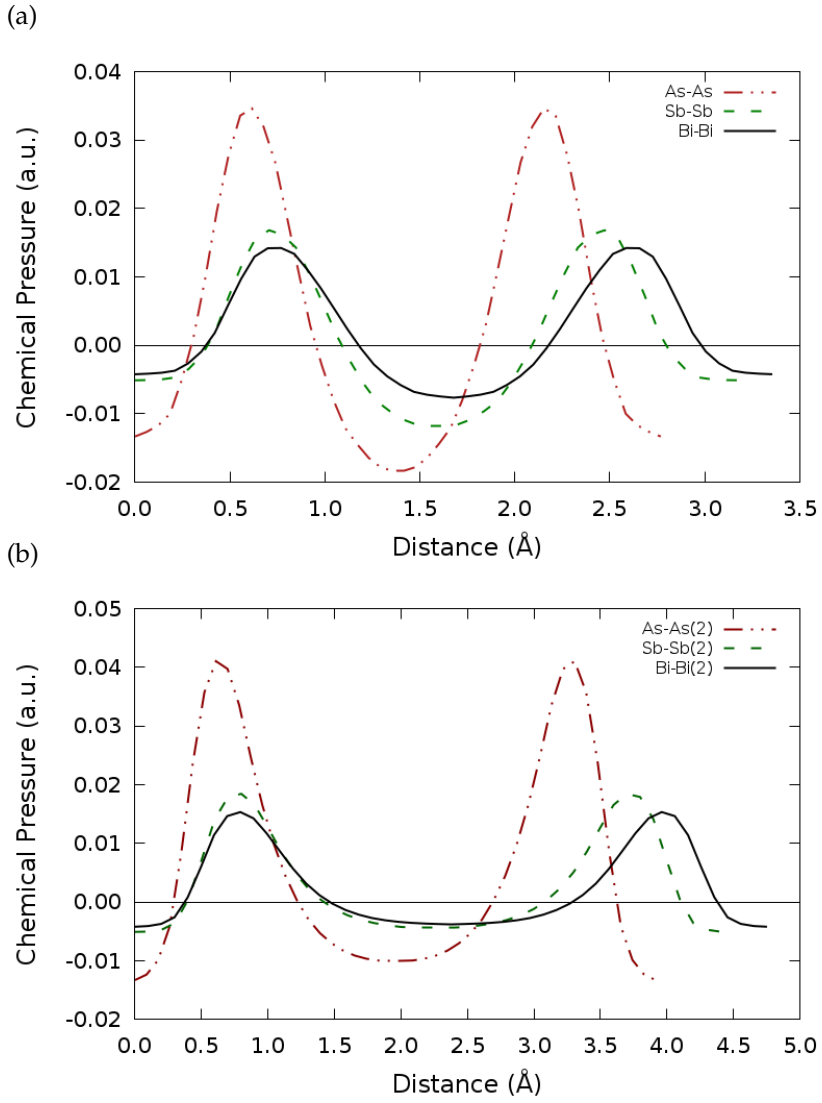

Figure 5.16: Chemical pressure versus distance of metallic crystals As, Sb, and Bi along (a) the nearest neighbor (b) next nearest neighbor paths.

ima and first-order saddle point of the valence basins. This index can be adapted and reformulated for these specific compounds using chemical pressure values as follows:

$$\Delta(\mathrm{CP}) = \mathrm{CP}_{nn} - \mathrm{CP}_{nnn}, \tag{5.1}$$

where CP_{nn} and CP_{nnn} are the absolute values of the lowest chemical pressure values along the nearest neighbor and next nearest neighbor paths, respectively. Accordingly, we have obtained decreasing $\Delta(\mathrm{CP})$ values of 0.0082, 0.0074 and 0.0038 a.u. for As, Sb, and Bi, respectively. The chemical pressure difference is the lowest in Bi since the delocalization is the highest, in agreement with the greatest metallic character as we go down along the elements of group 15.

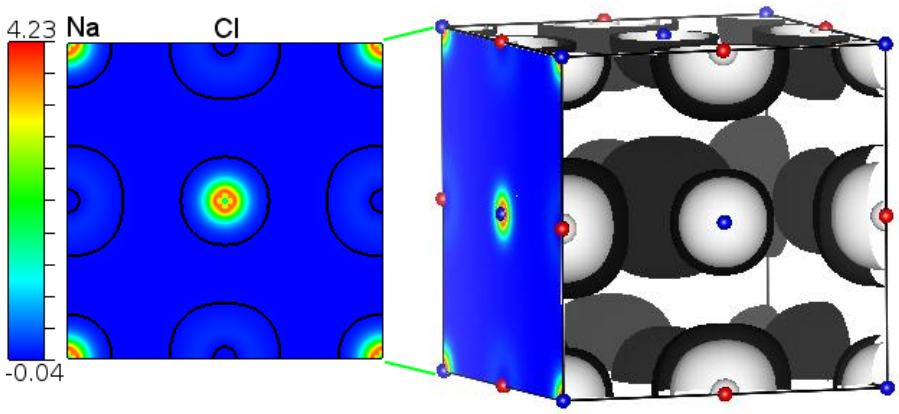

Figure 5.17: Chemical pressure plots of ionic NaCl in the rocksalt structure. (Right) 3D isosurfaces with CP = +0.026 (white) and CP = -0.026 (black). (Left) 2D [0 1 0] plane at $y = 0$.

The second index was recently proposed by Jenkins [61]. According to the theory of atoms in molecules (AIM), the bond metallicity can be determined from the electron density (ρ) properties at the bond critical point (bcp) using the ratio:

$$\xi(r_{bcp}) = \frac{\rho(bcp)}{\nabla^2\rho(bcp)}, \tag{5.2}$$

This can be written within the chemical pressure framework as follows:

$$\xi(CP) = \frac{CP_{nn}}{\nabla^2 CP_{nn}} \tag{5.3}$$

Interestingly, this ratio gives an ascending order of 0.165, 0.244 and 0.299 for As, Sb, and Bi, respectively, thus confirming the expected metallic trend.

5.3.7 Ionic bonding: NaCl

The zero CP isoline is able again to identify the meaningful chemical species in the ionic rock-salt structure of NaCl. Cations and anions are visualized with spherical shapes according to our 2D and 3D plots. The highest positive pressure is localized at the Na^+ positions, whereas the positive CP value associated with Cl^- is lower. This result is within the expectations for a higher electron density on the cation compared to the one on the anion. The interstitial space has low and negative CP values. In the 3D plot, it is however observed that the drop in CP from the zero value isoline follows an isotropic behavior, with spherical black isosurfaces surrounding the concentric isosurfaces of positive pressure (See Fig. 5.17).

6 ENERGETIC CONTRIBUTIONS TO THE CHEMICAL PRESSURE

CONTENTS

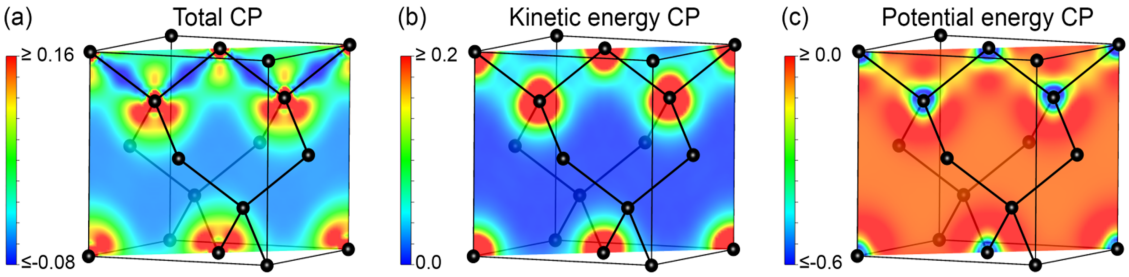

Chemical pressure maps of the diamond polymorph of C. [1 1 0] cross-sections are shown for (a) the total CP, (b) the kinetic energy component of the CP, and (c) the potential energy contribution to the CP.

6.1 INTRODUCTION

We have proposed the use of chemical pressure (CP) concept as a convenient tool to identify different chemical bonding networks in crystalline solids displaying various forms of localized and non- localized interactions, including covalent, ionic, metallic, van der Waals and hydrogen bonding as described in chapter 5. This was achieved by coupling the chemical pressure analysis within the framework of the density functional theory (DFT-CP program). In this chapter, we examine separately each energetic contribution to the chemical pressure map in a straightforward way to understand the source of the positive and negative CP regions within the crystalline unit cell space. We observed that the four meaningful energetic contributions to the chemical pressure, the kinetic, exchange-correlation, local pseudopotential, and Hartree, show characteristic features just around the nuclei and along the bonding paths showing a flat behavior in the interstitial space. This analysis reveals systematic trends that allows us to draw some general conclusions. Overall, kinetic chemical pressure is positive and dominates the core regions whereas the local pseudopotential contribution is responsible for the localized covalent bonding. It is also worth to emphasize that lone pair regions exhibit negative values of chemical pressure for the four mapped contributions surrounded with a zero value isoline only in the kinetic energy and local pseudopotential maps. Our analysis leads to an interesting analogy between metallic and ionic systems, both displaying the same trends for the local pseudopotential and the total chemical pressure one-dimensional profiles. Weak interactions and hydrogen bonding are identified by very low values of all CP contributions around the center of the interaction path along with a distinctive behavior of the Hartree and local pseudopotential terms around the nuclei positions.

6.2 RESULTS AND DISCUSSION

6.2.1 Chemical pressure contributions of isolated Molecules: H_2, CO_2 and S_8

We will follow almost the same sequence as of the previous chapter in discussing separately the energetic contributions to the chemical pressure of the systems presented in chapter 5. Then we will start with the simplest molecule, H_2 molecule, in which the H core is empty. Figure 6.1a shows the pure CP maps of each contribution separately.

The cross sections of each energetic contribution were plotted using the CP original scale. The KE is mostly positive over the entire unit cell except in regions associated with the bonding between the H nuclei. Hartree term is also positive at each *voxel* of the unit cell, including a small region with negative value, nearly zero, around the H_2 molecule. Rescaling the four cross sections, it is shown that the negative CP features (blue) near the nuclei are due to the XC and Local PSP terms while intense positive pressure (red) is surrounding the H atoms and along the bonding region is mainly from respectively KE and Hartree terms. Another way to explore the CP maps of the main four mapped energetic contributions is to select the maximum positive and minimum negative CP value in the four CP maps and

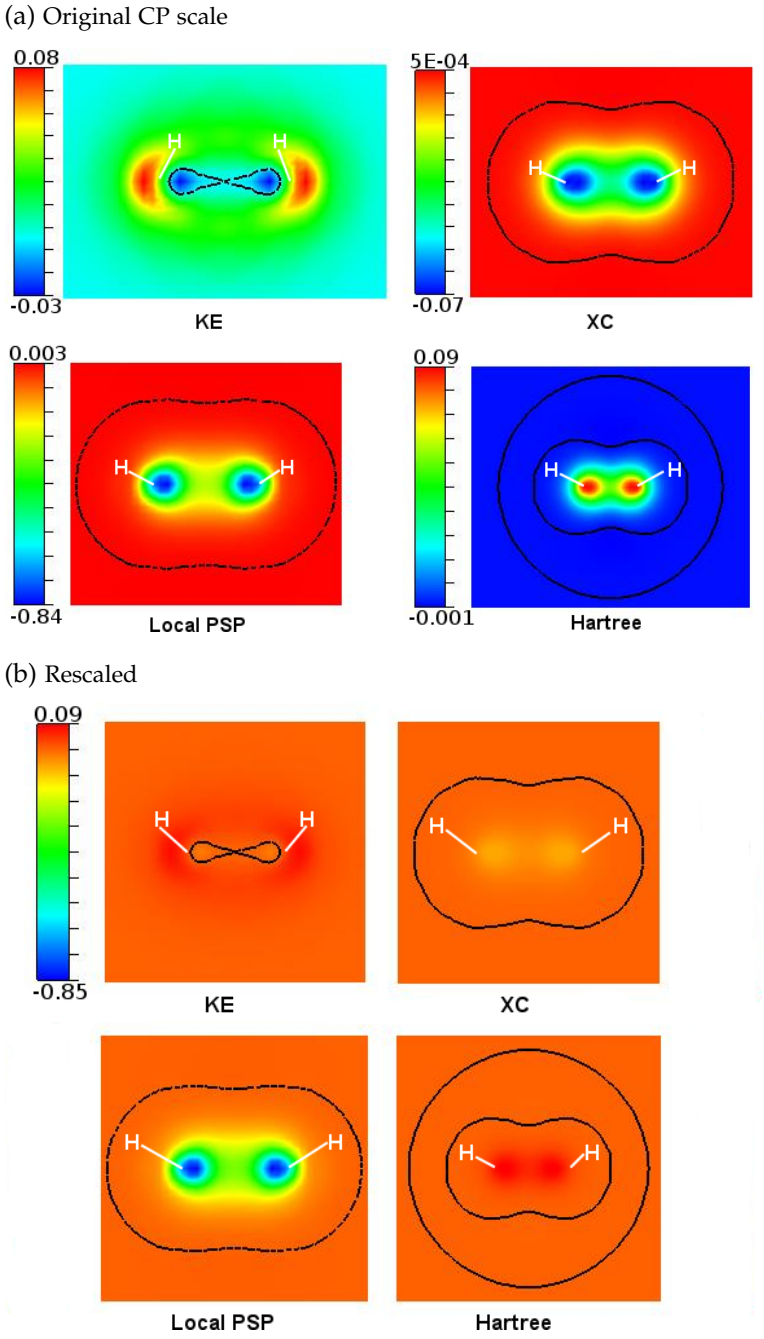

Figure 6.1: DFT-CP distributions calculated for isolated H_2 molecule. (a) Cross sections of the four separate energetic contributions through the nuclear positions using the original scale. (b) Same cross sections in (a) but adjusted to a common scale.

rescale them as shown in Figure 6.1b. Then, it is easier to identify where the strong positive and negative features come from. Since the four CP maps have a common scale, the positive pressure (red) arises from the KE and Hartree terms while the negative pressure (yellow-blue) is mainly due to the local potential and XC terms.

In Fig. 6.2, the covalent H–H bond appears as a deep double well of negative pressure, with the H atom situated toward the outside of these wells. Positive Hartree and negative XC components are opposite and cancel each other. However, KE term

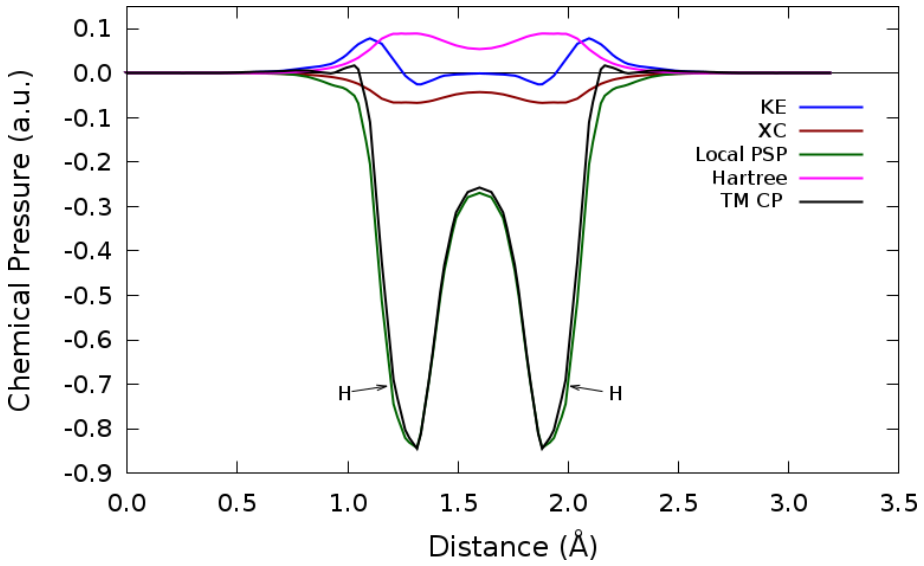

Figure 6.2: 1D plot displaying the variation of the total mapped CP and each mapped energetic contribution with distance between the H nuclei

is almost zero at the bond center and also near the nuclei. Hence, the total mapped CP comes mainly from the local potential contribution which is the most negative term in the CP map. The negative pressure region was expected since the H core is empty.

In case of isolated CO_2 molecule, as shown in Fig. 6.3b, The high positive pressure at the nuclei is because of the well localized electrons where the kinetic energy is maximum. Besides, the local pressure is a non-positive function between the nuclei. This implies that the potential becomes more negative as the cell contracts. Hence, the local component provides a severe negative feature between the atoms while both KE and Hartree components provide the more positive features at the atomic positions. The total mapped CP along the CO_2 molecule is very defined by KE and local potential contributions since their maps display the most positive and most negative pressure values, respectively. The bonding electrons and the lone pairs of O are detected by intense negative pressure (blue). As done with the H_2 molecule, the cp maps of the energetic contributions were rescaled in Fig. 6.3b using the maximum positive and the minimum negative CP values shown in the top panel.

The variation of CP with distance along the bonding path of the linear CO_2 molecule is shown in Fig. 6.4. Near the atomic cores, the KE term is maximum while the rest of the contributions are almost zero. Also Hartree contribution changes in a positive scale indicating that it becomes more positive as the cell contracts since the bonding electrons experience a higher repulsion forces at lower volume.

Orthorhombic sulfur displays S_8 molecules with boat configuration in which a pair of four S atoms forming a square are lying in two different planes [96]. In Fig. 6.5a, we show a cross section of the resulting total mapped CP distributions along a plane intersecting the S_8 boat leaving four S atoms at each side of that plane. Also another cross section, including three S atoms connected by two covalent bonds, is shown in the right panel. The bond between S atoms is marked by intense negative pressure (blue). The most intense positive pressure is located at the nuclei while a region of negative pressure, which is nearly zero, is centered inside the boat

Total mapped CP (TMCP) is the total CP **without** *adding the non-mapped contributions to the background.*

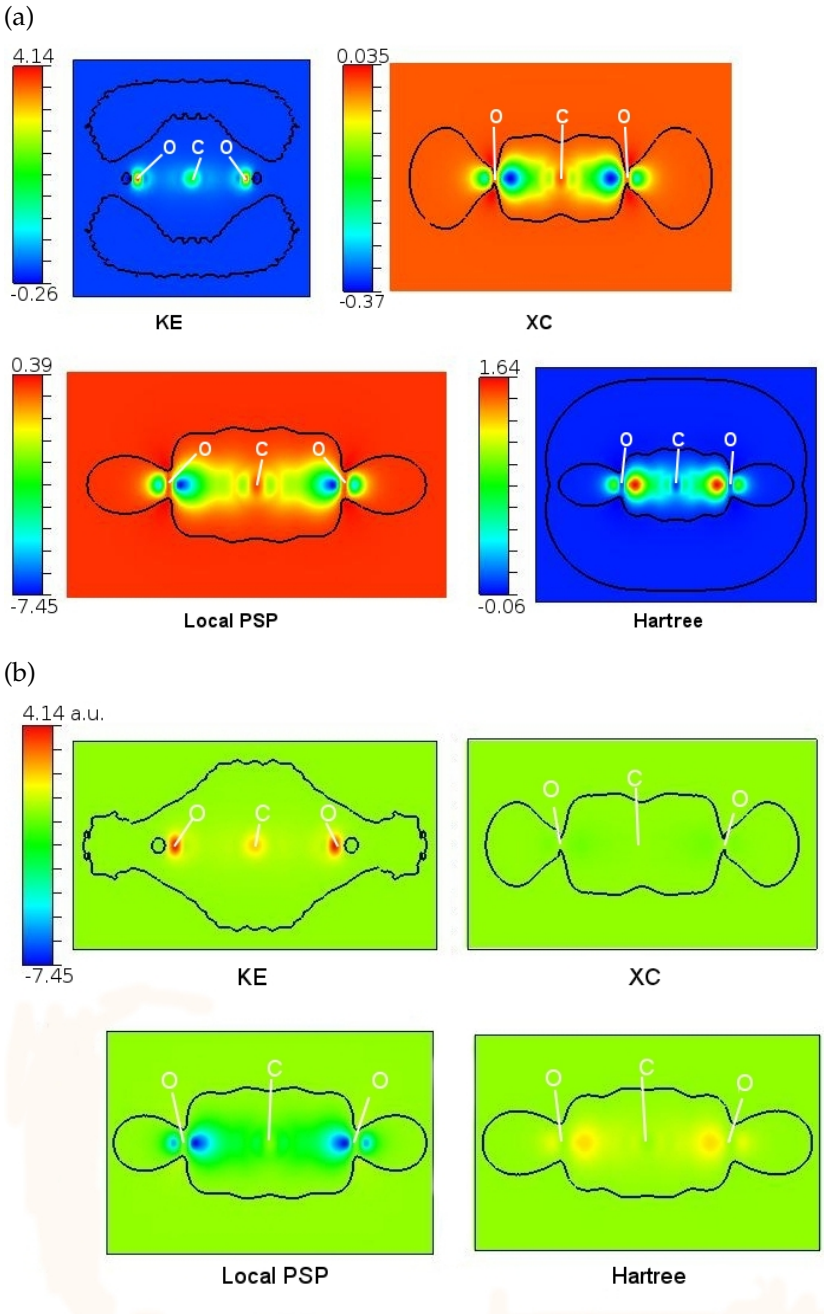

Figure 6.3: DFT-CP distributions calculated for isolated CO_2 molecule. Cross-sections of the energetic contributions to CP (a) using the original CP scale and (b) rescaled. Black contours drawn for CP=0.0 to indicate transitions between negative and positive CP values.

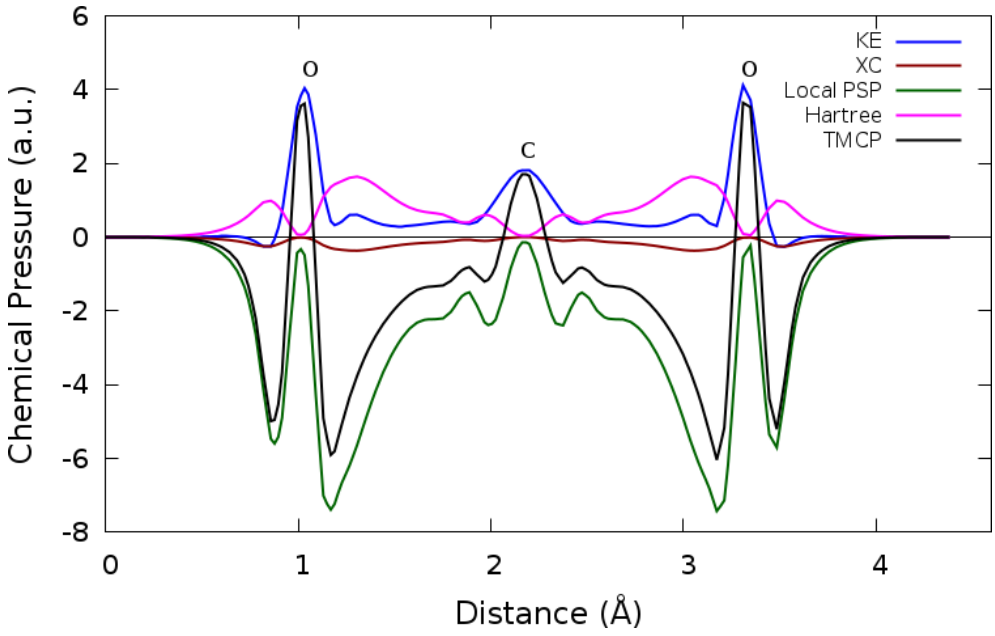

Figure 6.4: 1D profile of the chemical pressure contributions along the linear CO_2 molecule.

configuration. As seen in the previous isolated systems, the CP in the space faraway from the molecule is positive and gradually decreases to zero as the distance from the nuclei increases. Moreover, a region of negative pressure (green) is assumed to be associated to the lone pairs of S (See Fig. 6.5a-right).

Now we will explore the source of these CP features in the light of the mapped energetic contributions. Figure 6.5b shows how the CP changes between atoms. The most intense CP is localized near the nuclei. The KE and Hartree components are positive functions along the S–S bond while the local potential and XC components show negative behavior. It seems that the weak negative pressure seen at the center of the boat configuration of S_8 molecule in Fig. 6.5a-right comes from both local potential and XC components since their cross sections show negative pressure at the same region (See Fig. 6.5b). Another possibility to explore the CP distribution of each energetic component along three consecutive S atoms connected by two bonds is shown in Fig. 6.5c. In these cross sections, the lone pairs of one S atom are identified by negative pressure region in KE, XC and local potential components while by positive Hartree pressure. The other lone pairs are located in another plane nearly perpendicular to this.

In addition, we show in Fig. 6.6 the trend of the total mapped CP (TM CP) between two opposite S atoms passing through the center of the boat configuration. Although it is seen of positive pressure in the total CP cross section in Fig. 5.4b, the S_8 boat configuration center is seen now of negative pressure. Hence, this center is positive because of the homogeneous addition of the total non-mapped energetic contributions ($\approx$ +0.001) to each voxel in the cell. Examining the non-mapped components, Ewald energy pressure is higher positive than non-local components. Ewald energy represents the Coulomb repulsion between the ions in a crystal lattice which becomes positive as the cell contracts.

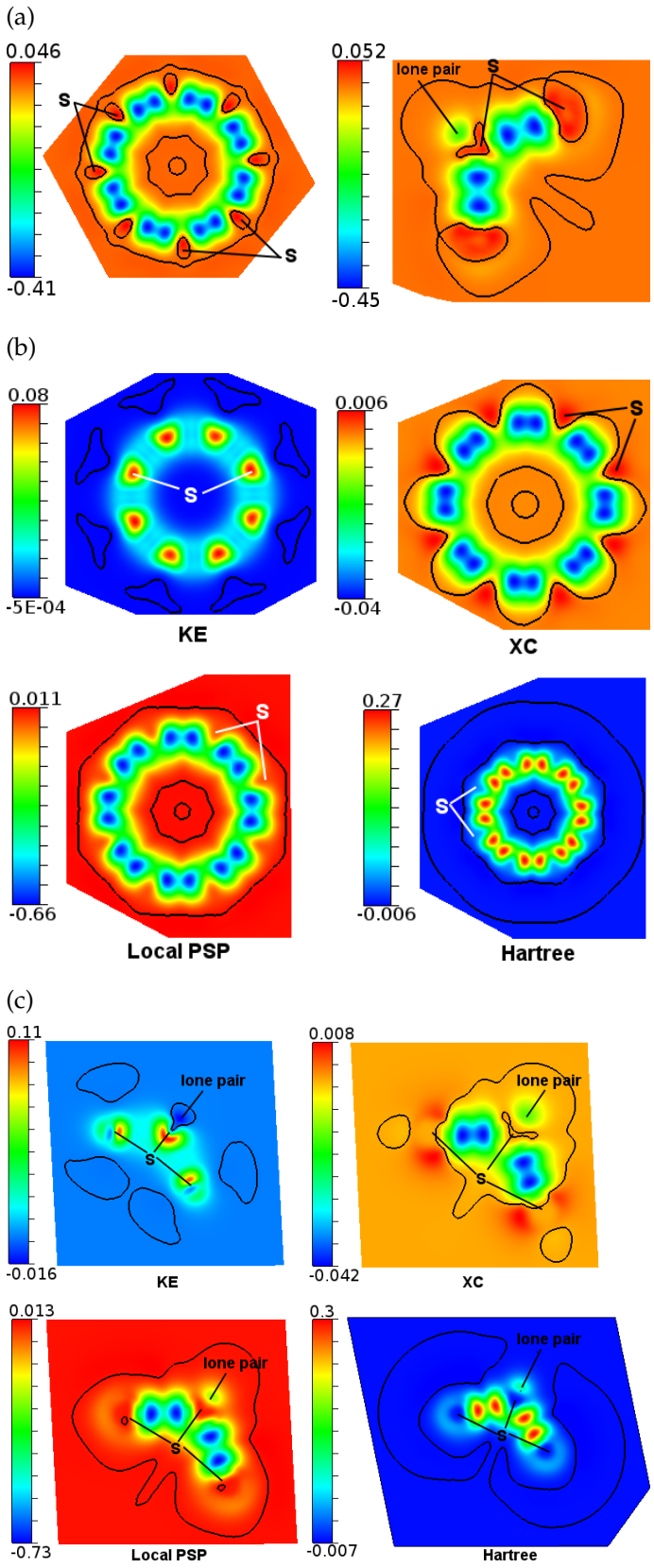

Figure 6.5: DFT-CP results of isolated S_8 molecule. (a) Cross section of the total mapped CP through (left) a plane intersecting S–S bonds (left) a plane containing three S atoms connected by two covalent bonds. Cross sections of the CP contributions through same plane (b) in a-left (c) in a-right. Isoline of zero pressure is added to all the cross sections.

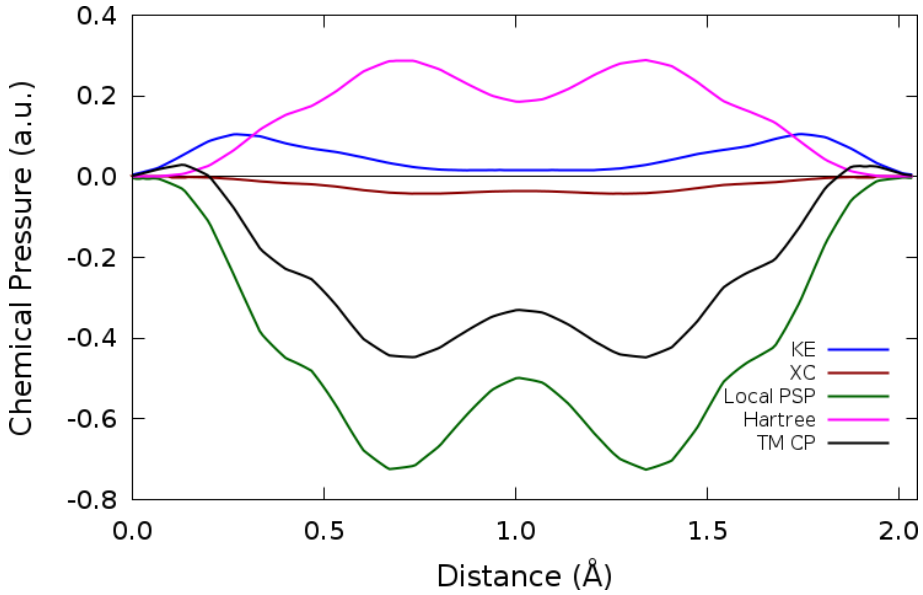

Figure 6.6: Chemical pressure contributions along two bonded S atoms in S_8 molecule.

6.2.2 Infinite 2D and 3D covalent lattices: Graphene & Diamond

Graphene was represented as a graphite unit cell with a long c-axis (10 Å) to avoid interlayer interactions.

In this part, we will discuss the CP features obtained in chapter 5 for these lattices built from only covalent bonds displaying two- and/or three-dimensional bonding networks. We will start with graphene. In Fig. 6.7a, we show a cross section of the total mapped CP map in which the in-plane C–C covalent bond is identified by a region of intense negative pressure (blue) and the nuclei are decorated by intense positive CP and separated by isoline of zero pressure from the background pressure. We have noticed that the positive pressure located at the hexagon centers of the graphene layer (See Fig. 5.6) disappear by ignoring the non-mapped contributions.

Figure 6.7b shows separate cross sections of the energetic contributions to the CP. KE and Hartree terms are positive over the entire unit cell while XC and local potential terms are negative. The maximum positive pressure is localed as usual at the nuclei. The hexagon centers of each graphene layer show negative total mapped CP which indicates a higher contribution from local potential and XC terms. The CP between the graphene layers is positive and changes to nearly zero. Besides, Figure 6.8 illustrates the interaction along the C–C bond. Here, again, the covalent bond appears as a deep double wells of negative pressure, with positive pressure at the nuclei. The positive pressure around the carbon cores arises from the kinetic energy term whereas the negative pressure along the bonding path is mainly due to the local potential. A sudden drop in the KE occurs on moving from the nuclei outward, since the highest electron localization is located near the nuclei.

Diamond has a three-dimensional crystal structure in which the carbon bonding involves sp^3 (tetrahedral) hybridization. In the unit cell, each six carbon atoms form a chair configuration. The total mapped CP map of diamond crystal is shown in Figure 6.9a. A cross section taken through [1 0 1] plane containing chains of bonded C atoms. The atomic positions are detected by intense positive pressure (red) which are embedded in a background of positive pressure. Regions of negative pressure are located between the C atoms and separated by isoline of zero pressure from the

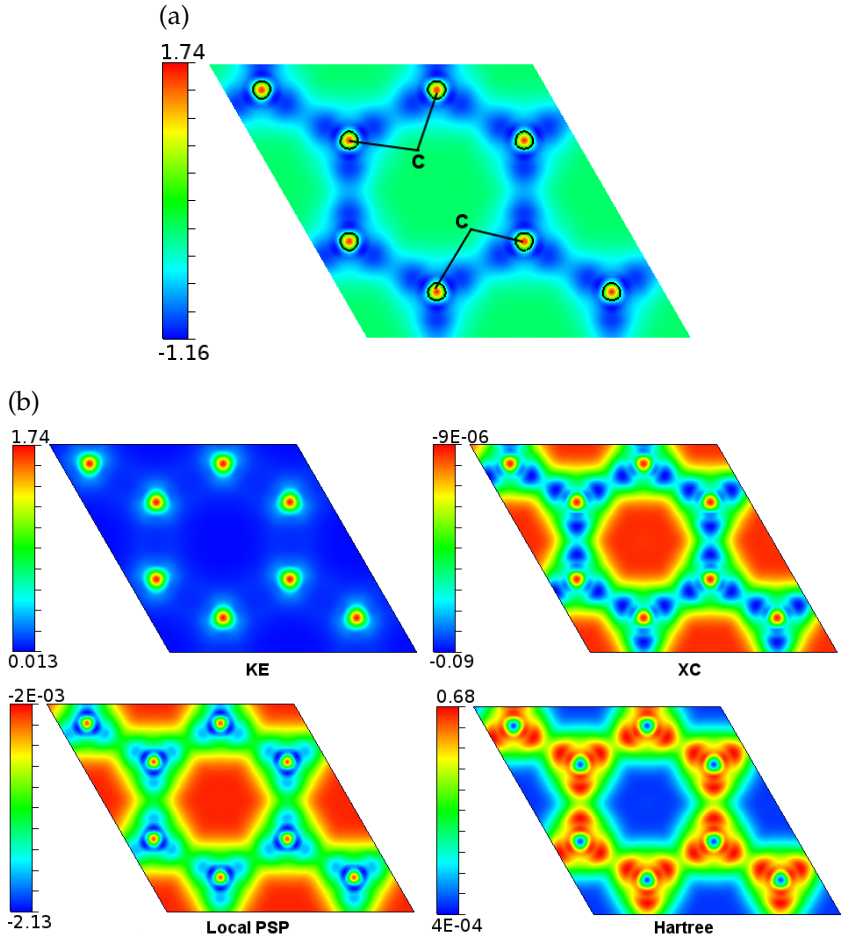

Figure 6.7: DFT–CP distributions calculated for isolated graphene (a) cross section of total mapped CP taken perpendicular to *c* (b) similar to the cross section of part a but for each energetic contribution. Black contours corresponding to CP=0.0 are overlaid on the map.

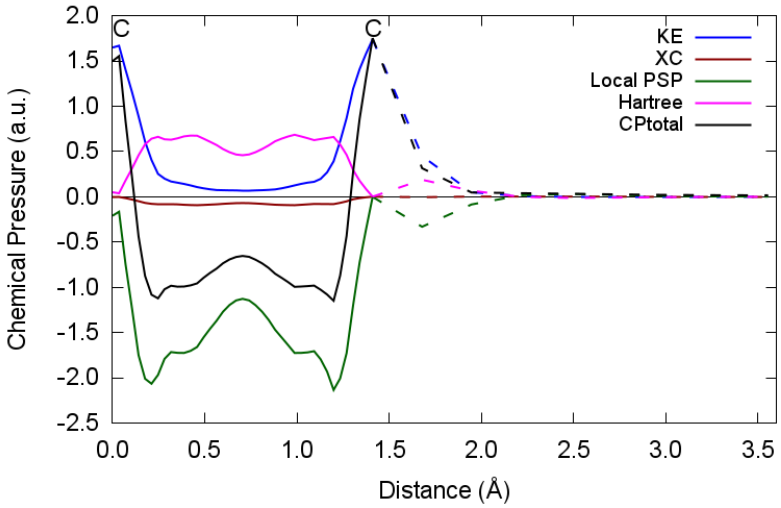

Figure 6.8: 1D profile of the chemical pressure contributions along the C–C bond path (solid) and perpendicular to graphene sheet (dashed).

background. The left panel of Figure 6.9a shows a background of mostly blue color, then we couldn't recognize the variation of CP along the bonding and interstitial spaces. In Figure 6.9a-right, We focus on the negative pressure features by rescaling the pressure range from -0.032 to 0.1 a.u., the most intense positive pressure is located around the atomic cores and lower positive pressure, close to zero, is located is the interstices. On the other hand, the negative pressure is accumulated directly between the C atoms and it appears as a region of three negative minima at the two bond ends and its center.

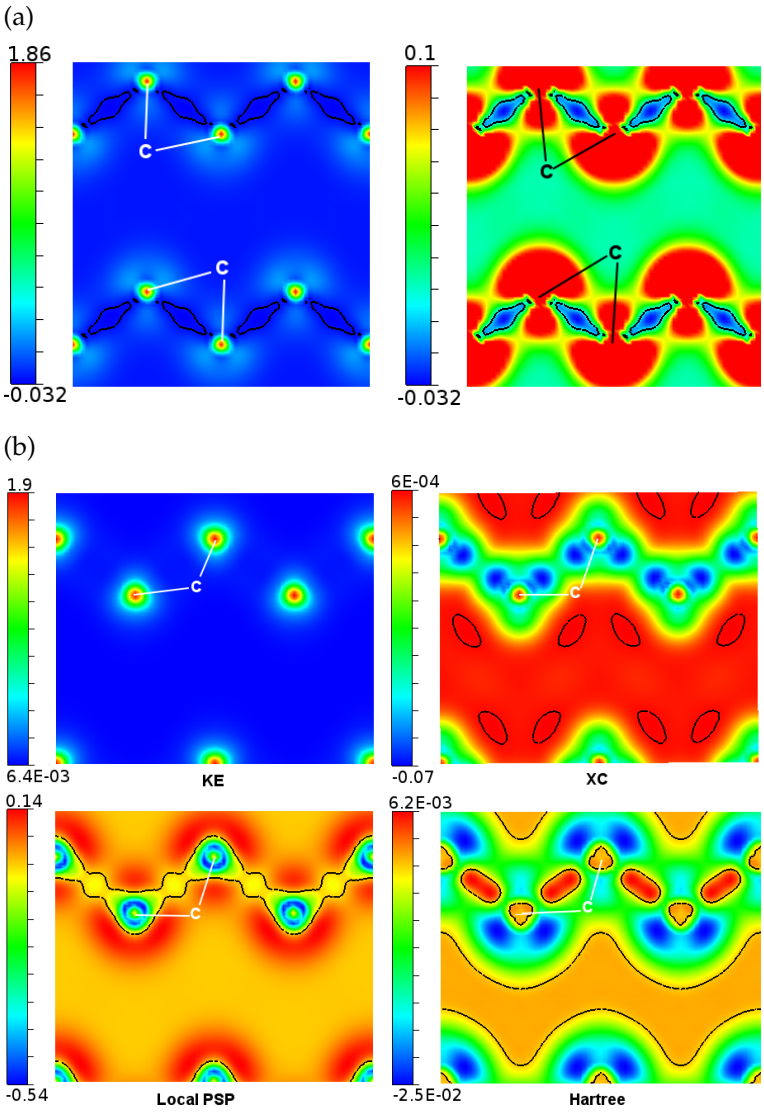

Figure 6.9: Cross-sections of chemical pressure of diamond. (a) Total mapped CP of [1 0 1] plane with pressure variation in the range of -0.032 to 0.100 a.u. and narrow range. (b) Mapped energy taken through a plane containing three C atoms connected by two bonds. Black contours corresponding to CP=0 are overlaid on the map.

For the first time we observed a CP minimum directly located at the bond center. The origin of this CP pattern can be discerned by separately analysing the CP contributions (Fig. 6.9b). KE is mostly positive everywhere in the crystal structure except

along the C–C bonding path which varies in a small negative CP scale. As usual, maximum of KE is located at the nuclei (red) and changes to a flatter region around the bond center. Hartree component is negative near the core while it becomes positive at the bond center and in the interstitial spaces which implies a more positive value as the cell contracts. Both XC and local potential components are negative functions along the bonding region. The local potential term has a third minimum, of lower negative CP value, at the bond center. The odd behavior of the local PSP and XC terms at the bond center can be related to the sp^3 hybridization of carbon atoms. In contrast to other systems, the XC term usually has a smaller negative CP range (very close to zero) than the local potential over the entire unit cell and also at each voxel. Figure 6.10 shows that around the bond center, the XC varies in a more negative CP range than the local component, and this results in a minimum of the TM CP at the bond center. The XC component is negative everywhere except some positive interstitial regions while the local potential is positive in the crystalline spaces.

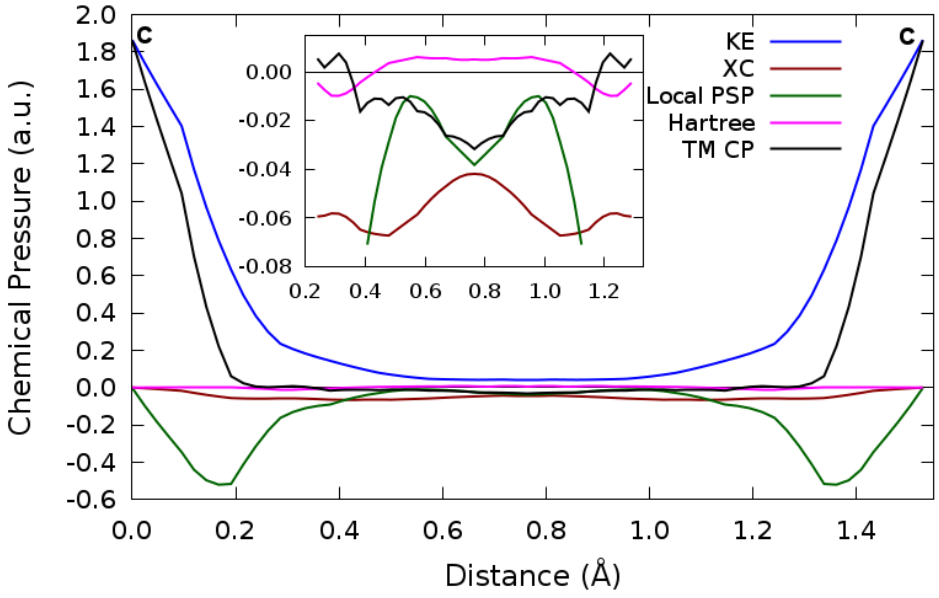

Figure 6.10: 1D profile of the chemical pressure contributions along the C–C bond path in diamond.

6.2.3 Crystals displaying both Intra- and Inter-molecular Interactions: Graphite, S_8 & CO_2

Moving to molecular crystal structures displaying non-covalent forces, such as van der Waals forces, offers the opportunity to recognize the differing behavior of the CP contributions of covalent and non-covalent interactions. In Figure 6.11a, we show a cross section through [0 0 1] plane calculated for the Bernal-stacked bilayer graphene, where half of the carbon atoms in the second layer sit on top of the empty centers of hexagons in the first layer. Each graphite layer displays two types of interaction: intralayer covalent C–C bond and interlayer weak van der Waals interactions produced by delocalized π-electron densities. The total mapped CP

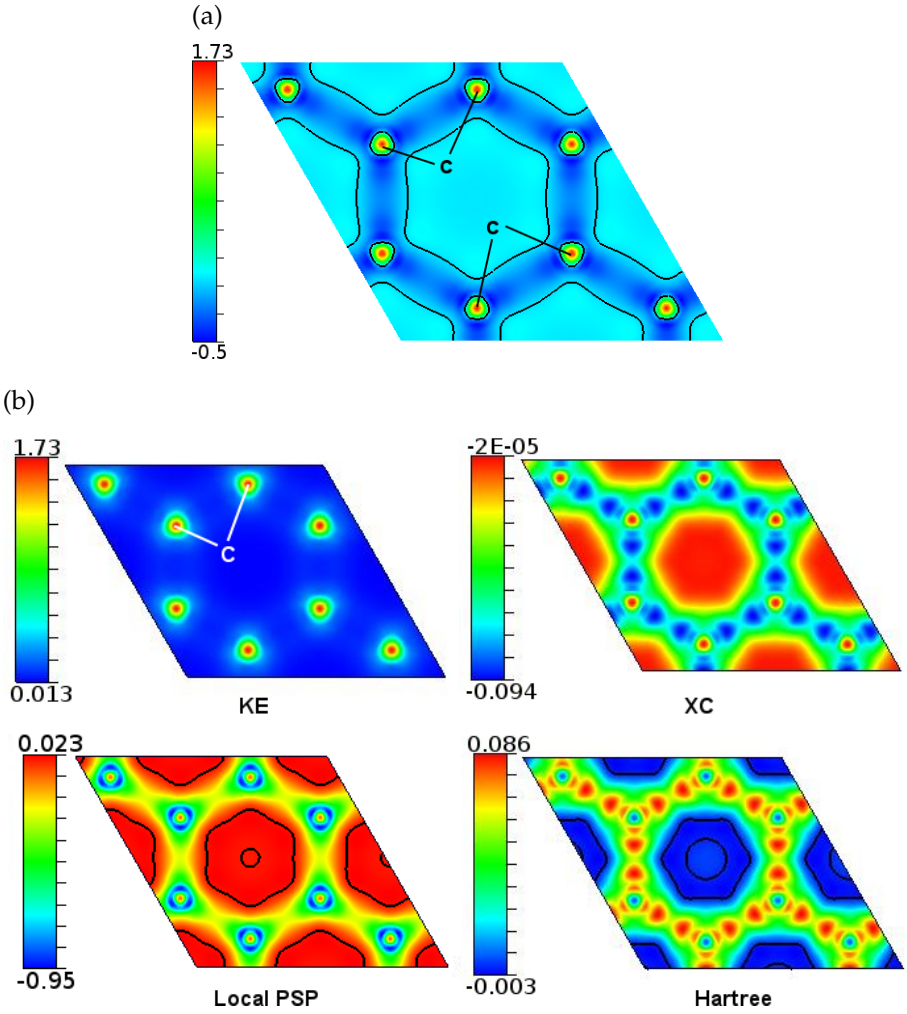

Figure 6.11: DFT-CP distributions calculated for graphite (a) cross section of total mapped CP in one layer (b) pure CP (without non–mapped terms) along two adjacent in– and out–plane C atoms (c) separate cross sections of each contribution to the mapped energy. Black contours corresponding to CP = 0 are overlaid on the map

map of a plane containing one layer displays negative pressure (blue) along the covalent C–C intralayer interactions with intense positive CP (red) at the nuclei. Accordingly, the covalent bond is characterized by two negative pressure ends with a lower negative at the bond center. The hexagonal pattern has an area of low positive pressure surrounded by isoline of zero pressure value.

We have noticed that the total mapped CP at the hexagon center changes from low negative to low positive on moving from isolated to molecular structure, respectively. This change can be associated with the weak interactions exist between the layers of graphite structure. Looking at the separate cross sections of the CP contributions of Figure 6.11b, again, the positive pressure located around the carbon cores is due to the KE term. The negative pressure located at the two ends of the C–C covalent bond arises from the local PSP term. In contrast to Figure 6.7b, the CP maps of KE and XC terms display similar features within same CP scale, whereas the local

and Hartree potentials vary in a wider CP range in case of graphene besides the existence of both negative and positive CP at the hexagon centers of graphite layers.

Figure 6.12 illustrates the two types of interaction between the carbon atoms, in-plane covalent bond (C1-C2) and out-plane weak van der Waals interactions (C2-C3). We can observe, again, a maximum positive KE located at the nuclei and a double deep wells of local potential is located very close to the core. While the opposing effects of Hartree and XC terms cancel each other out.

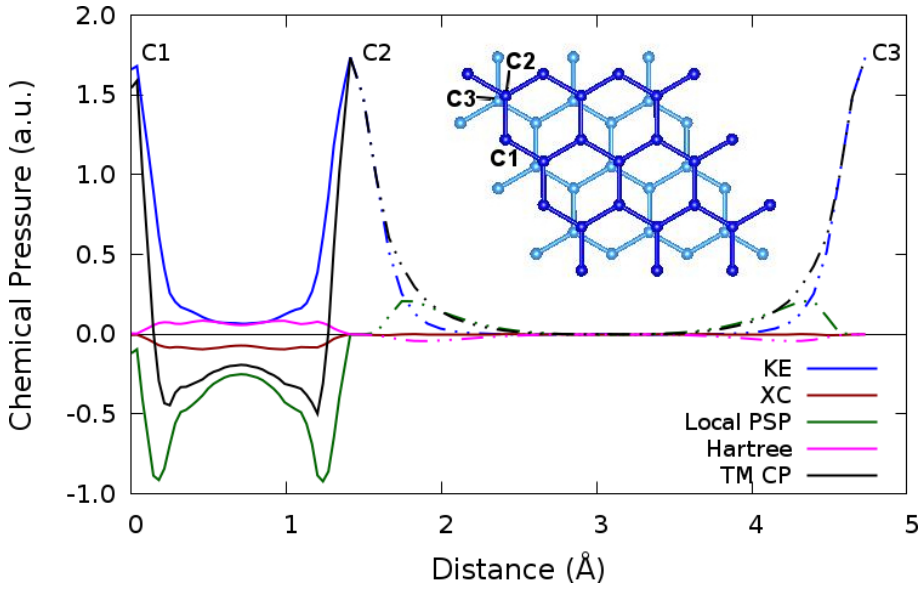

Figure 6.12: 1D profile of the chemical pressure contributions along in-plane covalent bond (C1–C2) and out- plane weak interactions (C2–C3) of graphite.

The weak interactions between the graphite layers, on the other hand, are characterized by nearly flat CP region and close to zero (See Figure 6.11b dashed line). The local potential shows a positive maxima of pressure with negative minima of Hartree near the carbon cores. Interestingly, This is the first time to see the local potential contribution varies in a positive CP scale. As seen in the previous systems, covalent bonds are always characterized by a negative local potential term. It seems to us that delocalized interactions will be also detected by positive value of local PSP term. This assumption will be more stressed through other crystals in the following sections.

Moving to the next system, molecular crystal of S_8, we will discuss the contributions to the CP and to be compared with the results discussed for the isolated molecule. Figure 6.13 shows cross section of the total mapped CP through a plane containing three consecutive atoms connected by two covalent bonds.

The CP map is characterized by regions of negative pressure surrounded by isolines of zero pressure value and a background of positive pressure in which the atoms are embedded. The regions of negative pressure (blue) are associated with the S–S covalent bonds and the lone pairs of sulfur atom. Overall, this picture was seen before in the isolated molecule (See Fig. 6.5), but some differences could be obtained between the two figures. First, the covalent bond in the isolated molecule is identified by more intense negative pressure (CP $\approx$ -0.45 a.u.). Second, the lone pair of electrons of sulfur atom is embedded in a negative pressure background(orange)

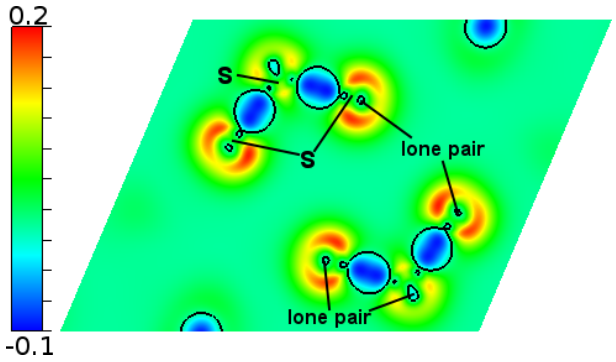

Figure 6.13: Cross-section of chemical pressure of molecular S_8 crystal through a plane containing three sulfur atoms bonded by two covalent bonds.

in the isolated molecule whereas they are surrounded by intense positive pressure (yellow) in the molecular structure. Another point is that the whole molecule is surrounded by a zero pressure isoline in the isolated structure separating the S_8 ring from the positive pressure background. We assume that this different environment around the S_8 molecule in isolated and molecular arrangement due to the weak van der Waals forces between the S_8 rings in the molecular structure.

We have noticed that the stacking between the S_8 rings is nearly similar to that between graphene layers in graphite structure. Projection along *c*-axis of the S_8 rings is shown in Fig. 6.14 in which the S_8 rings appear to have ABA stacking-type in which one-quarter of the S_8 atoms (red/blue) in one ring sit on top of the empty space of octagones below/above it. The CP at the S_8 ring center and in interstitial spaces is nearly zero and it changes to negative pressure ($\approx$ -0.02 a.u.) by adding the non-mapped energy, this seen in graphite/graphene pair. These CP features are assumed, again, due to the weak interactions between the S_8 rings in the molecular structure.

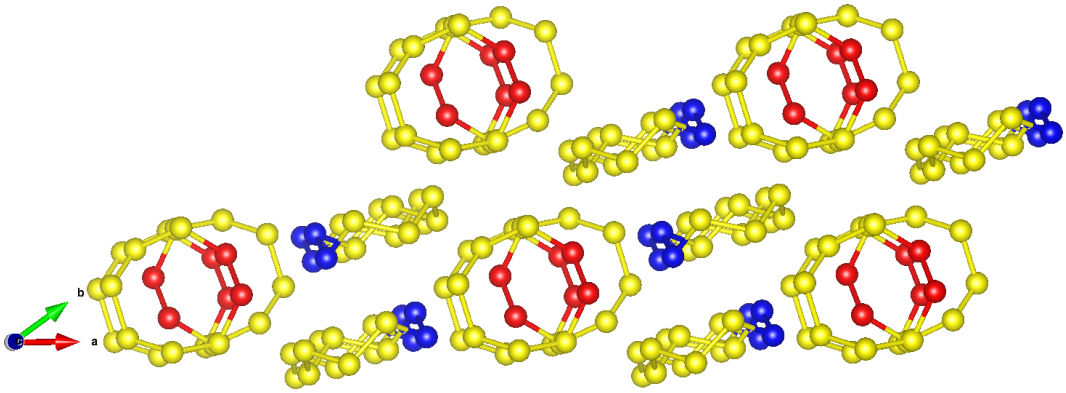

Figure 6.14: Stacking of the S_8 units in the molecular crystal. Projection along *c*-axis.

Regarding the partition into contributions, we can observe, again, that KE and Hartree terms are positive whereas local potential and XC terms are negative along the covalent bonding path (see Fig. 6.15 a). The psuedopotential of sulfur contains six electrons in the valence region, $3s^2\ 3p^4$, then each sulfur atom has two lone pairs of electrons. The lone pair of electrons of each sulfur atom can be identified as a negative region of CP close to the nuclei. Hartree pressure is more positive

as the cell contracts which indicates the repulsion between the bonding electrons. However, the local potential is non- positive function along the S–S bond that implies it becomes more negative as the cell contracts due to stronger interactions between the bonding electrons with both nuclei, then the overlap between the potentials increases.

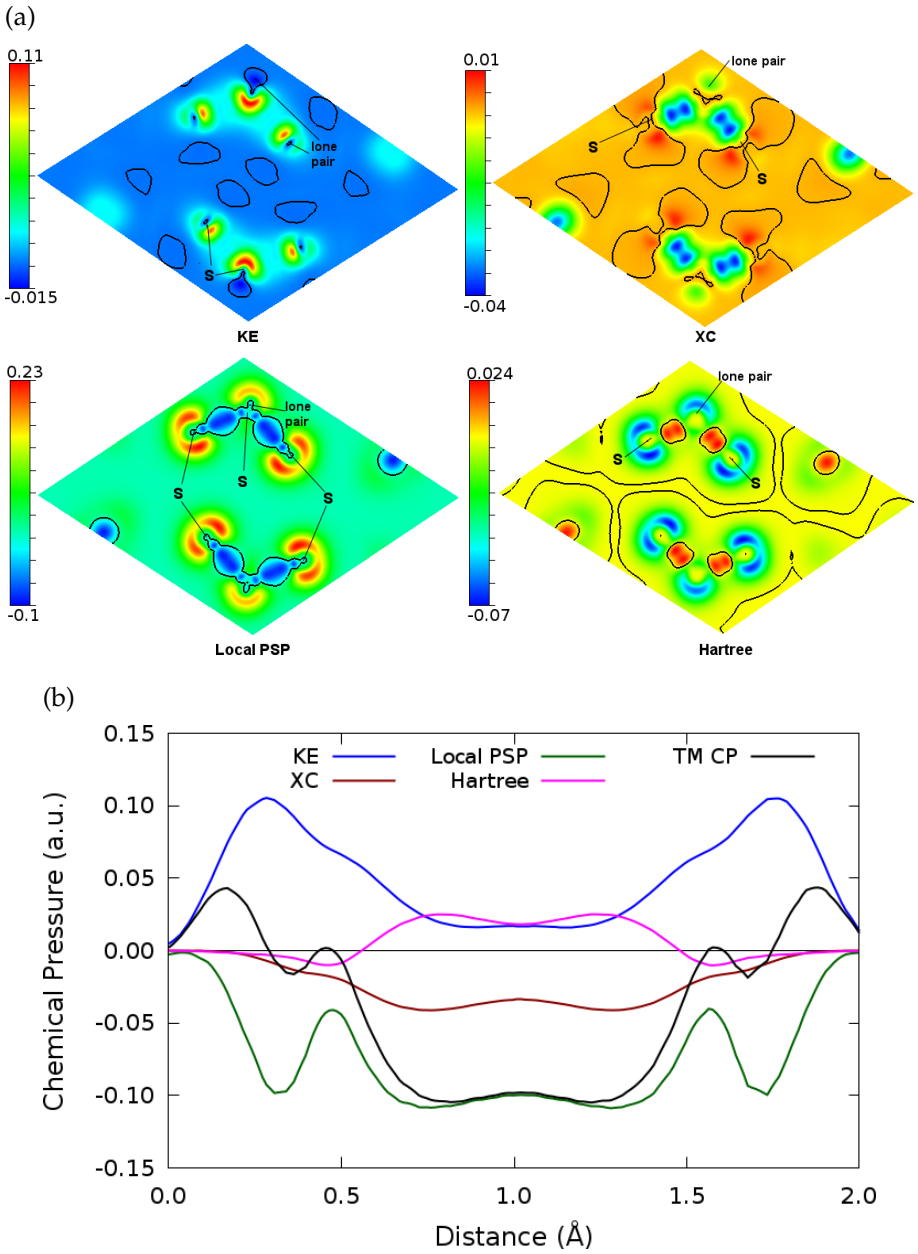

Figure 6.15: Chemical pressure contributions of molecular crystal of S_8. (a) Cross sections through a plane containing three nuclei of each S_8 unit for the major contributions to CP. (b) 1D plot of the CP contributions along the covalent S–S bonding path. Black contours corresponding to CP=0 are overlaid on the map.

The relative scales of these interactions are more clearly illustrated in a 1D profile of the CP function along the S–S path (See Fig. 6.15b). The CP varies in a flatter region around the bonding center due to the lowering CP range of both local poten-

tial and Hartree terms. As seen in graphite/graphene pair, in the isolated structure (Fig. 6.5a), local and Hartree terms display a wider CP range.

Now, we move to another molecular structure, the linear CO_2 structure. Figure 6.16 shows total mapped CP distributions of a plane containing four CO_2 molecules, plane $[1\,\bar{1}\,0]$. As seen in solid S_8, the total mapped CP map is characterized by a green background whose color corresponds to positive pressure near to zero. The negative pressure is accumulated in regions associated with the covalent bonding and the lone pairs of oxygen atoms. We focus only on the pressure range from -0.8 to 2 a.u. (right panel), the covalent bonds and the lone pairs of electrons now appear in dark blue color which corresponds to intense negative pressure.

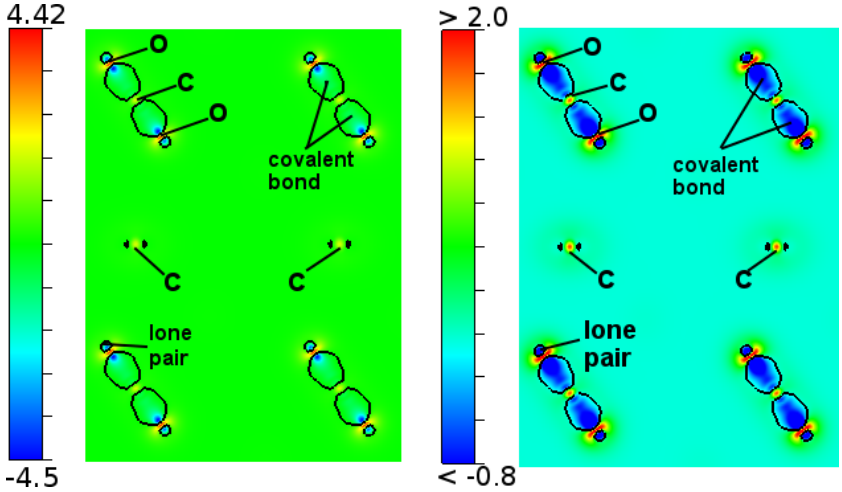

Figure 6.16: Cross-sections of chemical pressure calculated for molecular CO_2 crystal through $[1\,\bar{1}\,0]$ plane.

The partition into CP contributions are shown in Figure 6.17a. We can observe, again, that the positive pressure around the nuclei arises from the KE contribution whereas the negative pressure along the bonding path and in the interstices due to the Local PSP term. There are shoulders of positive pressure due to local PSP term with negative Hartree contribution situated toward the outside of each well near the two ends of the CO_2 molecule. These features were seen between graphite layers and also in molecular S_8 crystals. These features could be associated with the weak intermolecular interactions in the molecular structures.

These interactions are more clearly illustrated in the 1D profile of the CP along the bonding path (See Fig. 6.17b). Overall, the CP distributions in both isolated and molecular CO_2 are very similar. One important difference that could be related to the weak interactions in the molecular crystal is the positive pressure of the local PSP term which is not shown in the isolated structure. The total mapped CP is more negative in the isolated structure. The KE pressure dominates at the nuclei. Hartree and XC contributions are opposing and cancel each other out along the bond path. Hence, the TM CP is determined by local PSP and KE terms.

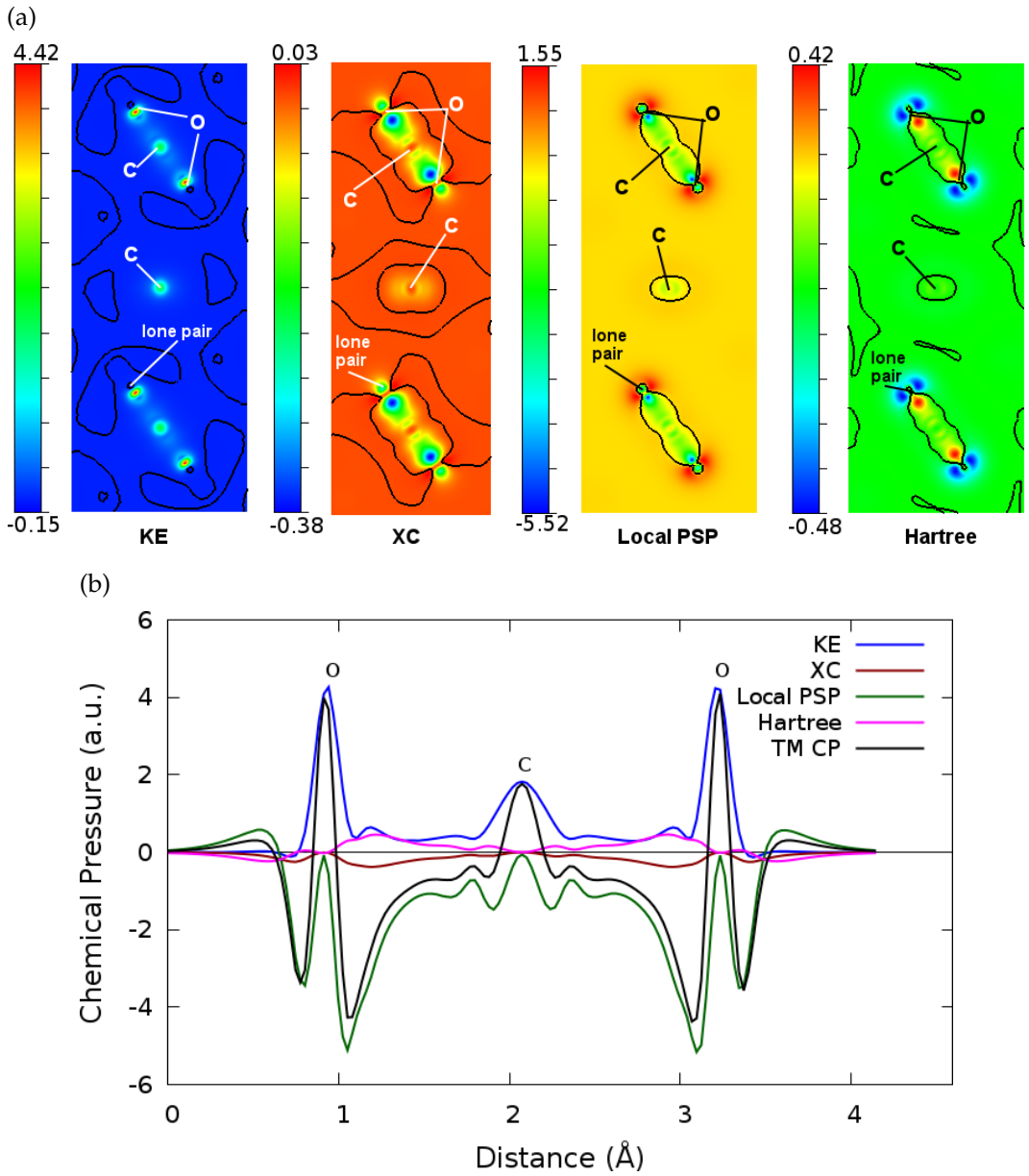

Figure 6.17: Decomposition of the CP distribution of solid CO_2 into contributions. (a) Cross sections of CP contributions through $[1\,\bar{1}\,0]$ plane with black contours drawn for CP = 0 to indicate transitions between negative and positive CP values. (b) 1D plot of CP contributions along the O–C–O bond path in molecular CO_2 crystal.

6.2.4 Chemical pressure contributions in hydrogen bond: Ice-I_h

Let's turn to explore the CP contributions in another type of weak interactions, the hydrogen bond, in the ice-I_h phase. We have shown in the previous chapter that the CP formalism can detect and identify localized and delocalized interactions in ice-I_h (Fig. 5.13a). Here, we will discuss in more details the source of these CP features and how it could be used to differentiate between covalent and non-covalent bond. In Figure 6.18a, we show a cross section of the total mapped CP distribution in the ice-I_h phase. The H atom is embedded in a negative pressure region (blue)

whereas O nucleus is detected by intense positive pressure (red). Every H_2O unit is separated by an isoline of zero pressure from a positive background. The hydrogen bond consists of two opposite pressure regions on moving from H nucleus, negative and positive pressure.

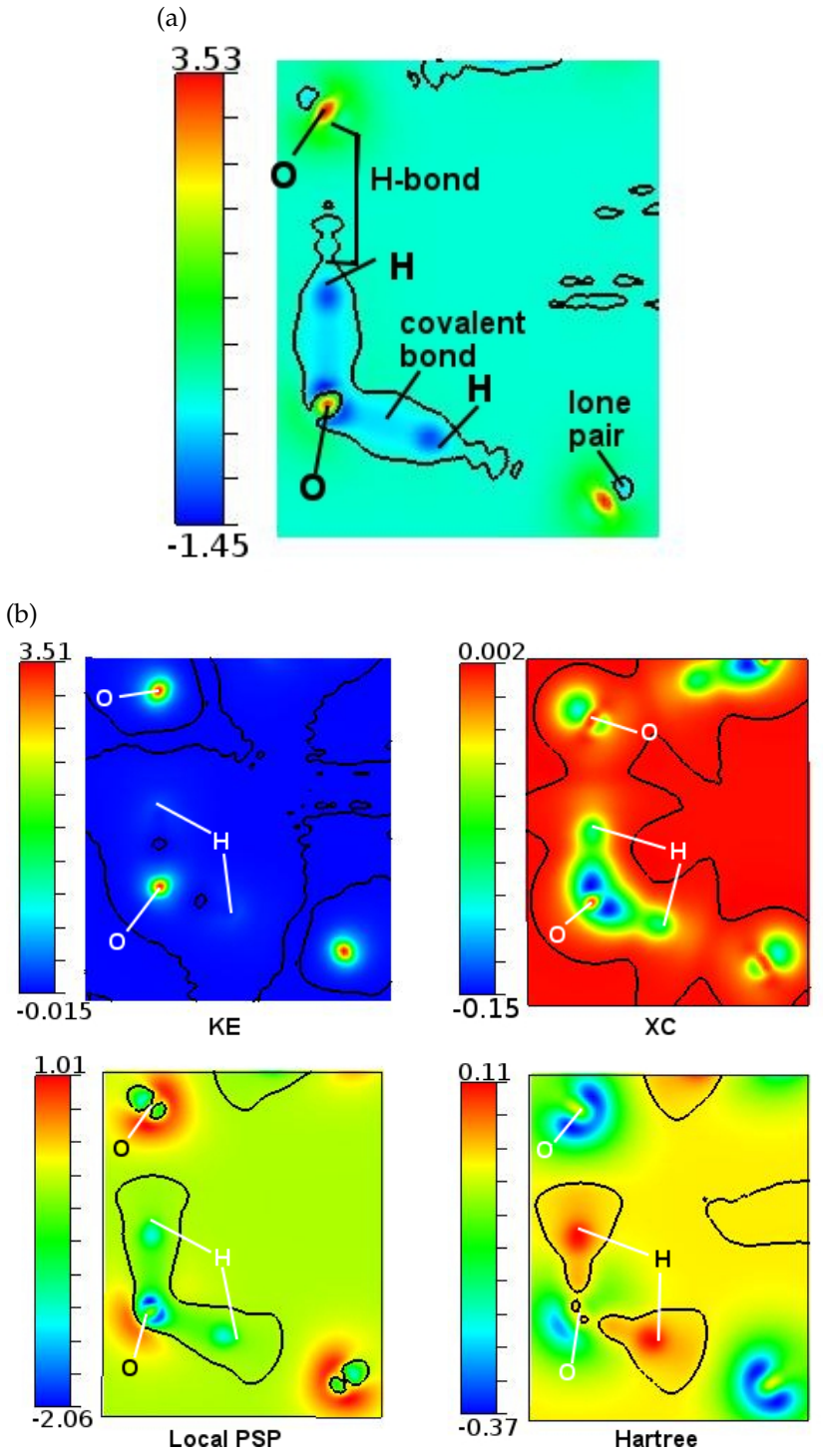

Figure 6.18: DFT-CP distributions calculated for ice-I_h. (a) Cross section of TM CP distribution through $[1\,\bar{1}\,0]$ plane at distance zero from origin. (b) Decomposition the CP distribution into its major contributions.

As regards the partition into contributions shown in Fig. 6.18b, it is clear that the KE map shows that intense positive pressure is located at the oxygen nucleus whereas it drops suddenly, nearly to zero, in the nucleus of hydrogen atom. The XC term is almost negative over the entire unit cell except in the regions between the chains of water units, it is flat and close to zero value. The local potential contribution is negative a long the covalent H–O bond and gradually decreases to zero at the middle of the hydrogen bond. Hartree map displays the opposite behavior of the local PSP contribution in which covalent interactions are characterized by positive pressure whereas hydrogen bond with negative pressure.

The relative scales of these interactions are more clearly illustrated in a 1D profile of the CP function along a O–H$\cdots$O path (Fig. **??**). In the oxygen side of the hydrogen bond there is a shoulder of positive pressure due to the local term with negative Hartree contribution compensated with the increasing positive kinetic core part. This distribution was seen in previous systems displaying weak intermolecular interactions (See Figs. 6.12, 6.17b).

6.2.5 Partition of chemical pressure in crystals displaying metallic bonding: Na, As, Sb & Bi

In this section, we will turn to another type of chemical bond, the metallic bond. We will show here the partition of the CP distributions of some simple metallic compounds such as Na, As, Sb and Bi crystal structures into its main major contributions. It is well known that atoms are held together by metallic bond within a sea of delocalized electrons in metallic crystals.

Using the semi-core PSP for Na which contains 9 active electrons in the valence region.

Let's start with the sodium in *bcc* structure. According to the free electron model, the valence electron density in a crystal structure of a metallic solid is obtained from the ideal gas in which electron-electron interactions are completely neglected. This could be seen as a CP plateau in the interstitial spaces between the Na cores. This behavior is seen also in the contributions as shown in Fig. 6.19a. We can observe that the intense CP features are accumulated near the nuclei (See Fig. 6.19b). The positive pressure around the sodium cores arises from the local PSP term whereas the negative pressure is due to the Hartree contribution.

Interestingly, we see now a new trend of the CP contributions for the metallic bond which differs from the covalent bond trend, but at the same time, it is analogue to the contributions trend of weak interactions, as seen in graphite and ice-I_h. The total mapped CP is positive around the Na–Na path due to local potential and kinetic energy terms (See Fig. 6.19b).

This pressure becomes negative when adding the non-mapped pressure to the background as shown in Fig. 5.14

We have also studied the metallicity in some selected elements of the group 15 of the periodic table, such as As, Sb, and Bi. In the previous chapter, we have discussed how the CP formalism can be used as a tool to identify and calculate an index for metallicity in solid crystals (See eq. 5.1–5.3). Here, we will discuss the partition of CP distributions into contributions to understand the source of these features. Overall, the positive CP features around the nuclei arise mainly from the local PSP contribution along with the KE term and compensated by negative Hartree contribution. The total KE pressure contribution decreases on moving to Bi. This can be understood as an indication to the increasing delocalization of electrons, Ruedenberg's point of view. In view of the 1D profiles along the nearest neighbor

KE pressure in As is 0.00352283 *a.u.* = 103.645 *GPa*

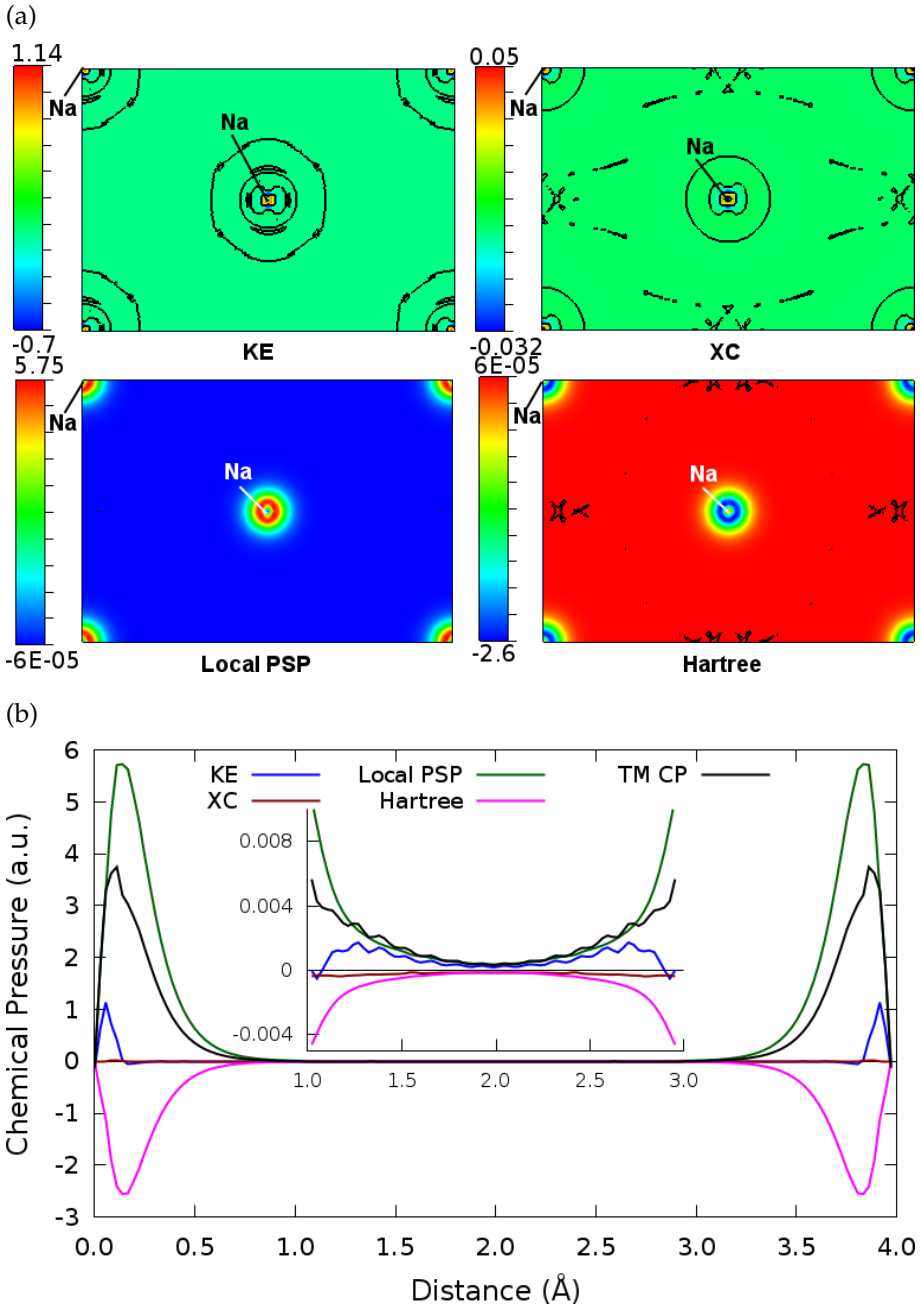

Figure 6.19: DFT-CP results of metallic *bcc*-Na structure. (a) Partition of CP into its major contributions through $[1\,0\,\bar{1}]$ at $z = 0$ with black isolines corresponding to CP=0. (b) 1D plot of the CP of contributions along the two closest Na atoms path.

path (See panels b in Figs. 6.20–6.22), the KE contribution decreases around the nuclei, but, at the same time, it increases at the center to a positive value in Bi. This is accompanied by a decrease in the local PSP term due to stronger interactions as the cell is contracted.

Moreover, The nuclei are decorated by negative pressure of Hartree contributions with a very small positive value located between the nearest atoms. XC, on the other hand, is non-positive function over the entire unit cell of As and Bi, while it exhibits positive regions around the nucleus of Sb. Interestingly, KE maps of Sb and

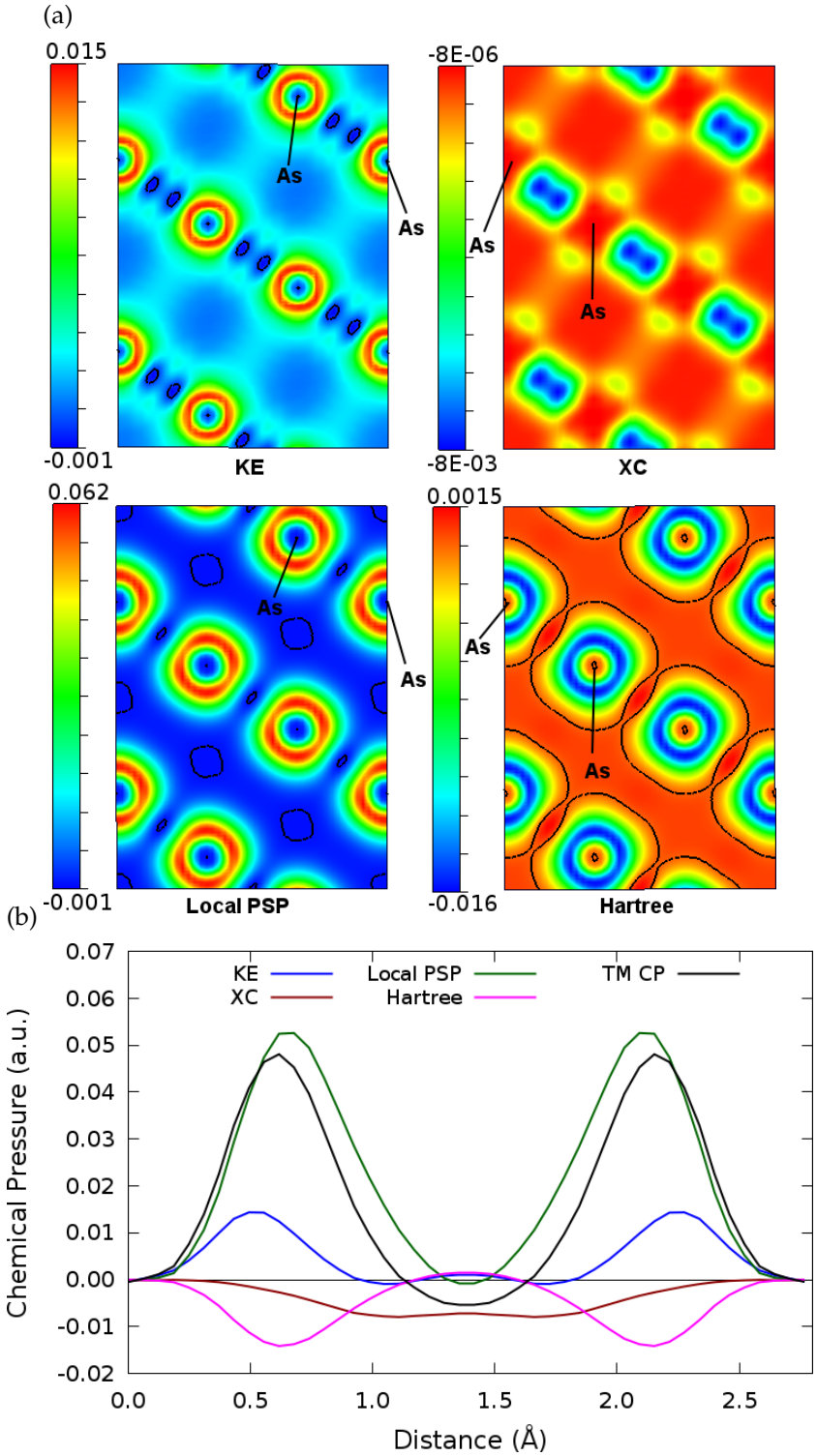

Figure 6.20: (a) Cross sections of the CP contributions through the [1 1 0] plane calculated for As crystal. (b) 1D plot of the CP contributions along the nearest neighbor path.

Bi show that the outermost shell surrounding the nuclei in red are distorted into an egg shape. This occurs against the negative pressure in the bonding region as seen in cross sections of KE (Fig. 6.20–6.22).

The trend of the local pseudopotential and Hartree terms along the metallic atoms was seen before in crystals display weak intermolecular interactions. It seems to us that the change of the local potential from non-positive function to positive one in the metallic solids is because of the delocalization of the valence electrons and then the weak attraction of these electrons with the nuclei.

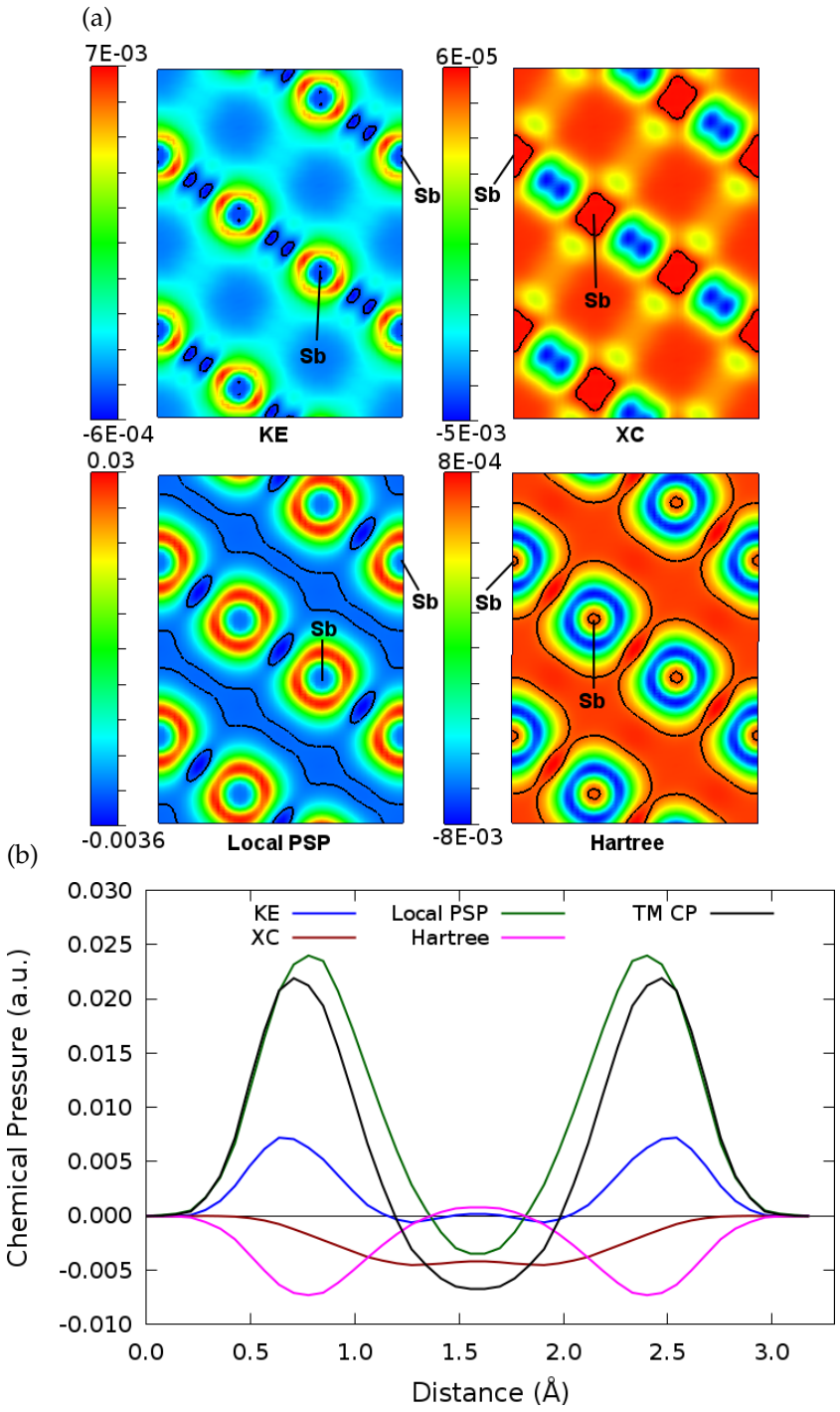

Figure 6.21: (a) Cross sections of the CP contributions through the [1 1 0] plane calculated for Sb crystal. (b) 1D plot of the CP contributions along the nearest neighbor path.

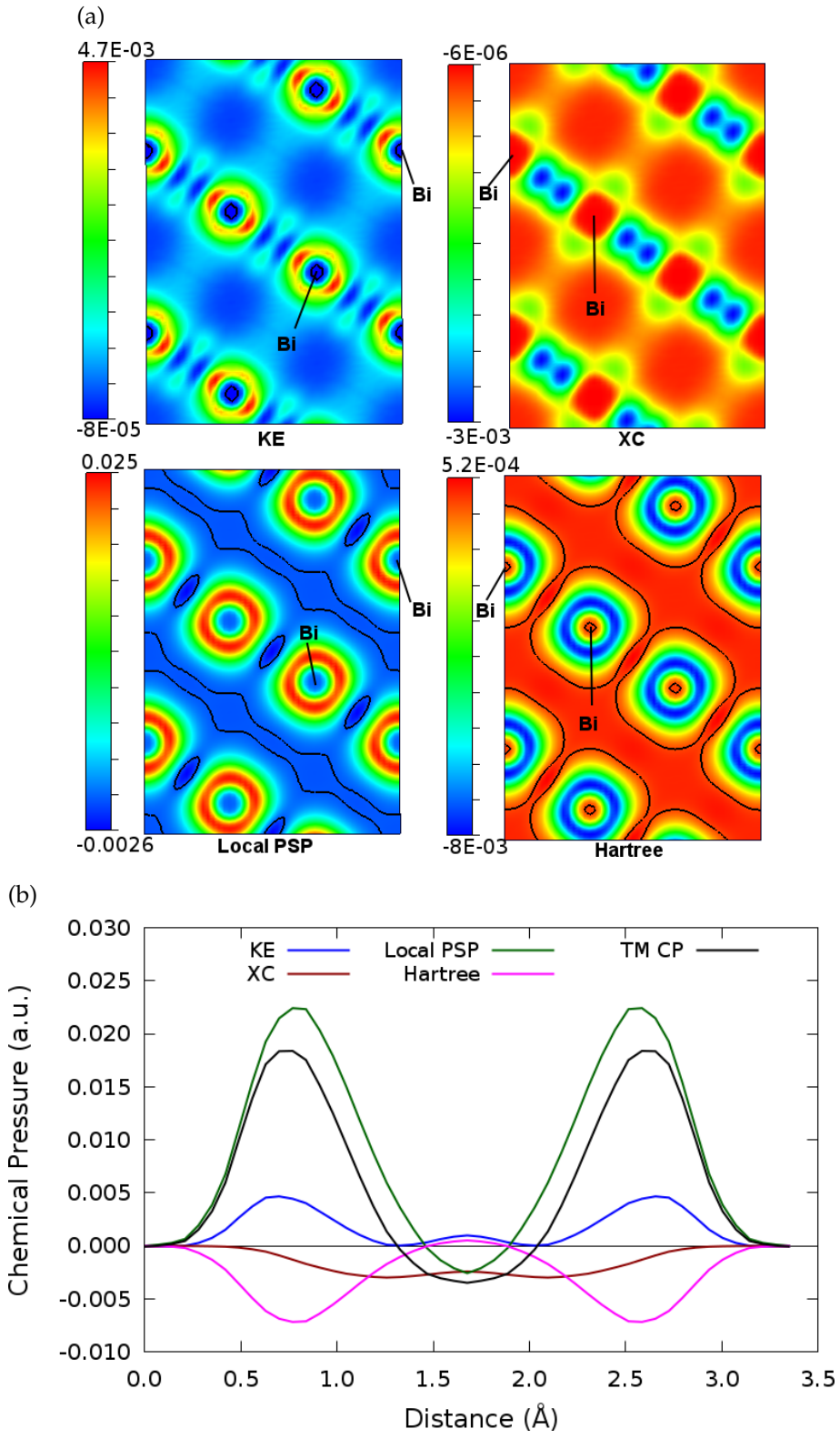

Figure 6.22: (a) Cross sections of the CP contributions through the [1 1 0] plane calculated for Bi crystal. (b) 1D plot of the CP contributions along the nearest neighbor path.

6.2.6 Chemical pressure contributions in crystals displaying ionic bonding: NaCl

Now, we will go over another type of bonding, the ionic bond. Here, we show the DFT-CP analysis of in the ionic crystals of NaCl. The semi-core pseudopotentials of metals are available at the ABINIT website. We will also discuss the effect of using such high number of electrons in the valence region on the CP features. In Fig. 6.23a and b, we show the total mapped CP distributions of the B1-phase of NaCl applying the valence-only (VO) and semi-core (SC) versions of the atomic pseudopotentials of Na which contain respectively 1 and 9 electrons in the active valence region.

http://www.abinit.org/downloads/psp-links/psp-links/hgh

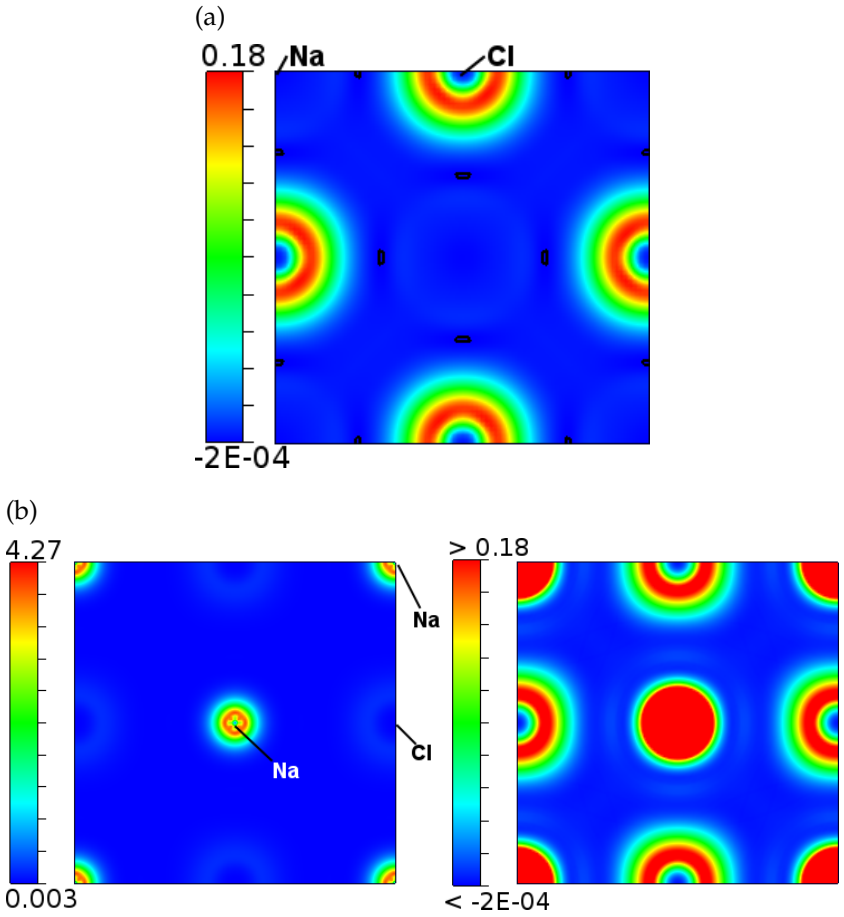

Figure 6.23: Cross sections of the total mapped CP distributions of NaCl taken perpendicular to c-axis at $z = 0$ using (a) valence-only (VO) and (b) semi-core pseudopotential of Na. In part b-right, we focus on the range -2×10^{-4} to 0.18.

In the resulting CP map of using the VO pseudopotential, we can observe that the region surrounding the sodium atom is very flat and of negative pressure, nearly zero, whereas the chloride cores are decorated with spherical shells that change in color from blue (negative) to red (positive) and back to blue on moving from the nuclei outward. On the other hand, turning to the SC pseudopotential, the CP features changes to more intense positive pressure. These intense positive pressures (red) can be associated to the semi-core active $2s^2$ $2p^6$ electrons of sodium atom. These core-like features change the maximum positive pressure from 0.18 to 4.27 a.u. in VO and SC, respectively. The CP features around the chloride cores are still

same seen in the VO CP map. This could be shown by focusing only on the pressure range -2 $\times$ 10^{-4} to 0.18, the CP scale of the VO CP map, as shown Fig. 6.23b-right.

Let's now examine the source of these CP features through the mapped energetic contributions (See Figure 6.24a and b). We noticed that the local potential is a non-negative function over mostly the entire unit cell in contrast to negative behavior in the previous mentioned systems.

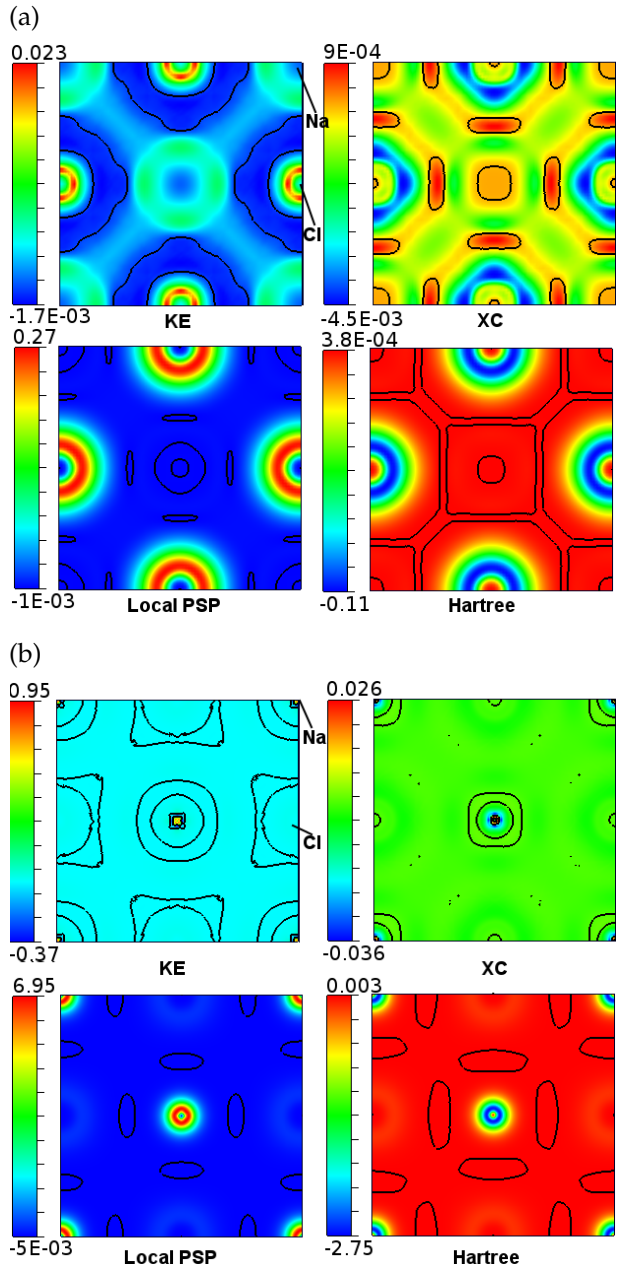

Figure 6.24: Cross sections of energetic contributions to the mapped DFT-CP calculated for NaCl (a) valence–only (VO) (b) semicore pseudopotential of Na.

The most intense positive features (red) are localized near the nuclei of Cl, that is when VO results. However, this changes in using semicore pseudopotential of Na, a higher positive CP localizes around Na. In any case, local potential term is the most positive contribution to the total mapped CP (TM CP) while Hartree share

with a greater extent in the negative part. Actually, we are interested in the negative CP region associated with bonding, so we analyze the variation of CP contributions along the Na–Cl bond (see Figure 6.25a-b).

(a)

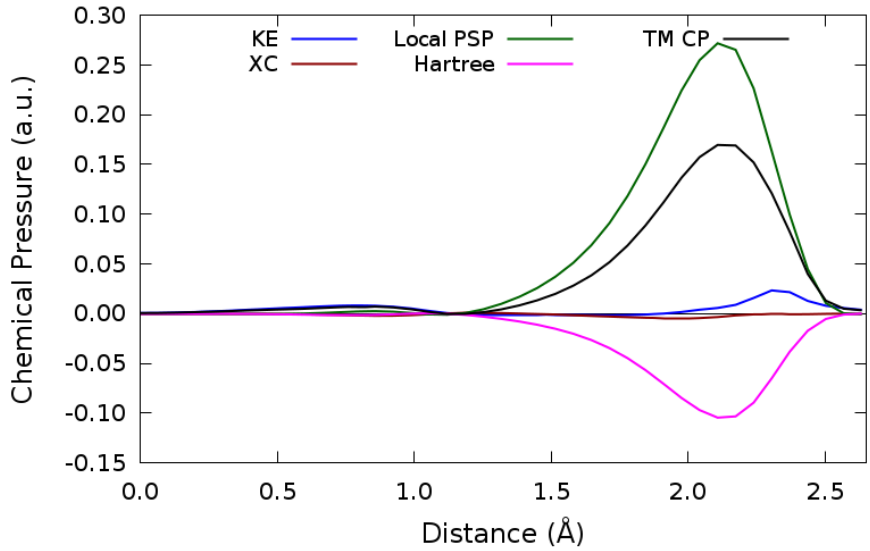

(b)

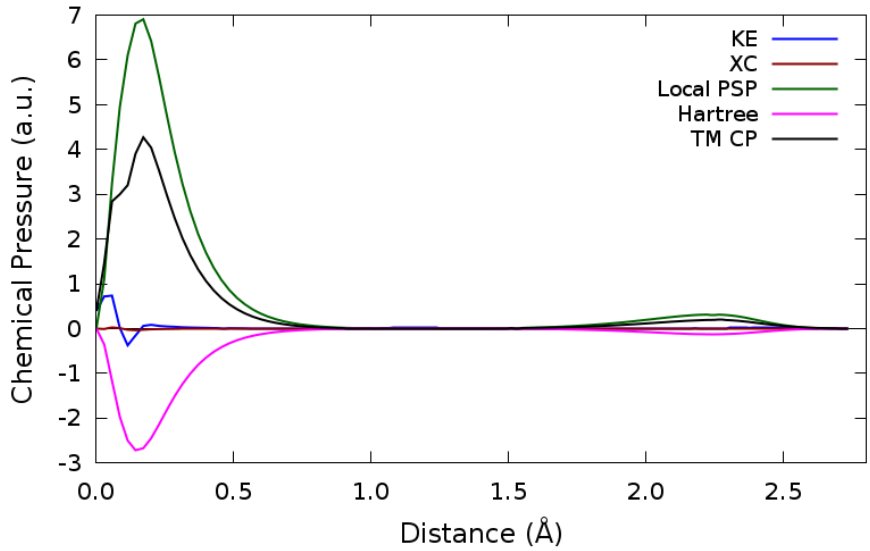

Figure 6.25: 1D profiles of chemical pressure distribution along the Na–Cl bond (a) valence–only (VO) (b) semicore pseudopotential of Na.

Part V

Chemical Pressure & Anions In Metallic Matrices Model

7 CHEMICAL PRESSURE IN METALLIC MATRICES

CONTENTS

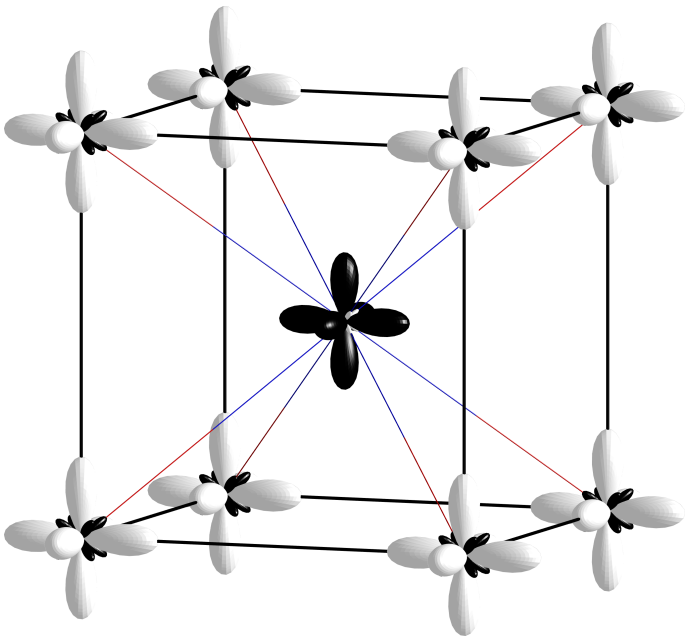

DFT-Chemical Pressure associated with the atoms in perovskite-type BaSn. Black anisotropic lobes of negative chemical pressure around Sn atom pointing to the centers of the cube faces suggest the positions for the enhancement of the cohesion of this metal alloy. The white lobes of positive pressure pointing between Ba–Ba contacts indicate the difficulty to reduce the volume of the BaSn unit cell along these directions.

The crystal structure of an inorganic compound consists of a metallic matrix playing the role of a host lattice in which the nonmetallic atomic constituents are located, the Anions in Metallic Matrices (AMM) model stated. Actual positions of these guest atoms can be microscopically interpreted in terms of the topological features of the electron density of the metallic sub-lattice. Besides the electron density, the electron localization function (ELF) has also provided successful support to the AMM model in a variety of examples. A particular interesting case is the one of the Ca *fcc* (face centered cubic) and *sc* (simple cubic) phases that show ELF attractors at the same positions where oxygen nuclei are located, respectively, in the rock salt (B1) and cesium chloride (B2) phases of CaO. Similar results were also observed for the pairs Ca/CaF_2 and $BaSn/BaSnO_3$. Interestingly enough, we will illustrate in this chapter how the DFT-Chemical Pressure (DFT-CP) approach provides a straightforward interpretation of these findings. Our results display similarities with the ELF plots but using the energetic perspective of the CP approach. From the analysis of different geometries for the metallic structure, CP maps are able to reveal a correspondence between negative (attractive) pressure regions and the positions of the anions in different inorganic compounds containing the same metallic sub-lattice. In this way, the CP map of a Ca-*fcc* structure with the same dimensions of the CaO-B1 phase is seen to show minima (equivalent to ELF-attractors) of negative pressure at the atomic positions of oxygen in the CaO-B1 phase. The same has obtained in the case of Ca-*sc* when the dimensions of the CaO-B2 phase are used. Moreover, the CP analysis in a high pressure phase of BaSn (with the same structure as in the $BaSnO_3$ perovskite) shows *attractors* of negative pressure at the O-atom positions occupied in the perovskite structure, thus showing an octahedral-like isosurface of negative chemical presure around each Sn-atom. Other examples involving *fcc*-Na and the associated B1 phases of different sodium halides will be also discussed in this chapter.

7.1 INTRODUCTION

The literature on the theories and formalisms describing chemical bonding in inorganic crystal structures is very extensive. There are many contributions that can be classified into either classical or quantum models. The approach of Pauling has been the paradigm for predicting and rationalizing the crystal structures of ionic compounds in the last century [93, 95]. The limitations of the ionic model, which have led to a number of misconceptions about the crystal structure and the bonding network, were discussed by O'Keeffe & Hyde [88] using an alternative approach. These authors put the emphasis on a description of the crystalline structure based on considering the anions into a packed cation array. Interestingly enough, von Schnering *et al.* [124] introduced the term *electride* after an extensive quantum mechanical treatment of a high pressure modification of cesium, and denoted this phase as Cs^+e^-. Thus, the emphasis was again on a negative charge, in this case the valence electron localized in the empty space of the structure that can be seen as acting as a pseudo-anion.

Besides, considering the metallic matrix of an inorganic compound as a host lattice for non-metallic atoms, the Anions in Metallic Matrices (AMM) model shows that

the electron density of this metallic sub-lattice induces the final positions of the non-metallic atoms in the crystal. This idea was a result of a number of studies that take into account not only a dense packing of atoms, as in metals and/or alloys, but also more open skeletons such as AlX_3 structures (X = F, Cl & OH) [123]. The AMM model found support from several theoretical calculations as those reported for PB (zincblende-type) [84] and for the high pressure phases of Na and K [76]. In these structures, the valence electrons of the metal are found to be localized in interstitial positions and, as in the work of von Schnering *et al.* [124], they are named as pseudoanions and the metal is called an *electride*. Moreover, and directly related with the study presented in this chapter, a more recent analysis of the electron localization function (ELF) of different elemental calcium phases, e.g. *fcc* and *sc*, at the volumes of the NaCl-type (B1) and CsCl-type (B2) structures of CaO, reveals the correspondence between the positions of the localized electron density in the interstitial positions of the metal and the positions of the oxygen atoms in the two structures of CaO. Among other examples that include the couples BaSn/$BaSnO_3$ and Na/NaX (X: F, Cl, Br), these crystals will be the focus of a study in this chapter using the CP formalism.

7.2 STRUCTURAL AND COMPUTATIONAL DETAILS

At zero pressure, two phases of solid calcium are known. The low-temperature phase II has a fcc structure with a = 5.588 Å. The high-temperature phase I crystallizes in a *bcc* structure with a = 4.48 Å at 721 K [59]. The Clapeyron dP/dT slope for the II-I phase transition provides a transition pressure of 19.5 GPa at 300 K with a volume reduction of 2% and a = 3.559 Å at 26.6 GPa. By increasing pressure at the same temperature, a phase transition to a new phase III was observed at 32 GPa with a volume reduction of 8% [90]. This phase III crystallizes in a simple cubic structure with a = 2.615 Å at 39 GPa. This pressure induced phase transition was also confirmed in the range $31 - 35$ GPa and 300 K [90, 131]

Moreover, calcium oxide transforms from the B1 (NaCl-type) to the B2 (CsCl-type) structure in the range 60-70 GPa with a volume decrease of 11% [60]. Calcium oxide shows a unit cell parameters of 4.80 and 2.64 Å for B1 and B2 phase, respectively. The elemental calcium structures are preserved in the corresponding CaO phases. In the B1 and B2 phases, the calcium sub-lattice displays, respectively, the *fcc* and *sc* structures. However, a CaO phase with a *bcc*-Ca sub-lattice has not been reported yet.

Regarding the BaSn/$BaSnO_3$ pair, BaSn undergoes a transition from the CaSi- to CsCl-type structure at high pressure [5]. It is this high pressure phase of BaSn, with a primitive cubic unit cell and a lattice constant of 4.07 Å, the structure considered in our study. At ambient pressure, sodium adopts the (*bcc*) crystal structure. However, we have studied *fcc*-Na structure, since this is the sub-lattice of sodium atoms in the rock-salt phases of the sodium halides. In fact, the *fcc* structure in alkali halides has been found for example in potassium which transforms from the *bcc* crystal structure to *fcc* at 11 GPa [89].

The electronic structure calculations of all the compounds presented in this chapter were carried out following the same procedure described previously in chapter

Table 7.1: Computational parameters of CP calculations with `ABINIT`. Atomic units are used.

	no. of e	a (Å)	Space Group	E_{cutoff} (Ha)	k-point grid	FFT-grid
fcc-Ca	10	5.521	Fm-3m	120	$4 \times 4 \times 4$	$100 \times 100 \times 100$
sc-Ca	10	4.829	Pm-3m	100	$6 \times 6 \times 6$	$60 \times 60 \times 60$
BaSn	10 (Ba)–4 (Sn)	4.070	Pm-3m	80	$1 \times 1 \times 1$	$240 \times 240 \times 240$
B1-CaO	10 (Ca)–6 (O)	2.645	Fm-3m	300	$6 \times 6 \times 6$	$60 \times 60 \times 60$
B2-CaO	10 (Ca)–6 (O)	4.800	Pm-3m	170	$6 \times 6 \times 6$	$60 \times 60 \times 60$
$BaSnO_3$	10 (Ba)–4 (Sn)–6 (O)	4.07	Pm-3m	170	$5 \times 5 \times 5$	$90 \times 90 \times 90$
NaF	9 (Na)–7(Cl)	4.634	Fm-3m	350	$6 \times 6 \times 6$	$150 \times 150 \times 150$
NaCl	9 (Na)–7(Cl)	5.465	Fm-3m	350	$6 \times 6 \times 6$	$192 \times 192 \times 192$
NaBr	9 (Na)–7(Cl)	5.974	Fm-3m	350	$6 \times 6 \times 6$	$192 \times 192 \times 192$

3. All the calculations employed the semi-core pseudopotential when it is available. The number of valence electrons for the corresponding atoms are collected in Table 7.1 along with the main computational parameters.

See http://www.abinit.org/downloads/psp-links/psp-links/hgh

7.3 METALLIC SUB-LATTICES

7.3.1 *fcc*-Ca

The ELF was firstly computed for a *fcc*-Ca lattice with the experimental lattice parameter determined at ambient conditions (a = 5.521 Å). The results show localized pair electrons at the atomic positions of fluoride anions in CaF_2 fluorite. However, when the volume of the unit cell is reduced to the theoretical value of the B1 structure of CaO (a = 4.829 Å), ELF also shows attractors at the positions of the O atoms in the B1 phase of CaO (see Ref. [123]).

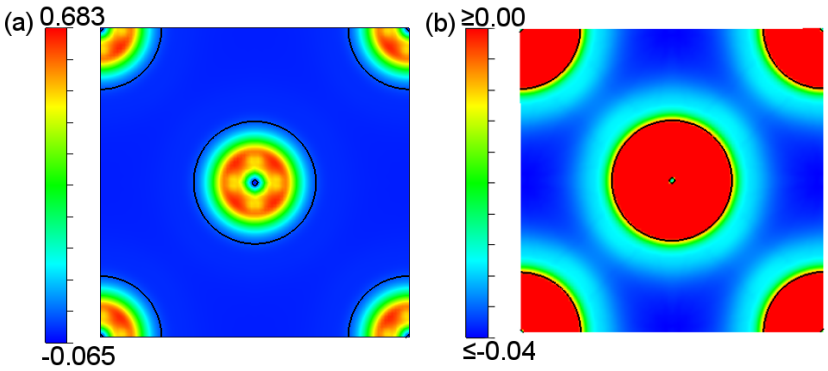

Figure 7.1: Chemical pressure analysis of *fcc*-Ca in the volume of CaO. (a) A [0 0 1] cross-section of the CP map and (b) the same map in (a) with CP range between 0.00 and -0.04 a.u..

In our study using the CP formalism, the raw data was obtained for each unit cell through the same electronic structure calculations as in the ELF case. The cross section of the CP map distribution for *fcc*-Ca in the volume of B1-CaO phase is displayed in Fig. 7.1 using two different scales. A similar picture was obtained at the equilibrium volume of *fcc*-Ca. The pressure value of each point in space is indicated by a color code depending on the scale. The total pressure range is from 0.683 to -0.065 a.u. (1 a.u. = 2.94219×10^4 GPa). Most of this pressure range is concentrated around the nuclei, the Ca has a spherical shell structure with color changing from blue (intense negative) to red (intense positive) and yellow (zero). This high variety of pressure values around the nuclei positions can be related to the semi-core $3s^2$ $3p^6$ electrons of the Ca atom. As displayed in the sub-figure using only a negative scale for the chemical pressure, the cores display an overall positive pressure that is gradually and radially decreasing as we depart from the nucleus. Once we arrive at a zero CP value then negative and more constant chemical pressure values surround the spherical CP positive values associated with the atomic positions.

In Fig. 7.2, we show 3D plots of the chemical pressure of *fcc*-Ca at its equilibrium lattice parameter using different values for the positive and negative CP isosurfaces.

The negative isosurfaces are exactly at the same positions as the ones obtained with the ELF.

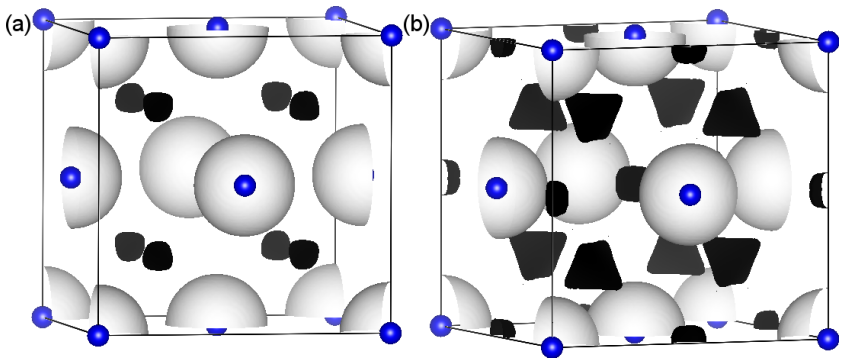

Figure 7.2: Chemical Pressure 3D isosurfaces of *fcc*-Ca lattice with isosurface value of (a) CP=±0.0278 and (b) CP=+0.0278 (white) and -0.0275 (black). Numerical values are in a.u..

There are minima critical points in the interstitial space that can visually detected using VESTA-program. In addition, 1D plots for different directions in the unit cell show how the chemical pressure between two adjacent Ca atoms changes along the Ca–Ca contacts. For example, when we move along the unit cell diagonal connecting two Ca atoms at the corners, the 1D CP profile exhibits roughly three minima (see insets of Fig. 7.3). The minima in the center of the cell (between 4 and 5 Å) are related to the position of oxygen in the B1 structure of CaO, whereas the other two minima in each sub-figure are related to the position of fluorine in CaF_2. The fact that the two minima in the upper sub-figure have a lower CP value is related to the higher lattice parameters of CaF_2 when compared with B1-CaO. In this case, we can conclude that the positions of the CP minima in the equilibrium *fcc*-Ca structure allow us to anticipate that the lattice parameter of CaF_2 is higher than the one of B1-CaO.

7.3.2 *sc*-Ca

Similar results were obtained for *sc*-Ca phase. In the work of Vegas *et al.* [123], the ELF was calculated at a=3.498 Å (equilibrium volume at 0 GPa) and at a volume where the induced B2 phase has emerged (a=2.645 Å at 26 GPa). In the latter, an ELF attractor is located at the cell center which is coincident with the position of the oxygen atom in B2-CaO.

Concerning our calculations, we show in Fig. 7.4 how the 3D CP maps display a localization of negative CP at the same position in the center of the cube only when the volume of the B2-CaO structure is considered. At the equilibrium volume of *sc*-Ca, the situation is not so clear and the negative CP value at the center of the cube is much higher. We can see these results with more detail in the 1D plots of Fig. 7.5 CP.

As in *fcc*-Ca, we observe that the chemical pressure along the Ca–Ca path is very flat. This is the common behavior in the interstitial space in metals (see also sections 5.3.6-6.2.5). The difference in the negative chemical pressure region between the two volumes is the lower CP value obtained for the *sc*-Ca lattice at the reduced volume.

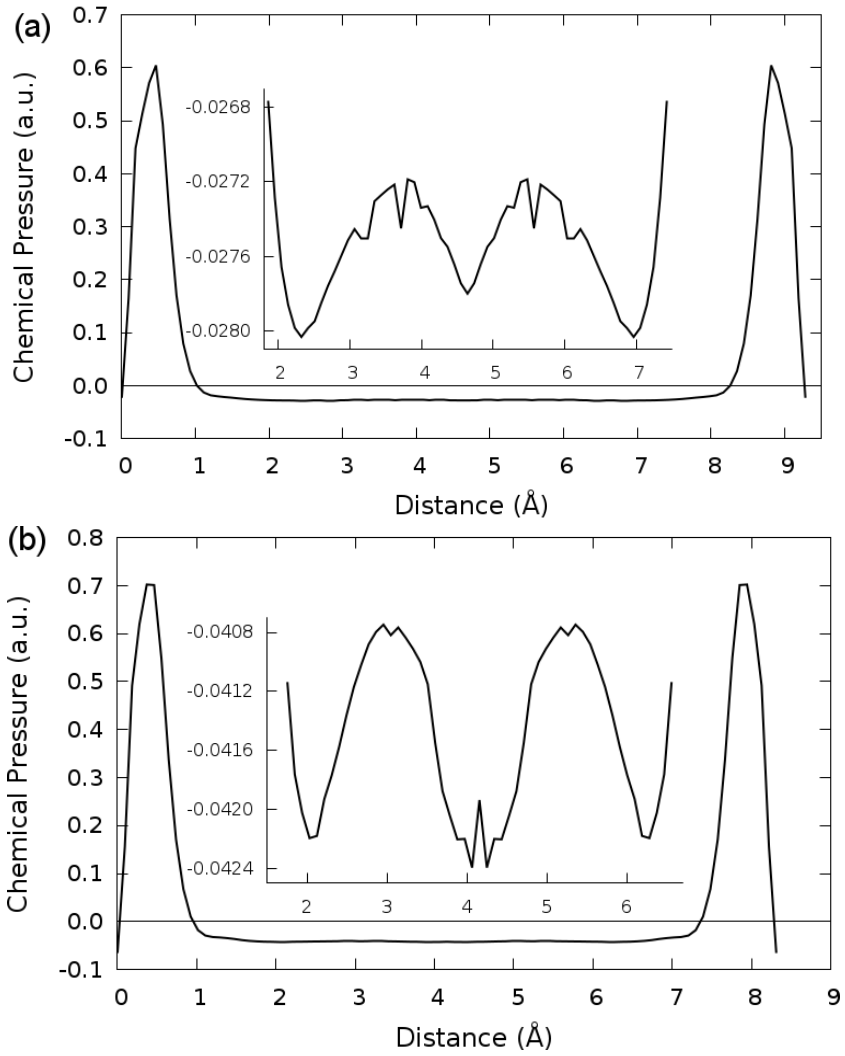

Figure 7.3: 1D profiles of chemical pressure along the diagonal of (a) *fcc*-Ca lattice and (b) the same lattice of (a) at the volume of its oxide phase.

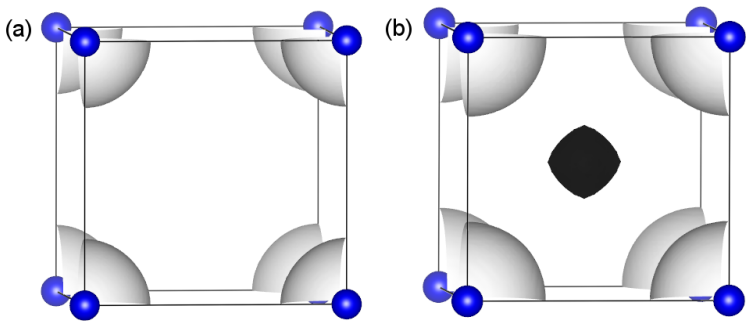

Figure 7.4: Chemical pressure analysis of *sc*-Ca lattice. 3D isosurfaces of CP=±0.066 a.u. for (a) the equilibrium volume and (b) the CaO volume.

It is also observed that the distance at which the flat region of negative CP begins is around 1 Å for the equilibrium volume of *sc*-Ca. This distance is slightly lower for the structure with a reduced volume. The same results were obtained for *fcc*-Ca and suggest the possibility of defining an ionic radius for the metallic cations using

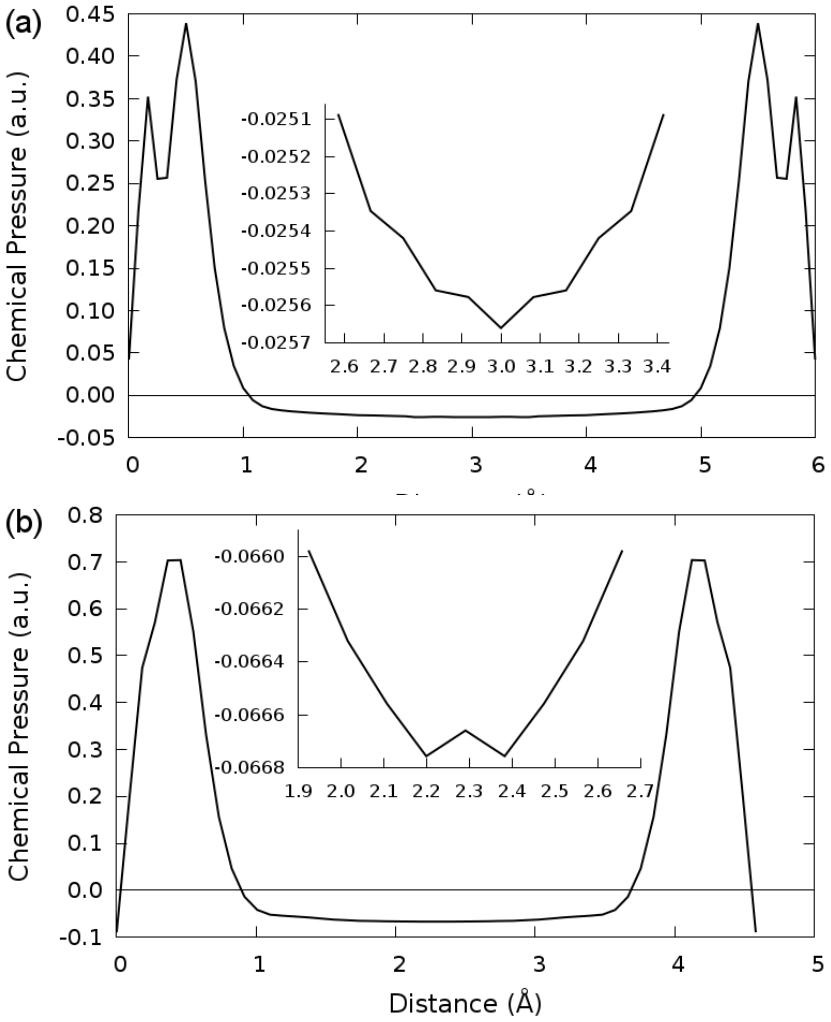

Figure 7.5: 1D profiles of chemical pressure along the diagonal of *sc*-Ca structure at (a) the equilibrium volume and (b) a reduced volume corresponding to the B2 phase of CaO.

the distance defined above. Interestingly enough, the Pauling's ionic Ca^{2+} radius is 0.99 Å.

7.3.3 BaSn

In case of BaSn, ELF calculations show equivalent results as the ones we have discussed for *fcc*- and *sc*-Ca structures. Vegas *et al.* [123] found ELF attractors at the centers of the six phases of the cubic unit cell, which are the positions of the oxygen atoms in the $BaSnO_3$ perovskite structure. Thus, an octahedron of ELF attractors surround the tin atom located at the center of the cubic unit cell.

Results from our CP calculations provide regions of negative CP at the same positions of the ELF attractors when we use the equilibrium lattice parameter of $BaSnO_3$ (see Fig. 7.6). It is clear that the CP formalism is able to identify the positions of the anions in the metallic sub-lattices.

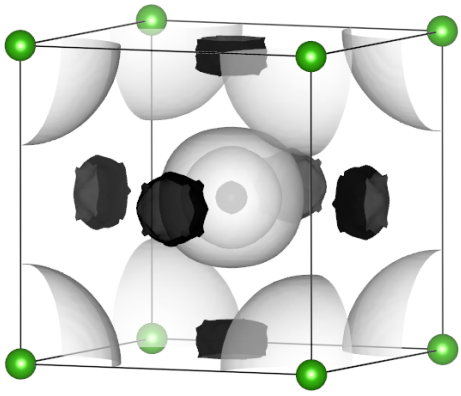

Figure 7.6: Chemical pressure distribution of BaSn crystal lattice. 3D white and black iso-surfaces of CP=0.00 and CP=-0.0125 a.u., respectively.

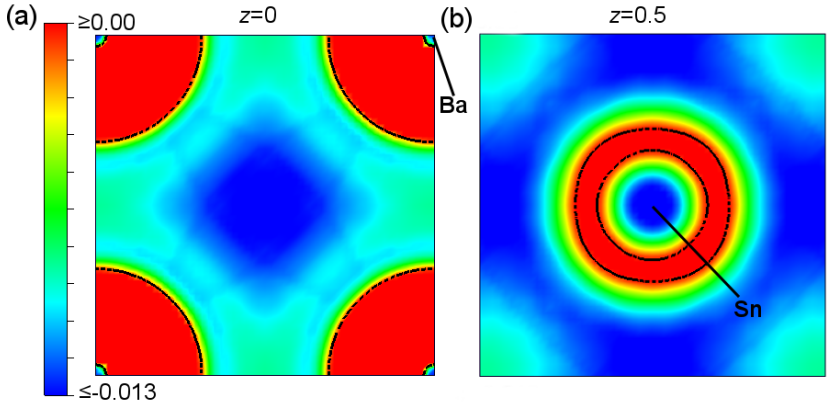

Figure 7.7: Cross-sections of the chemical pressure map for BaSn through [0 0 1] plane at (a) z=0 and (b) z=0.5 from the origin.

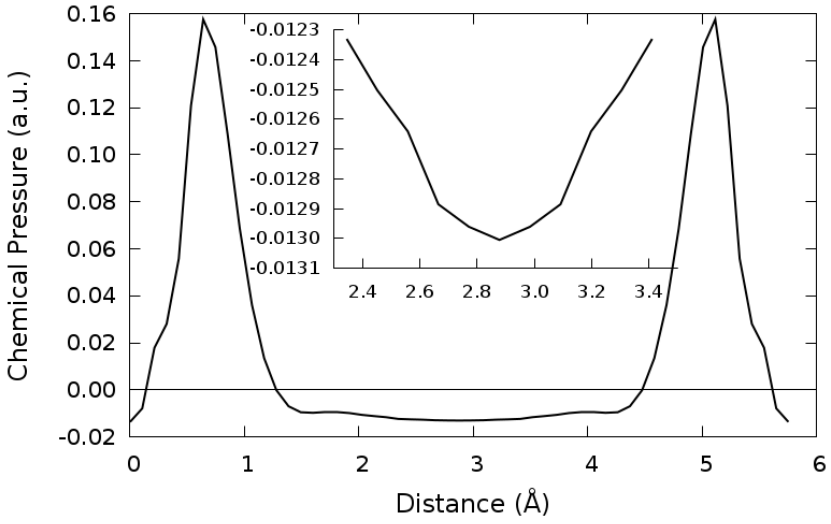

Figure 7.8: 1D profile of the chemical pressure distribution of BaSn crystal lattice along one face diagonal between two Ba atoms.

In terms of the 2D CP maps, we obtain a qualitative description of the metallic cores similar to the one of *fcc*- and *sc*-Ca. When we use a scale of negative values,

it is clearly seen that these metallic cores have a spherical shape with an average positive CP. Again, the high positive CP (dense red) surrounding the Ba atomic positions is due to the semi-core $5s^2 5p^6$ electrons. For Sn, as the semi-core option is not available, the CP values surrounding its nucleus do not produce a clear positive region, except for circular crown that can be used to delimit the Sn^{4+} size. According to the distances from the nuclei up to the zero CP isoline, the Ba^{2+} and Sn^{4+} radii are estimated as 1.29 and 0.90, respectively. These values are in fair agreement with the corresponding Pauling's ionic radii of 1.35 Å and 0.71 Å. Which is to be emphasized is that in the flat negative CP region, the minima (dense blue) appear at the cubic face centers (see Fig. 7.7). These minima can be characterized in the 1D CP profile connecting two Ba atoms along a face diagonal. In Figure 7.8, such a profile is plotted for a BaSn metallic lattice with the same dimensions as in $BaSnO_3$ perovskite.

7.3.4 *fcc*-Na

We studied metallic sodium with the *fcc* structure because this is the matrix sublattice in the B1 phase of NaX (X=F, Cl, Br) ionic crystals at room conditions. Results in this section can be compared with those described for *bcc*-Na in sections 5.3.6-6.2.5. Chemical pressure maps were obtained at the corresponding volumes of NaF, NaCl, and NaBr. In Fig. 7.9, the 3D plots with negative and zero CP isosurfaces are displayed for the three crystals. We have kept the relative size of their unit cells in order to make the results comparable with each other. In all the cases, it is observed the characteristic spherical shape of the metallic Na^+ cation. Regions of negative CP are located at the center of the cube, at the centers of the edges, and at the eight equivalent positions represented by $(\frac{1}{4}, \frac{1}{4}, \frac{1}{4})$. It is interesting to notice that the same qualitative view is obtained regardless the dimensions of the unit cell.

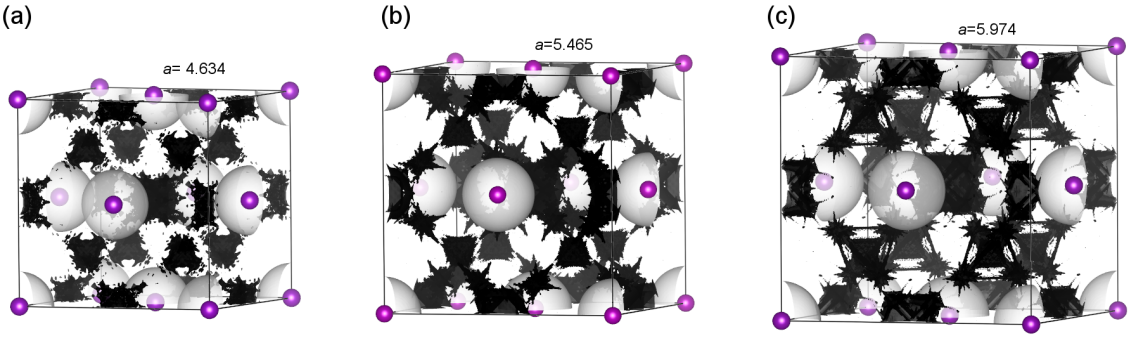

Figure 7.9: Chemical pressure analysis of *fcc*-Na at the equilibrium volumes of its corresponding ionic crystal. 3D white isosurfaces of CP=0.00. Black isosurface of (a) CP=-0.044 a.u. at the volume of NaF, (b) CP=-0.021 a.u. at the volume of NaCl, and (c) CP=-0.017 a.u. at the volume of NaBr. The cell parameter *a* is given in Å.

This result is also obtained when the 2D maps of the [0 0 1] plane of the *fcc*-Na unit cell is analyzed (see Fig. 7.10). Using the zero pressure isoline as a measure of the size of Na^+, the radii calculated along the edges slightly increases from NaF (0.77 Å) and NaCl (0.84 Å) to NaBr (0.87 Å), following a similar rate as their cor-

responding lattice parameters. As we will see in other results, the similarities are greater between NaCl and NaBr than when NaF is involved. Nevertheless, we can conclude that the CP maps are quite independent on the lattice parameters.

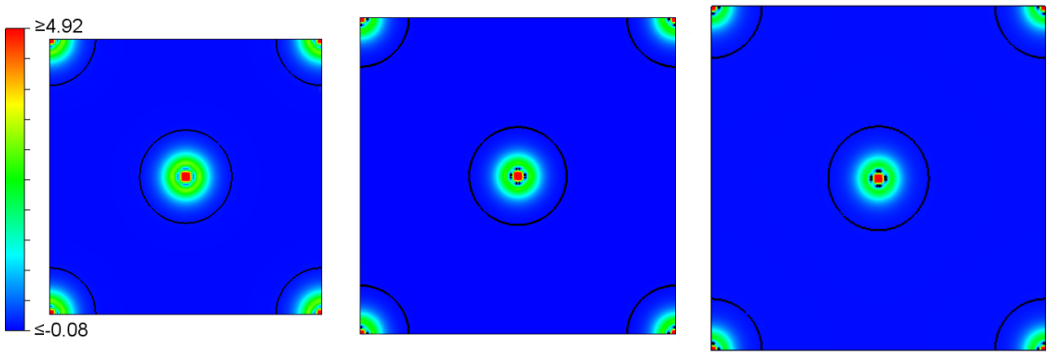

Figure 7.10: Chemical pressure cross-section of [0 0 1] plane of *fcc*-Na at the corresponding equilibrium volumes of NaF, NaCl, and NaBr crystals. Black curves for CP=0.0.

7.4 OXIDE AND HALIDE CRYSTALS

In this section, we present the CP distributions within the corresponding oxide and halide structure of the systems mentioned above. The CP features in both cases can be compared to recognize the overall effect of the anion occupation on the CP distribution in the metallic sub-lattice.

7.4.1 B1-CaO

In B1-CaO structure (a=4.829 Å), the oxygen atoms are now occupying the positions of negative CP isosurfaces at the centers of the edges of the cubic unit cell previously shown in Fig. 7.2. Negative CP isosurfaces at $(\frac{1}{4}, \frac{1}{4}, \frac{1}{4})$ positions are still present (see Fig. 7.11) with a value of -0.063 a.u.. It is illustrative to compare this value with those obtained at the same positions in *fcc*-Ca at two different lattice parameters in order to distinguish the effects of a reduction of the volume (macroscopic pressure) and the presence of oxygen in the lattice. At the *fcc*-Ca equilibrium volume (a=5.521 Å), the CP value is -0.0275 a.u., whereas a value of -0.0422 a.u. was obtained when we use the same lattice parameter (a=4.829 Å) as in the B1-CaO structure. We noticed that, according to its equation of state, this is the lattice parameter of *fcc*-Ca at around 10 GPa. It is clear that there is an equivalent effect of the macroscopic pressure and the insertion of oxygen atoms into the *fcc*-Ca lattice. The first one induces a reduction in the value of CP at the $(\frac{1}{4}, \frac{1}{4}, \frac{1}{4})$ positions from -0.0275 to -0.0422 a.u., and the second one a further lowering of CP to the final value of -0.063 a.u. in B1-CaO.

In Fig. 7.11, the Ca and O atoms are surrounded by white isosurfaces of zero pressure value. According to the CP results, the ionic radius for Ca^{2+} in B1-CaO is 0.90 Å compared to 1.02 Å in the *fcc*-Ca sub-lattice (see Fig. 7.2). These two values are in a good agreement with the Pauling's ionic radius of Ca^{2+} which is 0.99 Å.

This comparison leads to the conclusion that the Ca atom nearly keeps the same size in oxide crystal as in the metal.

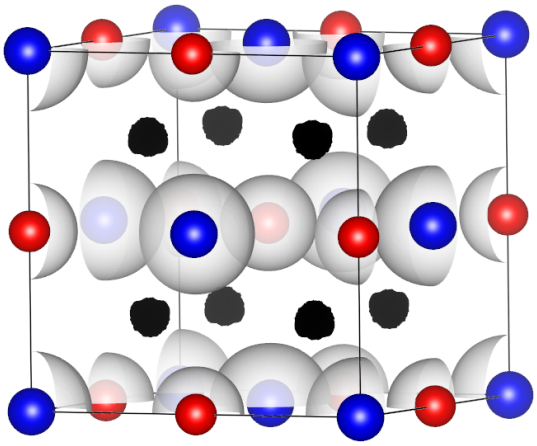

Figure 7.11: Chemical pressure distribution within B1-CaO crystal. (a)3D isosurfaces of CP=0.0 (white) and -0.063 (black) a.u.. Balls in blue and red represent Ca and O atoms, respectively.

On the other hand, we present in Fig. 7.12 the [0 0 1] cross-sections of CP for the B1-CaO crystal. In these CP maps, and for a clear comparison, we adjusted the CP range to that one used for the CP maps of the *fcc*-Ca presented in Fig. 7.1. We see clearly how the CP features around the Ca core are mostly preserved in the oxide phase of Ca. Besides, the distance from the Ca nucleus to the zero pressure black isoline, which is equivalent to the white 3D isosurface, is almost the same in both crystal structures.

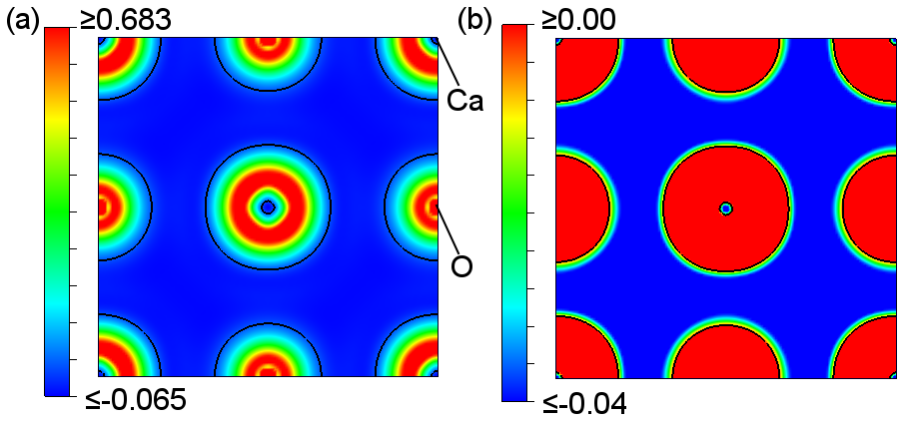

Figure 7.12: Cross-sections of chemical pressure for B1-CaO crystal through [0 0 1] plane. The CP range is adjusted to (a) (-0.065–0.683) and (b) (-0.04–0.00) a.u..

7.4.2 B2-CaO

Similar results were obtained in the B2-CaO crystal structure. In Fig. 7.13-a, we show the 3D isosurfaces of CP in which the minimum obtained in the metallic sublattice is now occupied by the oxygen atom (see Fig. 7.4). A very flat negative CP

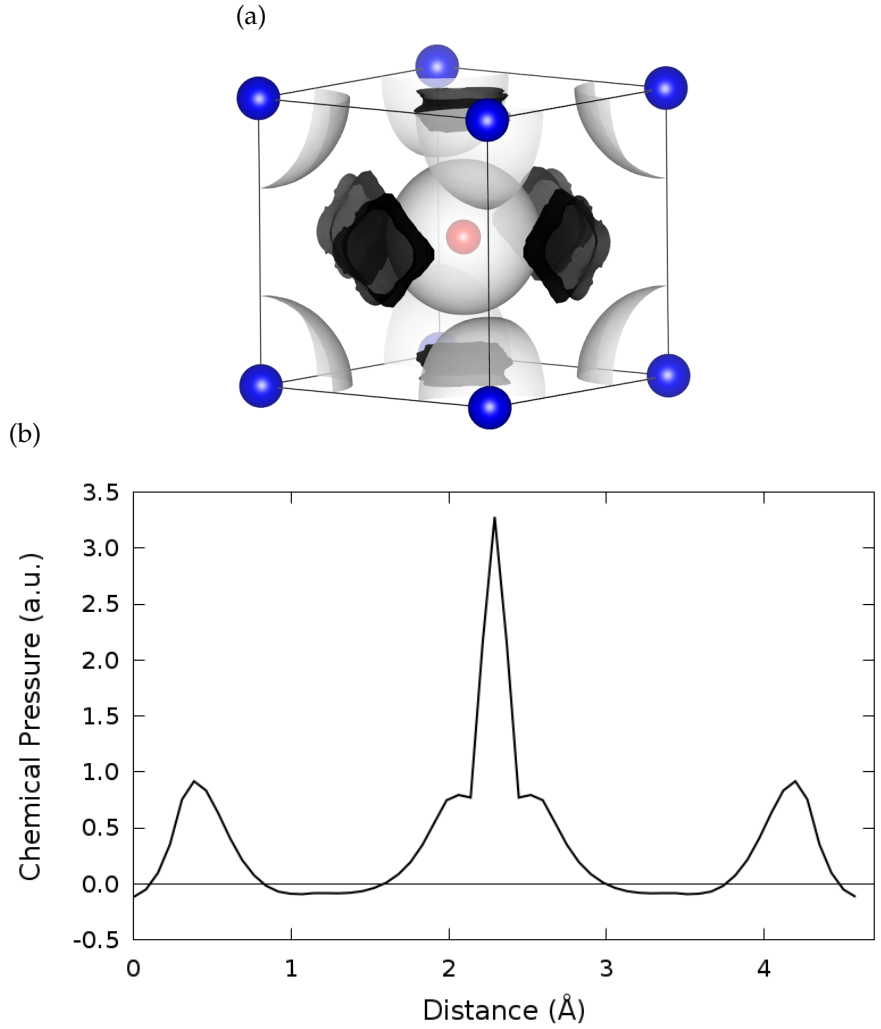

Figure 7.13: Chemical pressure distribution within B2-CaO crystal. (a)3D isosurfaces of CP=0.0 (white) and -0.1 (black) a.u.. Balls in blue and red represent Ca and O atoms, respectively. (b) 1D profile of CP along the unit cell diagonal (Ca–O–Ca).

appears around the centers of the cube faces. This can be observed in terms of the 1D profile of the CP along the cube diagonal (Ca–O–Ca path) in Fig. 7.13-b. The minimum seen in the inset of Fig. 7.5-b is now replaced by a maximum representing the oxygen nucleus. Besides, the distance from the Ca nucleus up to the zero isoline is 0.83 Å compared to 0.87 Å and 1.05 Å in metallic *sc*-Ca lattice at the same volume of B2-CaO and its equilibrium volume, respectively. These values are very close to those obtained in the *fcc* structure of Ca and CaO.

7.4.3 $BaSnO_3$

We have shown that in the BaSn sub-lattice, minima of CP are located at the cube face centers, i.e. the psoitions of oxygen atoms in $BaSnO_3$. In a similar way, we compare the 2D and 3D plots for BaSn and $BaSnO_3$ to see the effect of the oxygen atoms on the CP features of the main metallic sub-lattice. In Fig. 7.14, we show that the

minima seen in the BaSn crystal (with a octahedron-like shape) are now replaced by the oxygen atoms surrounded by zero pressure isosurfaces (white). Also, it is noticed that the spherical positive CP surrounding the Sn nucleus in BaSn lattice is now distorted into oval-shapped regions of positive CP located between the Sn–O contacts in $BaSnO_3$ crystal.

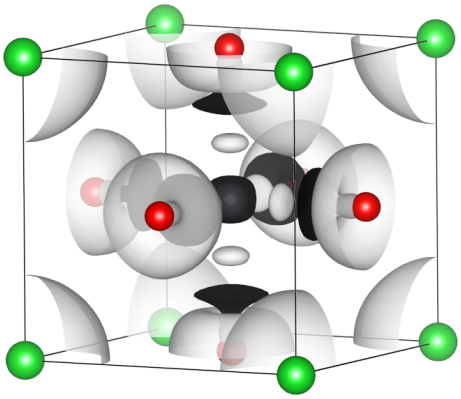

Figure 7.14: Chemical pressure distribution within $BaSnO_3$ crystal. 3D isosurfaces of CP=0.00 (white) and -0.032 (black) a.u.. Balls in green, gray, and red represent Ba, Sn, and O atoms, respectively.

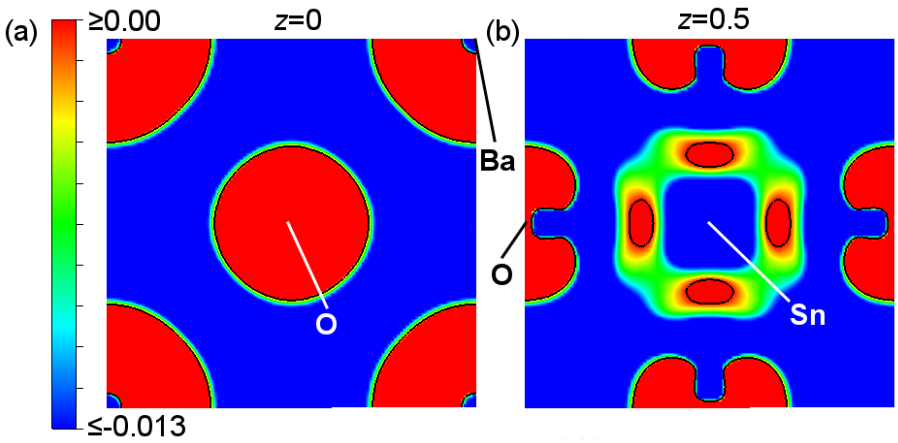

Figure 7.15: 2D chemical pressure maps for $BaSnO_3$ crystal. The maps are taken through [0 0 1] plane at (a) z=0.0 (b) z=0.5 adjusted to the same CP range. A black contour is shown for CP=0.0.

Concerning the ionic radii of Ba^{2+} and Sn^{4+}, we obtained values of 1.13 Å and 0.90 Å, respectively. The latter was measured from the Sn nucleus up to the zero CP isoline along the Sn–O contacts. Similarly to Ca/CaO pair, the atomic size of Ba^{2+} decreases a little in the oxide crystal. In the 2D CP maps of Fig. 7.15, it is seen clearly how the CP features around the Ba atom are roughly kept in BaSn/$BaSnO_3$ (see Fig. 7.7).

7.4.4 Na-halide crystals

Moving to the last example of this discussion, we studied the B1 phases of NaX (X=F, Cl, Br) to compare with the results previously presented for the *fcc*-Na at the equilibrium volume of the NaX crystals. We observed an equivalent CP behavior in the three cases. So we will show the 2D and 3D plots of CP distributions only for NaF crystal (see Fig. 7.16). The 2D CP map of NaF shows mostly the same CP features around the Na nucleus as in its metallic sub-lattice (see Fig. 7.10). In addition, as seen in B1-CaO (see Fig. 7.11), the negative CP isosurfaces obtained at $(\frac{1}{4}, \frac{1}{4}, \frac{1}{4})$ positions in the metallic Na sub-lattice (see Fig. 7.9), can be also seen within the NaF crystal with a lower CP value (-0.086 a.u.). In this case, as we used the same lattice parameter for *fcc*-Na and B1-NaF, the lowering in the CP from -0.044 to -0.086 is entirely due to a *pressure* effect of the fluor sub-lattice.

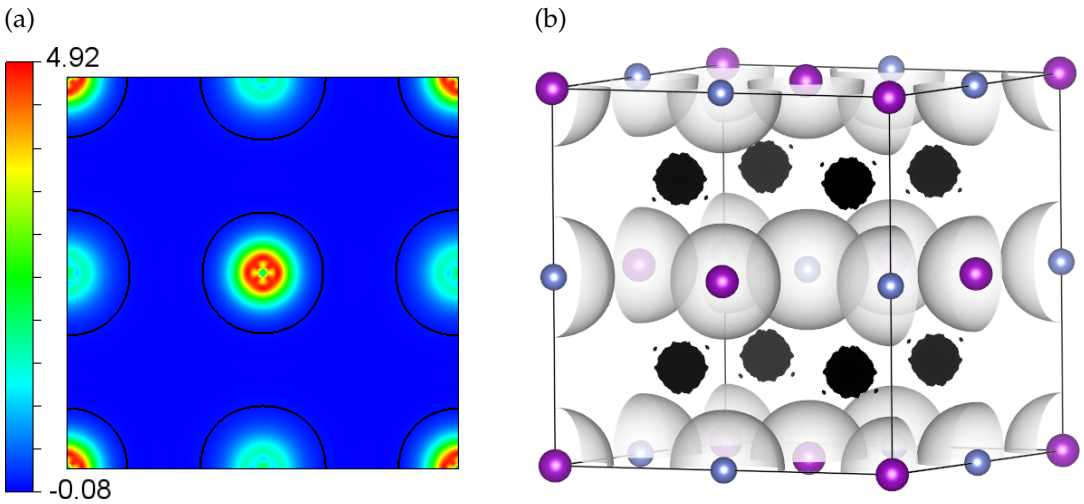

Figure 7.16: Chemical pressure calculated for *fcc*-NaF. (a) 2D CP map along [0 0 1] plane including both atom types. Black isolines of CP=0.0 are loaded to the 2D map. (b) 3D isosurfaces of CP=0.00 (white) and CP=-0.086 (black).

We illustrate the CP profiles along the Na–X paths in the 1D plot of Fig. 7.17. It is interesting to notice how the differences in these profiles can be related to different electronegativities of the halide atoms. For example, the maximum CP near the Na nucleus increases along the sequence Br, Cl, and F. The attached zoom in for the distance range 0.6-1.4 Å shows that the CP along the Na–F path varies with lower CP values than the other halides. Besides, the CP behavior of NaCl and NaBr is very similar, although the trend F, Cl, and Br is maintained. The calculated ionic radii of Na^+ in the three crystals are 0.70, 0.76, and 0.78 Å for respectively NaF, NaCl, and NaBr. These values are very close to those calculated in the metallic sub-lattice. All these results point to similar CP features of the metallic sub-lattice in both the metal and the halide crystals, thus supporting the Anions in Metallic Matrices model of Vegas *et al.*.

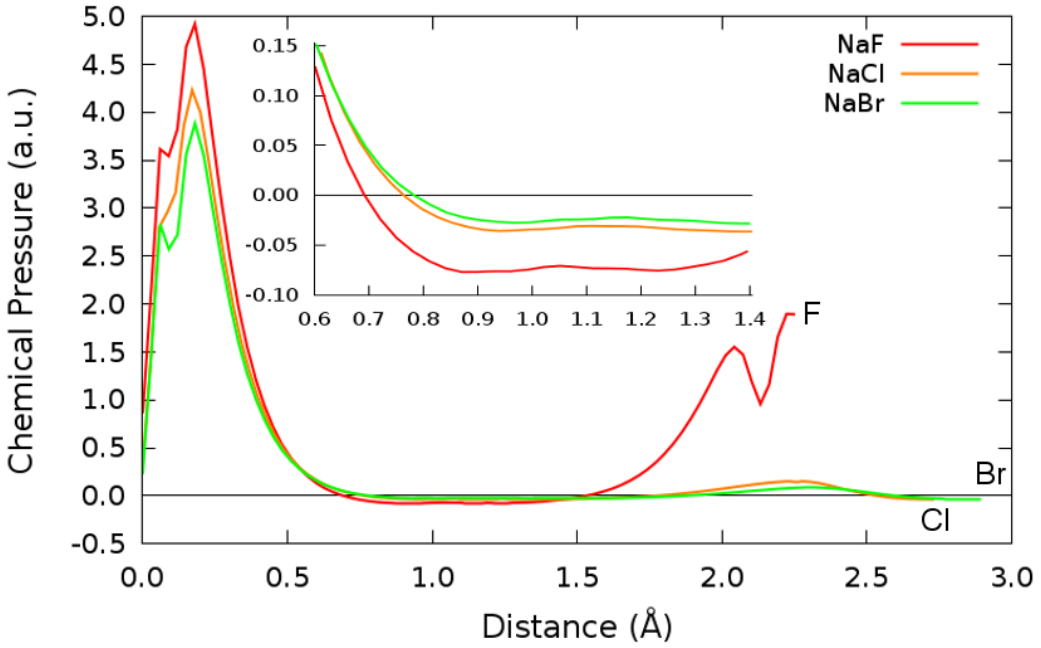

Figure 7.17: 1D profiles of the CP along the Na-X bond (X = F, Cl, Br). Zoom in for a selected distance is attached.

Considering also the metal and metal-oxide systems, we can say at this point that the CP formalism is not only able to reproduce similar results to those obtained with the ELF as regards the AMM model but it also provides quantitative criteria to measure the effect of the anions when introduced in the metallic sub-lattice. For example, the evaluation of CP values at particular positions or atomic/ionic radii can be used for that purpose if they are calculated at different lattice volumes of the metallic sub-lattice and the corresponding metal-anion compound. Future work along this direction is necessary to account for a clear relationship between macro and local pressures in inorganic compounds.

Part VI

Conclusions

8 CONCLUSIONS

The purpose of this chapter is to summarize our main contributions and to put some concluding remarks for the results presented in this thesis.

In part II, we have briefly presented the basic concepts of quantum chemistry related to the density functional theory (DFT) approximation. Principles of Kohn–Sham equations and how to solve these equations to calculate different physical properties were also discussed. This is followed by a detailed presentation of the Chemical Pressure (CP) approach that can be used to characterize and visualize the local pressures within a crystal structure. This dense chapter shows the complete idea for the DFT-Chemical Pressure formalism that we have applied in this thesis. The second chapter of this part concerns the computational procedure of both the electronic structure calculations and the chemical pressure analysis done for all the systems studied in the following chapters.

In part III, we examined the behavior of $Cs_2UO_2Cl_4$ under hydrostatic pressure. This compound is quite compressible and exhibits a structural anisotropy mainly controlled by the orientation of the uranyl moiety. d_{UO}, d_{UCl}, and d_{CsO} distances decrease roughly by 0.01, 0.20, and 0.95 Å in the $0-50$ GPa pressure range, thus providing information on the strengths of bonds and interactions, and also on the main mechanisms of volume reduction under applied pressure. Our calculated equation of state parameters are new to the best of our knowledge, and deserve experimental measurements to be contrasted with. In addition to structural data, vibrational stretching frequencies were calculated in order to analyze their correlation with U–O bond lengths and the charge transferred to UO_2. According to our calculations, d_{UO} shows two opposite trends under hydrostatic pressure: an unexpected increase of 0.006 Å in the low pressure regime followed by a quasi-linear decreasing trend up to 50 GPa. We obtain different force constants for uranyl bonds of the same length, which confirms that Badger's rule is invalid in its traditional form. We found a plausible interpretation in terms of which is the main factor controlling d_{UO}-stretching frequency relationships. The charge transferred to uranyl is a key factor in the low pressure region resulting in a red shift trend for the Raman symmetric stretching frequency. Pressure-induced shortening of distances dominates the ν_1-d_{UO} trend at pressures above 10 GPa. In this high pressure region, the mechanical effect leads to Cs–O interactions to enter in the repulsive region enhancing the shortening of the U–O distance, which results in a blue shift trend for the Raman frequency. Interestingly enough, in both regimes, independent Badger's linear relationships are found, though a unique correlation covering the whole pressure range can also be obtained when charge transfer effects are removed.

In part IV, we presented how the DFT Chemical Pressure (CP) method can form the basis of the visualization of the forces within chemical bonds. Over a series of molecular and crystalline examples, specific features in the CP maps have become associated with different types of bonding interactions. Focused concentrations of

negative pressures along an interatomic contact (countered by positive pressures near the cores) correlate strongly with the presence of covalent bonds, while weaker intermolecular interactions, such as van der Waals attraction and hydrogen bonds, were reflected in much shallower negative CP features. Model systems for metallic and ionic bonding, meanwhile, exhibite much less directional interactions, with the major balance of forces being between positive CPs around the ion cores and a background negative pressure representing the long-range electrostatic forces. In each of these systems, but most particularly the covalent cases, the CP features provided images quite similar to those that would be obtained with another method for visualizing bonding features: the electron localization function. With the CP approach, however, these features now have clear interpretations in terms of forces calling for the expansion and contraction of the structures, which can be investigated in more detail by separately plotting different energetic contributions to the CP map, such as the kinetic and potential energy terms. The pictures that result for the covalent bond closely align with the model for the chemical bond described in detail by Ruedenberg and coworkers for simple molecular systems such as H_2, and offer the opportunities for similar levels of insight to be attained for more complex systems.

Besides, in chapter 6, we discussed the origin of the CP features in the studied systems through going further in the analysis of the main energetic contributions which can be separately mapped. In terms of the kinetic energy and the main contributions to the potential energy (Hartree, local pseudopotential, exchange-correlation, and Ewald energy terms), we showed that the positive kinetic chemical pressure located away from the bonding region close to the nuclear positions can be understood in as a form of promotion effect. Away from the internuclear region, the potential is more like that of the free atoms; the deviations from the free-atom wavefunctions induced by the bonding region are then, locally, perceived as a destabilizing perturbation. Interestingly, we are able to recognize the differences between the weak intermolecular interactions, van der Waals and hydrogen-bond. We showed that negative CPs occur between the sheets of graphite and this is reassuring, as it suggests an attractive force is holding the layers together. On the other hand, in the hydrogen-bond region, the positive pressure stemming from the oxygen atom arises from the potential energy, which contrasts sharply with the negative local contribution we have generally observed for covalent interactions. We presented, from the point of view of CP analysis, the difference between metallic and covalent bonding. It can be seen in the nature of the driving forces competing for the expansion and contraction of the structure. For the covalent bond, this competition was essentially between the enhanced stability of electrons concentrating near the cores along the interatomic vectors against the kinetic energy costs that the wavefunctions feel away from the bonding region. In the metal, however, the primary balance occurs instead between the kinetic energy costs of squeezing the cores against the electrostatic attraction between the cores and the electron gas (which belongs to the Ewald term of the total energy).

In part V, we explored the chemical pressures within different metallic sub-lattices and the corresponding oxide/halide crystals such as Ca/CaO, BaSn/$BaSnO_3$, and Na/NaX (X=F, Cl, Br). Our results show that the CP approach can be used to obtain similar information to that discussed by the AMM model based on the ELF results.

Besides, we have shown that the addition of anions is nearly equivalent to the pressure application in reduction of the lattice volume. The distance from the nucleus to the zero CP isoline is a propose as a parameter for estimating ionic radii. When this parameter is evaluated to calculate the radii of cations in metals, halides, and oxides, we obtained results in fair agreement with Pauling's radii. The CP features in the metallic sub-lattice are mostly preserved in the corresponding oxide/halide lattice. Consequently, we found for example that the ionic radii are very similar in both lattices, although more analysis and systems have to be considered before establishing general conclusions. By the end of this part, we presented the CP distribution in the halide systems showing how the effect along the Na–halide bonding paths shows a reasonable trend with the atomic number of the halide. This behavior is chemically intuitive and deserves further investigation that could lead to a quantitative relationship between chemical pressure and electronegativity.

El propósito de este capítulo es resumir nuestras principales contribuciones y añadir algunos comentarios finales sobre los resultados presentados en esta tesis.

En la parte II, hemos presentado brevemente los conceptos básicos de química cuántica relacionados con la aproximación de la teoría del funcional de la densidad (DFT). Discutimos también los principios que subyacen a las ecuaciones de Kohn-Sham y cómo se resuelven estas ecuaciones para obtener la solución de la ecuación de Schrödinger en un sistema cristalinos. A continuación llevamos a cabo una presentación detallada del formalismoe de la Presión Química (CP) y su utilización para caracterizar y visualizar las presiones locales dentro de una estructura cristalina. Este capítulo es denso y muestra la idea completa del formalismo DFT-Presión Química que hemos aplicado en esta tesis. El segundo capítulo de esta parte trata el procedimiento computacional tanto de los cálculos de estructura electrónica como del análisis de la presión química realizados para todos los sistemas estudiados en esta tesis.

En la parte III examinamos el comportamiento del $Cs_2UO_2Cl_4$ bajo presión hidrostática. Este compuesto es bastante compresible y presenta una anisotropía estructual principalmente controlada por la orientación del grupo uranilo. Las distancias d_{UO}, d_{UCl}, y d_{CsO} disminuyen aproximadamente 0.01, 0.20, and 0.95 Å en el rango de presión $0-50$ GPa, proporcionando información sobre la fortaleza de los enlaces e interacciones, y también sobre los mecanismos principales de la reducción de volumen bajo la aplicación de presión. los parámetros de nuestra ecuación de estado calculada son, hasta donde sabemos, nuevos y merecerían ser contrastados con medidas experimentales. Además de los datos estructurales, se calcularon frecuencias vibracionales de tensión con el fin de analizar su correlación con la longitud de enlace U–O y con la carga transferida al UO_2. Según nuestros cálculos, d_{UO} presenta dos tendencias opuestas al aplicar presión hidrostática: un aumento inexperado de 0.006 Å en el regimen de presiones bajas seguido por una disminución aproximadamente lineal en el rango de presiones altas hasta 50 GPa. Hemos obtenido constantes de fuerza diferentes para enlaces uranilo de la misma longitud, lo que confirma que la regla de Badger no es v álida en su forma tradicional. Hemos encontrado una interpretación verosímil en términos del factor principal que controla la relación entre d_{UO} y la frecuencia de tensión. La carga transferida al uranilo es un factor clave en la región de baja presión, lo que resulta en un desplazamiento al rojo en la frecuencia Raman de tensión simétrica. La relación ν_1-d_{UO} a presiones por encima de 10 GPa está dominada por el acortamiento de las distancias inducido por la presión. En esta región de alta presión, el efecto mec ánico lleva a las interacciones Cs–O a entrar en la región repulsiva, favoreciendo el acortamiento de la distancia U–O, lo que resulta en un desplazamiento al azul de la frecuencia Raman. Es interesante señalar que hemos encontrado, en los dos regímenes, relaciones lineales de Badger independientes, aunque puede obtenerse una correlación única abarcando el rango entero de presiones si se eliminan los efectos de la transferencia de carga.

En la parte IV hemos mostrado cómo el método DFT de la presión química (CP) puede constituir una base para la visualización de las fuerzas dentro de los enlaces químicos. Utilizando una serie de ejemplos moleculares y cristalinos, se han asociado ciertas características específicas en los mapas CP con diferentes tipos de interacciones de enlace. Las concentraciones de presión negativa a lo largo de un contacto interatómico (contrarrestadas por presiones positivas cerca de las regiones

atómicas internas) se correlacionan con la presencia de enlaces covalentes, mientras que las interacciones intermoleculares más débiles, tales como la interacción de van der Waals y los enlaces de hidrógeno, se ven reflejadas en zonas de presión química negativa menos profundas. Los sistemas modelo para el enlace metálico e iónico presentan interacciones mucho menos direccionales, siendo el principal balance de fuerzas el existente entre presiones químicas positivas cerca de los iones y una presión negativa de fondo que representa las fuerzas electrostáticas de largo alcance. En cada uno de estos sistemas, pero particularmente en los casos covalentes, las características de los mapas de presión química proporcionan imágenes bastante similares a aquellas que se obtendrían con otro métodos de visualización del enlace químico como la función de localización electrónica. Con el enfoque CP, sin embargo, esas características distintivas tienen ahora una interpretación clara en términos de fuerzas compitiendo por la expansión y contracción de las estructuras, que pueden ser investigadas en mayor detalle representando por separado las diferentes contribuciones energéticas al mapa CP, tales como los términos cinético y de energía potencial. La imagen que resulta para el enlace covalente es cercana al modelo del enlace químico descrito en detalle por Ruedenberg y colaboradores para sistemas moleculares sencillos como el H_2, y ofrece oportunidades para alcanzar similares niveles de comprensión en sistemas más complejos.

Además, en el capítulo 6, hemos discutido el origen de las características observadas en los mapas CP de los sistemas estudiados, profundizando en el estudio de las distintas contribuciones a la presión química que pueden representarse por separado. Siguiendo a Ruedenberg, hemos mostrado, en términos de la energía cinética y de las principales contribuciones a la energía potencial(Hartree, pseudopotential local, cambio-correlación y energía de Ewald), que la presión química positiva debida a la energía cinética positiva, localizada fuera de la región de enlace y cerca de las posiciones nucleares, puede ser entendida como consecuencia del llamado *promotion state*. Fuera de la región internuclear, el potencial es más parecido al de los átomos libres; las desviaciones de las funciones de onda del átomo libre inducidas por la región de enlace son, entonces, percibidas localmente como una perturbación desestabilizadora. Resulta interesante comprobar que es posible reconocer las diferencias entre las interacciones intermoleculares débiles: van der Waals y enlace de hidrógeno. Hemos mostrado que entre las láminas de grafito aparecen presiones químicas negativas que sugieren la presencia de una fuerza atractiva manteniendo las láminas unidas. Por otro lado, en la región del enlace de hidrógeno, la presión positiva proveniente del átomo de oxígeno resulta de la energía potencial, lo que contrasta fuertemente con la contribución local negativa que hemos observado generalmente en las interacciones covalentes. Presentamos, desde el punto de vista del análisis CP, La diferencia entre el enlace metálico y covalente. Puede verse en la naturaleza de Las fuerzas motrices que compiten por la expansión y contracción de la estructura. En el enlace covalente esta competencia se produce esencialmente entre la estabilidad inducida por la densidad electrónica que se concentran cerca de los núcleos a lo largo de la dirección del enlace y el coste de la energía cinética asociado con la función de onda en regiones alejadas de la zona de enlace. En los metales, sin embargo, el balance se produce entre el coste energético debido al incremento de la energía cinética alrededor de las posiciones nucleares y la atracción electrostática entre los núcleos y el gas de electrones (término Ewald de la energía total).

En la parte V exploramos las presiones químicas en diferentes metales y en cristales de óxido/haluro tales como Ca/CaO, BaSn/$BaSnO_3$, y Na/NaX (X = F, Cl, Br) en donde estas subredes metálicas están presentes. Nuestro análisis muestra que el enfoque CP puede utilizarse para obtener información similar a la discutida para el modelo AMM utilizando los resultados de la ELF. Además, hemos demostrado que el papel que juegan los aniones correlaciona con el de la aplicación de presión externa. La distancia desde el núcleo hasta la isolínea de presión química cero se propone como un parámetro para estimar el radio iónico. Cuando este parámetro es utilizado para calcular los radios de los cationes en los metales, haluros y óxidos de nuestro estudio, obtenemos resultados en acuerdo aceptable con los radios iónicos de Pauling. Las características de la presión química en las redes metálicas se conservan en su mayor parte cuando pasamos a los óxidos/haluros en donde están presentes. En consecuencia, se encuentra que los radios iónicos son muy similares en ambos tipos de sistemas, aunque se necesitan más sistemas y análisis antes de establecer conclusiones generales. Al final de esta parte, presentamos la distribución de presiones químicas en los haluros de sodio mostrando cómo el efecto a lo largo del camino de enlace Na-X correlaciona de forma razonable con el número atómico del haluro. Este comportamiento es intuitivo desde el punto de vista químico y merece que sea explorado con mayor profundidad con el objetivo de poder encontrar una relación entre la presión química y la electronegatividad.

LIST OF PUBLICATIONS

1. Hussien H. Osman, Pilar Pertierra, Miguel A. Salvadó, F. Izquierdo-Ruiz and J. M. Recio, "Structure and bonding in crystalline cesium uranyl tetrachloride under pressure." *Phys. Chem. Chem. Phys.*, **18**, 18398–18405, 2016.

2. Hussien H. Osman, Miguel A. Salvadó, Pilar Pertierra, Joshua Engelkemier, Daniel C. Fredrickson, and J. Manuel Recio, "Chemical Pressure Maps of Molecules and Materials: Merg- ing the Visual and Physical in Bonding Analysis." *Journal of the American Chemical Society*, **submitted**.

3. Hussien H. Osman, Pilar Pertierra, Miguel A. Salvadó, Daniel C. Fredrickson, and J. M. Recio, " Chemical Pressure Contributions to Chemical Bonding in Solids." **in preparation**.

4. Hussien H. Osman, Pilar Pertierra, Miguel A. Salvadó, Vegas Á, and J. M. Recio, "The Anion in Metallic Matrices model in the light of the Chemical Pressure formalism.", **in preparation**.

LIST OF FIGURES

LIST OF TABLES

Part VII

Bibliography

BIBLIOGRAPHY

[1] Bacskay, G. B. and Nordholm, S. "Covalent Bonding: The Fundamental Role of the Kinetic Energy." *The Journal of Physical Chemistry A*, **117** (33), (2013), pp. 7946–7958 (cit. on p. 61).

[2] Bader, R. F. W. *Atoms in molecules : a quantum theory*. The International series of monographs on chemistry. Oxford: Clarendon Press, 1990 (cit. on pp. 3, 6, 37, 60).

[3] Badger, R. M. "A Relation Between Internuclear Distances and Bond Force Constants." *The Journal of Chemical Physics*, **2** (3), (1934), pp. 128–131 (cit. on pp. 42, 52).

[4] Bartlett, J. R. "On the determination of uranium–oxygen bond lengths in dioxouranium(VI) compounds by Raman spectroscopy." *Journal of Molecular Structure*, **193**, (1989), pp. 295–300 (cit. on pp. 51, 52).

[5] Beck, H. P. and Lederer, G. "Thermische Dilatation und Hochdruckverhalten der Zintl-Phasen CaSn und BaSn." *Zeitschrift für anorganische und allgemeine Chemie*, **619** (5), (1993), pp. 897–900 (cit. on p. 109).

[6] Becke, A. D. "Density-functional thermochemistry. III. The role of exact exchange." *The Journal of Chemical Physics*, **98** (7), (1993), p. 5648 (cit. on p. 47).

[7] Becke, A. D. and Edgecombe, K. E. "A simple measure of electron localization in atomic and molecular systems." *The Journal of Chemical Physics*, **92** (9), (1990), pp. 5397– (cit. on pp. 3, 8, 60).

[8] Berns, V. M., Engelkemier, J.,Guo, Y., Kilduff, B. J. and Fredrickson, D. C. "Progress in Visualizing Atomic Size Effects with DFT-Chemical Pressure Analysis: From Isolated Atoms to Trends in AB5 Intermetallics." *Journal of Chemical Theory and Computation*, **10**, (2014), pp. 3380–3392 (cit. on pp. 4, 6, 26, 30, 34).

[9] Birch, F. "Finite strain isotherm and velocities for single-crystal and polycrystalline NaCl at high pressures and 300°K." *Journal of Geophysical Research: Solid Earth*, **83** (B3), (1978), pp. 1257–1268 (cit. on p. 37).

[10] Blanco, M. A., Francisco, E. and Luaña, v. "GIBBS: isothermal-isobaric thermodynamics of solids from energy curves using a quasi-harmonic Debye model." *Computer Physics Communications*, **158** (1), (2004), pp. 57–72 (cit. on pp. 6, 37).

[11] Bloch, F. "Über die Quantenmechanik der Elektronen in Kristallgittern." *Z. Physik*, **52** (7), (1929), pp. 555–600 (cit. on p. 18).

[12] Blöchl, P. E. "Projector augmented-wave method." *Phys. Rev. B*, **50 (24)**, (1994), pp. 17953–17979 (cit. on pp. 6, 21, 33).

[13] Canepa, F. and Eggenhoffner, R. "Investigation about chemical pressure effects on praseodymium intermetallics: II The $Pr_{1-x}Y_xRh$ family." *Journal of the Less Common Metals*, **161** (1), (1990), pp. L33–L36 (cit. on p. 4).

[14] Canepa, F., Franceschi, E. A., Olcese, G. L. and Eggenhoffner, R. "Investigations of chemical pressure effects on the valence behaviour of praseodymium intermetallics I: The $Pr_{1,àíx}Y_xSn_3$ family." *Journal of the Less Common Metals*, **154** (1), (1989) (cit. on p. 4).

[15] Cohen, M. L. and Heine, V. "The Fitting of Pseudopotentials to Experimental Data and Their Subsequent Application." *Solid State Physics*, **24**, (1970), pp. 37–248 (cit. on p. 20).

[16] Contreras-García, J., Pendás, Á. M., Silvi, B. and Recio, J. M. "Bases for Understanding Polymerization under Pressure: The Practical Case of CO_2." *The Journal of Physical Chemistry B*, **113** (4), (2009), pp. 1068–1073 (cit. on pp. 4, 72).

[17] *Critic2*. http://schooner.chem.dal.ca/wiki/Critic2. (Accessed on 04/22/2017) (cit. on p. 38).

[18] Dargent, M., Dubessy, J., Truche, L., Bazarkina, E. F., Nguyen-Trung, C. and Robert, P. "Experimental study of uranyl(VI) chloride complex formation in acidic LiCl aqueous solutions under hydrothermal conditions (T = 21 °C,Äì350°C, Psat) using Raman spectroscopy." *European Journal of Mineralogy*, **25** (5), (2013) (cit. on p. 42).

[19] De Silva, P. and Corminboeuf, C. "Simultaneous Visualization of Covalent and Noncovalent Interactions Using Regions of Density Overlap." *Journal of Chemical Theory and Computation*, **10** (9), (2014), pp. 3745–3756 (cit. on p. 3).

[20] DiMasi, E., Aronson, M. C., Mansfield, J. F., Foran, B. and Lee, S. "Chemical pressure and charge-density waves in rare-earth tritellurides." *Phys. Rev. B*, **52** (20), (1995), pp. 14516–14525 (cit. on p. 4).

[21] Dolyniuk, J.-A., He, H., Ivanov, A. S., Boldyrev, A. I., Bobev, S. and Kovnir, K. "Ba and Sr Binary Phosphides: Synthesis, Crystal Structures, and Bonding Analysis." *Inorganic Chemistry*, **54** (17), (2015), pp. 8608–8616 (cit. on p. 60).

[22] Dorado, B., Amadon, B., Freyss, M. and Bertolus, M. "DFT+U calculations of the ground state and metastable states of uranium dioxide." *Phys. Rev. B*, **79** (23), (2009), pp. 235125–235132 (cit. on p. 33).

[23] Dronskowski, R. and Bloechl, P. E. "Crystal orbital Hamilton populations (COHP): energy-resolved visualization of chemical bonding in solids based on density-functional calculations." *The Journal of Physical Chemistry*, **97** (33), (1993), pp. 8617–8624 (cit. on pp. 60, 61).

[24] Dudarev, S. L., Botton, G. A., Savrasov, S. Y., Humphreys, C. J. and Sutton, A. P. "Electron-energy-loss spectra and the structural stability of nickel oxide: An LSDA+U study." *Phys. Rev. B*, **57**, (1998), pp. 1505–1509 (cit. on p. 18).

[25] Engelkemier, J. and Fredrickson D. C. "Chemical Pressure Schemes for the Prediction of Soft Phonon Modes: A Chemist's Guide to the Vibrations of Solid State Materials." *Chemistry of Materials*, **28** (9), (2016), pp. 3171–3183 (cit. on pp. 4, 6, 34, 60).

[26] Engelkemier, J., Berns, V. M. and Fredrickson, D. C. "First-Principles Elucidation of Atomic Size Effects Using DFT-Chemical Pressure Analysis: Origins of $Ca_{36}Sn_{23}$'s Long-Period Superstructure." *Journal of Chemical Theory and Computation*, **9**, (2013), pp. 3170–3180 (cit. on pp. 23, 24, 28).

[27] Engelkemier, J., Green, L. M., McDougald, R. N., McCandless, G. T., Chan, J. Y. and Fredrickson, D. C. "Putting $ScTGa_5$ (T = Fe, Co, Ni) on the Map: How Electron Counts and Chemical Pressure Shape the Stability Range of the $HoCoGa_5$ Type." *Crystal Growth & Design*, **16** (9), (2016), pp. 5349–5358 (cit. on pp. 4, 6).

[28] Feinberg, M. J. and Ruedenberg, K. "Paradoxical Role of the Kinetic-Energy Operator in the Formation of the Covalent Bond." *The Journal of Chemical Physics*, **54** (4), (1971) (cit. on pp. 4, 61).

[29] Feinberg, M. J., Ruedenberg, K. and Mehler, E. L. "The Origin of Binding and Antibinding in the Hydrogen Molecule-lon." *Advances in Quantum Chemistry*, **5**, (1970), pp. 27–98 (cit. on pp. 4, 61).

[30] Fletcher, R. "A New Approach To Variable Metric Algorithms." *The Computer Journal*, **13** (3), (1970), p. 317 (cit. on p. 34).

[31] Foster, J. M. and Boys, S. F. "Canonical Configurational Interaction Procedure." *Rev. Mod. Phys.* **32** (2), (1960), pp. 300–302 (cit. on p. 60).

[32] Foster, J. P. and Weinhold, F. "Natural Hybrid Orbitals." *Journal of the American Chemical Society*, **102** (24), (1980), pp. 7211–7218 (cit. on pp. 3, 60).

[33] Fredrickson, D. C. "Electronic Packing Frustration in Complex Intermetallic Structures: The Role of Chemical Pressure in Ca_2Ag_7." *Journal of the American Chemical Society*, **133**, (2011), pp. 10070–10073 (cit. on pp. 3, 4, 6, 22, 23, 60).

[34] Fredrickson, D. C. "DFT-Chemical Pressure Analysis: Visualizing the Role of Atomic Size in Shaping the Structures of Inorganic Materials." *Journal of the American Chemical Society*, **134**, (2012), pp. 5991–5999 (cit. on pp. 4, 24, 30, 60).

[35] Frisch, M. J., Trucks, G. W., Schlegel, H. B., Scuseria, G. E., Robb, M. A., Cheeseman, J. R., Scalmani, G., Barone, V., Mennucci, B., Petersson, G. A., Nakatsuji, H., Caricato, M., Li, X., Hratchian, H. P., Izmaylov, A. F., Bloino, J., Zheng, G., Sonnenberg, J. L., Hada, M., Ehara, M., Toyota, K., Fukuda, R., Hasegawa, J., Ishida, M., Nakajima, T., Honda, Y., Kitao, O., Nakai, H., Vreven, T., Montgomery, J. A., Peralta, J. E., Ogliaro, F., Bearpark, M., Heyd, J. J., Brothers, E., Kudin, K. N., Staroverov, V. N., Kobayashi, R., Normand, J., Raghavachari, K., Rendell, A., Burant, J. C., Iyengar, S. S., Tomasi, J., Cossi, M., Rega, N., Millam, J. M., Klene, M., Knox, J. E., Cross, J. B., Bakken, V., Adamo, C., Jaramillo, J., Gomperts, R., Stratmann, R. E., Yazyev, O., Austin, A. J., Cammi, R., Pomelli, C., Ochterski, J. W., Martin, R. L., Morokuma, K., Zakrzewski, V. G., Voth, G. A., Salvador, P., Dannenberg, J. J., Dapprich, S., Daniels, A. D., Farkas, Foresman, J. B., Ortiz, J. V., Cioslowski, J. and Fox, D. J. *Gaussian 09, Revision B.01*. 2009 (cit. on p. 47).

[36] Galeev, T. R., Dunnington, B. D., Schmidt, J. R. and Boldyrev, A. I. "Solid state adaptive natural density partitioning: a tool for deciphering multi-center bonding in periodic systems." *Phys. Chem. Chem. Phys.* **15** (14), (2013), pp. 5022–5029 (cit. on p. 60).

[37] Goddard, W. A. and Wilson, C. W. "The role of kinetic energy in chemical binding." *Theoretica Chimica Acta*, **26** (3), (1972), pp. 211–230 (cit. on p. 61).

[38] Goedecker, S., Teter, M. and Hutter, J. "Separable Dual-Space Gaussian Pseudopotentials." *Phys. Rev. B*, **54** (3), (1996), pp. 1703–1710 (cit. on p. 34).

[39] Gonze, X., Amadon, B., Anglade, P. M., Beuken, J. M., Bottin, F., Boulanger, P., Bruneval, F., Caliste, D., Caracas, R., Côté, M., Deutsch, T., Genovese, L., Ghosez, P., Giantomassi, M., Goedecker, S., Hamann, D. R., Hermet, P., Jollet, F., Jomard, J., Leroux, S., Mancini, M., Mazevet, S., Oliveira, M. J. T., Onida, G., Pouillon, Y., Rangel, T., Rignanese, J. M., Sangalli, D., Shaltaf, R., Torrent, M., Verstraete, M. J., Zerah, G. and Zwanziger, J. W. "ABINIT: First-Principles Approach To Material and Nanosystem Properties." *Computer Physics Communications*, **180** (12), (2009), pp. 2582–2615 (cit. on pp. 6, 34).

[40] Gonze, X., Jollet, F., Abreu Araujo, F., Adams, D., Amadon, B., Applencourt, T., Audouze, C., Beuken, J.-M., Bieder, J., Bokhanchuk, A., Bousquet, E., Bruneval, F., Caliste, D., Côté, M., Dahm, F., Da Pieve, F., Delaveau, M., Di Gennaro, M., Dorado, B., Espejo, C., Geneste, G., Genovese, L., Gerossier, A., Giantomassi, M., Gillet, Y., Hamann, D. R., He, L., Jomard, G., Laflamme Janssen, J., Le Roux, S., Levitt, A., Lherbier, A., Liu, F., Lukač ević, I., Martin, A., Martins, C., Oliveira, M. J. T., Poncé, S., Pouillon, Y., Rangel, T., Rignanese, G.-M., Romero, A. H., Rousseau, B., Rubel, O., Shukri, A. A., Stankovski, M., Torrent, M., Van Setten, M. J., Van Troeye, B., Verstraete, M. J., Waroquiers, D., Wiktor, J., Xu, B., Zhou, A. and Zwanziger, J. W. "Recent developments in the ABINIT software package." *Computer Physics Communications*, **205**, (2016), pp. 106–131 (cit. on p. 34).

[41] Gonze, X., Rignanese, G.-m., Verstraete, M., Beuken, J.-m., Pouillon, Y., Caracas, R., Raty, J.-y., Olevano, V., Bruneval, F., Reining, L., Godby, R., Onida, G., Hamann, D. R. and Allan, D. C. "A brief introduction to the ABINIT software package." *Zeitschrift für Kristallographie*, **220**, (2005), pp. 558–562 (cit. on pp. 6, 34).

[42] Guo, Y. and Fredrickson, D. C. "On the Functionality of Complex Intermetallics: Frustration, Chemical Pressure Relief, and Potential Rattling Atoms in $Y_{11}Ni_{60}C_6$." *Inorganic Chemistry*, **55** (20), (2016), pp. 10397–10405 (cit. on p. 6).

[43] Hamann, D. R., Schlüter, M. and Chiang, C. "Norm-Conserving Pseudopotentials." *Phys. Rev. Lett.* **43** (20), (1979), pp. 1494–1497 (cit. on p. 21).

[44] Harris, N. A., Hadler, A. B. and Fredrickson, D. C. "In Search of Chemical Frustration in the Ca-Cu-Cd System: Chemical Pressure Relief in the Crystal Structures of Ca_5Cu_2Cd and $Ca_2Cu_2Cd_9$." *Zeitschrift für anorganische und allgemeine Chemie*, **637**, (2011), pp. 1961–1974 (cit. on p. 22).

[45] Hartwigsen, C., Goedecker, S. and Hutter, J. "Relativistic separable dual-space Gaussian pseudopotentials from H to Rn." *Phys. Rev. B*, **58** (7), (1998), pp. 3641–3662 (cit. on p. 34).

[46] Heine, V. "The Pseudopotential Concept." *Solid State Physics*, **24**, (1970), pp. 1–36 (cit. on p. 20).

[47] Hellmann, H. "A New Approximation Method in the Problem of Many Electrons." *The Journal of Chemical Physics*, **3** (1), (1935), p. 61 (cit. on p. 20).

[48] Hellmann, H. and Kassatotschkin, W. "Metallic Binding According to the Combined Approximation Procedure." *The Journal of Chemical Physics*, **4** (5), (1936), pp. 324–325. DOI: 10.1063/1.1749851 (cit. on p. 20).

[49] Henkelman Group. *Code: Bader Charge Analysis*. http://theory.cm.utexas.edu/henkelman/code/bader/. (Accessed on 04/22/2017) (cit. on p. 38).

[50] Hirshfeld, F. L. "Bonded-Atom Fragments For Describing Molecular Charge Densities." *Theoretica Chimica Acta*, **44** (2), (1977), pp. 129–138 (cit. on pp. 26, 27).

[51] Hohenberg, P. and Kohn, W. "Inhomogeneous Electron Gas." *Phys. Rev.* **136** (3B), (1964), B864–B871 (cit. on p. 13).

[52] Hopffgarten, M. v. and Frenking, G. "Energy decomposition analysis." *Wiley Interdisciplinary Reviews: Computational Molecular Science*, **2** (1), (2012), pp. 43–62 (cit. on pp. 60, 61).

[53] Hubbard, J. "Electron Correlations in Narrow Energy Bands." *Proceedings Mathematical Physical & Engineering Sciences*, **276** (1365), (1963) (cit. on p. 18).

[54] Hückel, E. "Quantentheoretische Beiträge zum Benzolproblem." *Zeitschrift für Physik*, **70**, (1931), pp. 204–286 (cit. on p. 22).

[55] Hückel, E. "Quantentheoretische Beiträge zum Problem der aromatischen und ungesättigten Verbindungen. III." *Zeitschrift für Physik*, **76**, (1932), pp. 628–648 (cit. on p. 22).

[56] Hughbanks, T. and Hoffmann, R. "Chains of trans-edge-sharing molybdenum octahedra: metal-metal bonding in extended systems." *Journal of the American Chemical Society*, **105** (11), (1983), pp. 3528–3537 (cit. on p. 60).

[57] Hughbanks, T. and Hoffmann, R. "Molybdenum chalcogenides: clusters, chains, and extended solids. The approach to bonding in three dimensions." *Journal of the American Chemical Society*, **105** (5), (1983), pp. 1150–1162 (cit. on p. 60).

[58] Izquierdo-Ruiz, F., Menéndez, J. M. and Recio, J. M. "Theoretical Analysis of Vibrational Modes in Uranyl Aquo Chloro Complexes." *Theor. Chem. Acc.* (2015), 134:7 (cit. on pp. 42, 43, 45, 54).

[59] Jayaraman, A., Klement, W. and Kennedy, G. C. "Phase Diagrams of Calcium and Strontium at High Pressures." *Phys. Rev.* **132** (4), (1963), pp. 1620–1624 (cit. on p. 109).

[60] Jeanloz, R., Ahrens, T. J., Mao, H. K. and Bell, P. M. "B1-B2 Transition in Calcium Oxide from Shock-Wave and Diamond-Cell Experiments." *Science*, **206** (4420), (1979) (cit. on p. 109).

[61] Jenkins, S. "Direct space representation of metallicity and structural stability in SiO solids." *Journal of Physics: Condensed Matter*, **14** (43), (2002), p. 10251 (cit. on p. 78).

[62] Johnson, E. R., Keinan, S., Mori-Sánchez, P., Contreras-García, J., Cohen, A. J. and Yang, W. "Revealing Noncovalent Interactions." *Journal of the American Chemical Society*, **132** (18), (2010), pp. 6498–6506 (cit. on pp. 3, 60).

[63] Kantorovich, L. *Quantum Theory of the Solid State: An Introduction*. 1st ed. Fundamental Theories of Physics 136. Springer Netherlands, 2004 (cit. on p. 22).

[64] Kaur, G., Panigrahi, P. and Valsakumar, M. C. "Thermal Properties of UO_2 with a Non-local Exchange-Correlation Pressure Correction: A Systematic First Principles DFT+U Study." *Modelling and Simulation in Materials Science and Engineering*, **21** (6), (2013), p. 065014 (cit. on p. 45).

[65] Kilduff, B. J. and Fredrickson, D. C. "Chemical Pressure-Driven Incommensurability in CaPd5: Clues to High-Pressure Chemistry Offered by Complex Intermetallics." *Inorganic Chemistry*, **55** (13), (2016), pp. 6781–6793 (cit. on p. 60).

[66] Kim, S.-J., Ponou, S. and Fässler, T. F. "Cation Substitution Effects in the System Sr2,àíxBaxBi3 ($0 \leqslant x \leqslant 1.3$): Structural Distortions Induced by Chemical Pressure." *Inorganic Chemistry*, **47** (9), (2008), pp. 3594–3602 (cit. on p. 4).

[67] Koch, W. and Holthausen, M. C. *A Chemist's Guide to Density Functional Theory*. 2nd ed. Wiley-VCH, 2001 (cit. on pp. 13–15, 17).

[68] Kohn, W. and Sham, L. J. "Self-Consistent Equations Including Exchange and Correlation Effects." *Phys. Rev.* **140** (4A), (1965), A1133–A1138 (cit. on pp. 13, 14, 17).

[69] Kohout, M., Pernal, K., Wagner, F. R. and Grin, Y. "Electron localizability indicator for correlated wavefunctions. I. Parallel-spin pairs." *Theoretical Chemistry Accounts*, **112** (5), (2004), pp. 453–459 (cit. on p. 60).

[70] Kresse, G. and Furthmüller, J. "Efficient Iterative Schemes for *ab initio* Total-Energy Calculations using A Plane-Wave Basis Set." *Phys. Rev. B*, **54** (16), (1996), pp. 11169–11186 (cit. on pp. 6, 33).

[71] Kresse, G. and Joubert, D. "From ultrasoft pseudopotentials to the projector augmented-wave method." *Phys. Rev. B*, **59** (3), (1999), pp. 1758–1775 (cit. on pp. 6, 33).

[72] Lee, C., Yang, W. and Parr, R. G. "Development of the Colle-Salvetti correlation-energy formula into a functional of the electron density." *Phys. Rev. B*, **37** (2), (1988), pp. 785–789 (cit. on p. 47).

[73] Lee, S. "Structural Diversity in Solid State Chemistry: A Story of Squares and Triangles." *Annual Review of Physical Chemistry*, **47** (1), (1996), pp. 397–419 (cit. on p. 23).

[74] Lewis, G. N. "The Atom and the Molecule." *J. Am. Chem. Soc.* **38**, (1916), pp. 762–786 (cit. on p. 3).

[75] Luaña, V., Recio, J. M. and Pueyo, L. "Quantum-mechanical description of ions in crystals: Electronic structure of magnesium oxide." *Phys. Rev. B*, **42** (3), (1990), pp. 1791–1801 (cit. on p. 43).

[76] Marqués, M., Ackland, G. J., Lundegaard, L. F., Stinton, G., Nelmes, R. J., McMahon, M. I. and Contreras-García, J. "Potassium under Pressure: A Pseudobinary Ionic Compound." *Phys. Rev. Lett.* **103** (11), (2009), pp. 115501–115505 (cit. on p. 109).

[77] Marques, M., Morales-Garcia, A., Menendez, J. M., Baonza, V. G. and Recio, J. M. "A novel crystalline SiCO compound." *Phys. Chem. Chem. Phys.* **17** (38), (2015), pp. 25055–25060 (cit. on p. 43).

[78] Martin, R. M. *Electronic structure: basic theory and practical methods*. Cambridge University Press: Cambridge, UK, New York, 2008, pp. 255–256 (cit. on pp. 13, 17, 20, 22, 24).

[79] Marzari, N., Mostofi, A. A., Yates, J. R., Souza, I. and Vanderbilt, D. "Maximally localized Wannier functions: Theory and applications." *Rev. Mod. Phys.* **84** (4), (2012), pp. 1419–1475 (cit. on p. 60).

[80] Michael, B., Sieffert, N., Golubnychiy, V. and Wipff, G. "Density Functional Theory Study of Uranium(VI) Aquo Chloro Complexes in Aqueous Solution." *The Journal of Physical Chemistry A*, **112** (11), (2008), pp. 2428–2436 (cit. on pp. 42, 43).

[81] Mizuguchi, Y., Paris, E., Sugimoto, T., Iadecola, A., Kajitani, J., Miura, O., Mizokawa, T. and Saini, N. L. "The effect of RE substitution in layered $REO_{0.5}F_{0.5}BiS_2$: chemical pressure, local disorder and superconductivity." *Phys. Chem. Chem. Phys.* **17** (34), (2015), pp. 22090–22096 (cit. on p. 4).

[82] Momma, K. and Izumi, F. "VESTA 3 for three-dimensional visualization of crystal, volumetric and morphology data." *Journal of Applied Crystallography*, **44** (6), (2011) (cit. on pp. 6, 35).

[83] Monkhorst, H. J. and Pack, J. D. "Special points for Brillouin-zone integrations." *Phys. Rev. B*, **13** (12), (1976), pp. 5188–5192 (cit. on pp. 33, 61).

[84] Mori-Sánchez, P., Pendás, Á. M. and Luaña, V. "Polarity inversion in the electron density of BP crystal." *Phys. Rev. B*, **63** (12), (2001), 125103–1:4 (cit. on p. 109).

[85] Nakamoto, K. "Theory of Normal Vibrations." *Infrared and Raman Spectra of Inorganic and Coordination Compounds*. John Wiley & Sons, Inc., 2008, pp. 1–147 (cit. on p. 52).

[86] Needham, P. "The source of chemical bonding." *Studies in History and Philosophy of Science Part A*, **45**, (2014), pp. 1–13 (cit. on p. 60).

[87] Nesper, R. "Bonding Patterns in Intermetallic Compounds." *Angewandte Chemie International Edition*, **30** (7), (1991), pp. 789–817 (cit. on p. 8).

[88] O,ÄôKeeffe, M., Hyde, B. G. "An alternative approach to non-molecular crystal structures with emphasis on the arrangements of cations." Vol. 61. (Chapter 2). Berlin: Springer Verlag, 1985 (cit. on p. 108).

[89] Olijnyk, H. and Holzapfel, W. B. "Phase transitions in K and Rb under pressure." *Physics Letters A*, **99** (8), (1983) (cit. on p. 109).

[90] Olijnyk, H. and Holzapfel, W. B. "Phase transitions in alkaline earth metals under pressure." *Physics Letters A*, **100** (4), (1984) (cit. on p. 109).

[91] Otero-de-la-Roza, A., Erin, R. J., and Luaña, V. "Critic2: A program for real-space analysis of quantum chemical interactions in solids." *Computer Physics Communications*, **185** (3), (2014), pp. 1007–1018 (cit. on pp. 6, 38).

[92] Parr, R. G., Yang, W. *Density-functional theory of atoms and molecules*. International series of monographs on chemistry, 16. Oxford, 1989 (cit. on p. 16).

[93] Pauling, L. "The Principles Determining the Structure of Complex Ionic Crystals." *Journal of the American Chemical Society*, **51** (4), (1929), pp. 1010–1026 (cit. on p. 108).

[94] Pauling, L. *The Nature of the Chemical Bond*. Cornell Univ. Press, Ithaca, New York, 1939 (cit. on p. 3).

[95] Pauling, L. *The Nature of the Chemical Bond and the Structure of Molecules and Crys- tals: an Introduction to Modern Structural Chemistry*. Cornell Univ. Press, Ithaca, New York, 1960 (cit. on pp. 3, 108).

[96] Pawley, G. S. and Rinaldi, R. P. "Constrained refinement of orthorhombic sulphur." *Acta Crystallographica Section B*, **28** (12), (1972), pp. 3605–3609 (cit. on p. 82).

[97] Perdew, J. P., Burke, K. and Ernzerhof, M. "Generalized Gradient Approximation Made Simple." *Phys. Rev. Lett.* **77**, (1996), pp. 3865–3868 (cit. on pp. 17, 48).

[98] Perdew, J. P., Ruzsinszky, A., Csonka, G. I., Vydrov, O. A., Scuseria, G. E., Constantin, L. A., Zhou, X. and Burke, K. *Physical Review Letters*, **100** (13), (2008) (cit. on p. 45).

[99] John P. Perdew and Yue Wang. "Accurate and simple analytic representation of the electron-gas correlation energy." *Phys. Rev. B*, **45** (23), (1992), pp. 13244–13249 (cit. on p. 17).

[100] Rajendra Prasad. *Electronic Structure of Materials*. CRC Press, 2013 (cit. on pp. 17, 20).

[101] Rabone, J. and Krack, M. "A procedure for bypassing metastable states in local basis set DFT+U calculations and its application to uranium dioxide surfaces." *Computational Materials Science*, **71**, (2013), pp. 157–164 (cit. on p. 45).

[102] Recio, J. M., Menendez, J. M. and Otero de-la-Roza, A. "An Introduction to High-Pressure Science and Technology." Ed. by V. Luaña A. Otero-de-la-Roza and M. Flórez. Boca Raton, Florida: CRC Press, 2015. Chap. 1 (cit. on pp. 25, 42).

[103] J. M. Recio et al. "Low- and high-pressure ab initio equations of state for the alkali chlorides." *Phys. Rev. B*, **48** (9), (1993), pp. 5891–5901 (cit. on p. 43).

[104] Reed, A. E. and Weinhold, F. "Natural localized molecular orbitals." *The Journal of Chemical Physics*, **83** (4), (1985), pp. 1736–1740 (cit. on p. 60).

[105] Reed, A. E., Curtiss, L. A., and Weinhold, F. "Intermolecular interactions from a natural bond orbital, donor-acceptor viewpoint." *Chemical Reviews*, **88** (6), (1988), pp. 899–926 (cit. on pp. 3, 60).

[106] Ruedenberg, K. "The Physical Nature of the Chemical Bond." *Rev. Mod. Phys.* **34 (2)**, (1962), pp. 326–376 (cit. on pp. 4, 61, 64).

[107] Salvadó, M. A., Pertierra, P., Morales-García, A., Menéndez, J. M. and Recio, J. M. "Understanding Chemical Changes across the α-Cristobalite to Stishovite Transition Path in Silica." *The Journal of Physical Chemistry C*, **117** (17), (2013), pp. 8950–8958 (cit. on p. 43).

[108] Savin, A. "The electron localization function (ELF) and its relatives: interpretations and difficulties." *Journal of Molecular Structure: THEOCHEM*, **727** (1–3), (2005), pp. 127–131 (cit. on p. 60).

[109] Savin, A., Becke, A. D., Flad, J., Nesper, R., Preuss, H. and von Schnering, H. G. "A New Look at Electron Localization." *Angewandte Chemie International Edition*, **30** (4), (1991) (cit. on p. 60).

[110] Savin, A., Nesper, R., Wengert, S. and Fässler, T. F. "ELF: The Electron Localization Function." *Angewandte Chemie International Edition in English*, **36** (17), (1997), pp. 1808–1832 (cit. on p. 60).

[111] Schmidt, M. W., Ivanic, I. and Ruedenberg, K. "Covalent bonds are created by the drive of electron waves to lower their kinetic energy through expansion." *The Journal of Chemical Physics*, **140** (20), (2014), p. 204104 (cit. on p. 61).

[112] Schnaars, D. D. and Wilson, R. E. "Structural and Vibrational Properties of $U(VI)O_2Cl_4^{-2}$ and $Pu(VI)O_2Cl_4^{-2}$ Complexes." *Inorganic Chemistry*, **52** (24), (2013), pp. 14138–14147 (cit. on pp. 7, 42, 43, 45, 49, 51, 52).

[113] Schnaars, D. D. and Wilson, R. E. "Lattice Solvent and Crystal Phase Effects on the Vibrational Spectra of $UO_2Cl_4^{-2}$." *Inorganic Chemistry*, **53** (20), (2014), pp. 11036–11045 (cit. on pp. 7, 42, 43, 45, 49, 51, 52).

[114] Shi, H., Chu, M. and Zhang, P. "Optical properties of UO_2 and PuO_2." *Journal of Nuclear Materials*, **400** (2), (2010), pp. 151–156 (cit. on p. 45).

[115] Siboulet, B., Marsden, C. J. and Vitorge, P. "A theoretical study of uranyl solvation: Explicit modelling of the second hydration sphere by quantum mechanical methods." *Chemical Physics*, **326**, (2006), pp. 289–296 (cit. on pp. 43, 45, 54–56).

[116] Silvi, B., Savin, A. "Classification of chemical bonds based on topological analysis of electron localization functions." *Nature*, **371** (6499), (1994) (cit. on pp. 3, 4, 60).

[117] Silvi, B. and Gatti, C. "Direct Space Representation of the Metallic Bond." *The Journal of Physical Chemistry A*, **104** (5), (2000), pp. 947–953 (cit. on p. 76).

[118] Tan, X., Fabbris, G., Haskel, D., Yaroslavtsev, A. A., Cao, H., Thompson, C. M., Kovnir, K., Menushenkov, A. P., Chernikov, R. V., Garlea, V. O. and Shatruk, M. "A Transition from Localized to Strongly Correlated Electron Behavior and Mixed Valence Driven by Physical or Chemical Pressure in ACo2As2 (A = Eu and Ca)." *Journal of the American Chemical Society*, **138** (8), (2016), pp. 2724–2731 (cit. on p. 4).

[119] Tang, W., Sanville, E. and Henkelman, G. "A grid-based Bader analysis algorithm without lattice bias." *Journal of Physics: Condensed Matter*, **21** (8), (2009) (cit. on pp. 6, 37).

[120] Vallet, V., Wahlgren, U. and Grenthe, I. "Probing the Nature of Chemical Bonding in Uranyl(VI) Complexes with Quantum Chemical Methods." *Physical Chemistry A*, **116** (50), (2012), pp. 12373–12380 (cit. on pp. 7, 42, 43, 47, 52).

[121] Vegas, Á. and Jansen, M. "Structural Relationships between Cations and Alloys; An Equivalence between Oxidation and Pressure." *Acta Crystallographica Section B*, **58** (1), (2002), pp. 38–51 (cit. on p. 4).

[122] Vegas, Á. and Mattesini, M. "Towards a generalized vision of oxides: disclosing the role of cations and anions in determining unit-cell dimensions." *Acta Crystallographica Section B*, **66** (3), (2010), pp. 338–344 (cit. on p. 8).

[123] Vegas, Á., Santamaría-Pérez, D., Marqués, M., Flórez, M., García Baonza, V., Recio, J. M. "Anions in metallic matrices model: application to the aluminium crystal chemistry." *Acta Crystallographica Section B*, **62** (2), (2006), pp. 220–227 (cit. on pp. 4, 8, 109, 111, 112, 114).

[124] von Schnering, H. G., Nesper, R. "How Nature Adapts Chemical Structures to Curved Surfaces." *Angewandte Chemie International Edition*, **26** (11), (1987) (cit. on pp. 108, 109).

[125] Wagner, F., Bezugly, V., Kohout, M. and Grin, Y. "Charge Decomposition Analysis of the Electron Localizability Indicator: A Bridge between the Orbital and Direct Space Representation of the Chemical Bond." *Chemistry - A European Journal*, **13** (20), (2007), pp. 5724–5741 (cit. on p. 60).

[126] Wang, F. and Miller, G. J. "Revisiting the Zintl-Klemm Concept: Alkali Metal Trielides." *Inorganic Chemistry*, **50** (16), (2011), pp. 7625–7636 (cit. on pp. 60, 61).

[127] Wannier, G. H. "The Structure of Electronic Excitation Levels in Insulating Crystals." *Phys. Rev.* **52** (3), (1937), pp. 191–197 (cit. on p. 60).

[128] Watkin, D. J., Denning, R. G. and Prout, K. "Structure of dicaesium tetrachlorodioxouranium(VI)." *Acta Crystallographica Section C*, **47** (12), (1991), pp. 2517–2519 (cit. on pp. 33, 43).

[129] Weisshaar, J. C. "Application of Badger's rule to third row metal diatomics." *The Journal of Chemical Physics*, **90 (3)**, (1989), pp. 1429–1433 (cit. on p. 52).

[130] Wiktor, J., Barthe, M.-F., Jomard, G., Torrent, M., Freyss, M. and Bertolus, M. "Coupled experimental and DFT+U investigation of positron lifetimes in UO_2." *Phys. Rev. B*, **90** (18), (2014), pp. 184101–184122 (cit. on p. 33).

[131] Winzenick, W. and Holzapfel, W. B. "Structure systematic and equations of states for the alkaline earth metals under pressure." *High Pressure Science and Technology*, (1996), pp. 384–386 (cit. on p. 109).

[132] Xu, B., Wang, Q., and Tian, Y. "Bulk modulus for polar covalent crystals." *Scientific Reports*, **3**, (2013), 3068/1–7 (cit. on p. 45).

[133] Yannello, V. J., Kilduff, B. J. and Fredrickson, D. C. "Isolobal Analogies in Intermetallics: The Reversed Approximation MO Approach and Applications to $CrGa_4$- and Ir_3Ge_7-Type Phases." *Inorganic Chemistry*, **53** (5), (2014), pp. 2730–2741 (cit. on p. 60).

[134] Yee, K. A. and Hughbanks, T. "Utility of semilocalized bonding schemes in extended systems: three-center metal-metal bonding in molybdenum sulfide (MoS_2), niobium tantalum sulfide bronze ($H_x(Nb,Ta)S_2$), and zirconium sulfide (ZrS)." *Inorganic Chemistry*, **30** (10), (1991), pp. 2321–2328 (cit. on p. 60).

[135] Yu, M., Trinkle, D. R. and Martin, R. M. "Energy density in density functional theory: Application to crystalline defects and surfaces." *Phys. Rev. B*, **83** (11), (2011), p. 115113 (cit. on p. 21).

[136] Yun, Y., Kim, H., Lim, H. and Park, H. K. "Electronic Structure of UO_2 from the Density Functional Theory with On-Site Coulomb Repulsion." *J. Korean Phys. Soc.* **50** (5), (2007), pp. 1285–1289 (cit. on p. 18).

[137] Zhurov, V. V., Zhurova, E. A. and Pinkerton, A. A. "Chemical Bonding in Cesium Uranyl Chloride Based on the Experimental Electron Density Distribution." *Inorganic Chemistry*, **50** (13), (2011), pp. 6330–6333 (cit. on pp. 33, 42, 43).

[138] Zhurov, V. V., Zhurova, E. A., Stash, A. I. and Pinkerton, A. A. "Characterization of Bonding in Cesium Uranyl Chloride: Topological Analysis of the Experimental Charge Density." *The Journal of Physical Chemistry A*, **115** (45), (2011), pp. 13016–13023 (cit. on pp. 42, 43, 45–47, 54).

[139] Zurek, E., Jepsen, O. and Andersen, O. K. "Muffin-Tin Orbital Wannier-Like Functions for Insulators and Metals." *ChemPhysChem*, **6** (9), (2005), pp. 1934–1942 (cit. on p. 60).

[140] Zurek, E., Jepsen, O. and Andersen, O. K. "Searching for the Interlayer Band and Unravelling the Bonding in $\beta - ThSi_2$ and $\alpha - ThSi_2$ with NMTO Wannier-like Functions." *Inorganic Chemistry*, **49** (4), (2010), pp. 1384–1396 (cit. on p. 60).